Positron emission tomography for quality assurance in proton therapy

Buitenhuis, Tom

DOI:
10.33612/diss.110452833

Positron Emission Tomography for Quality Assurance in Proton Therapy

ISBN (printed): 978-94-034-2221-3
ISBN (electronic): 978-94-034-2220-6
Printed by Ridderprint BV
Cover design by Wout Buitenhuis

rijksuniversiteit
groningen

Positron Emission Tomography for Quality Assurance in Proton Therapy

Proefschrift

ter verkrijging van de graad van doctor aan de
Rijksuniversiteit Groningen
op gezag van de
rector magnificus prof. dr. C. Wijmenga
en volgens besluit van het College voor Promoties.

De openbare verdediging zal plaatsvinden op

vrijdag 10 januari 2020 om 16:15 uur

door

Hans Jan Thomas Buitenhuis

geboren op 19 juli 1989
te Ridderkerk

Promotor
Prof. dr. S. Brandenburg

Copromotor
Dr. P. G. Dendooven

Beoordelingscommissie
Prof. dr. R. Boellaard
Prof. dr. W. Enghardt
Prof. dr. J. Seco

Contents

Chapter 1

Introduction

Cancer is one of the leading causes of death in The Netherlands. In 2017, all types of cancer combined caused 47,000 of 150,000 recorded causes of death (Centraal Bureau voor de Statistiek, 2017). There are several ways to treat cancer. The most common treatments include radiotherapy, surgery, chemotherapy, targeted therapy, hormonal therapy and immunotherapy. Often, different treatment modalities are combined to maximize their efficacy. For example, patients might receive radiotherapy after surgery to remove any traces of cancer cells that were left.

Radiotherapy uses ionizing radiation to kill tumor cells by damaging their DNA. This radiation can be applied internally (brachytherapy) or externally. For brachytherapy, radioactive sources are implanted in and around the tumor, which deliver dose directly at the right location. However, for this method, the tumor needs to be in a relatively easily accessible location. For some patients, radioactive substances that accumulate in the tumor are injected. This radiation then delivers most dose at the site where it accumulates. More often, the radiation is applied using a source outside of the body. In the past, radioactive sources such as ^{60}Co were used to supply MeV gamma rays. Nowadays, a linear accelerator is used in most radiotherapy facilities to produce MeV electron beams. These electrons are stopped in a tungsten absorber to generate MeV X-rays, which penetrate deeply into the body.

Other particles can also be used, such as protons or even heavier nuclides. Accelerating these particles to clinically useful energies requires large particle accelerators. Already in 1946, Robert R. Wilson wrote about how protons with an energy in the order of 100 MeV are very interesting for radio-

therapy (Wilson, 1946). Currently, 92 particle therapy centers exist all over the world (PTCOG, 2019). Patients are being treated daily with protons, and to a lesser extent with carbon nuclei. Until 2017 approximately 170.000 patients have been treated with protons and carbon nuclei worldwide (PTCOG, 2019). In The Netherlands, several proton therapy centers were recently built. The University Medical Center Groningen has treated a first patient in their new proton therapy facility in January 2018 (UMCG, 2018). HollandPTC started treatments in August 2018 and ZON-PTC in Maastricht started treatments in February 2019.

Proton beam radiotherapy is characterized by possibilities for improved localized dose deposition as compared to photon radiotherapy. This characteristic may be exploited to reduce collateral damage to healthy tissues surrounding the tumor, and in applicable cases, also to escalate the dose to the tumor. However, the finite proton range and the high dose in the Bragg peak come with increased sensitivity to deviations from the planned treatment compared to photons. Therefore, an *in vivo* means of verifying the dose delivery is key to fully exploit the clinical benefit of the physically superior dose distributions.

Because the protons are stopped inside the patient body, *in vivo* dose delivery verification requires imaging of secondary radiation induced by proton interactions in the human body. High-energy photons are most often used for this purpose, as they have favorable production cross sections and they can escape the patient body. Two types of high-energy photons that follow from nuclear reactions induced by the protons are available: positron annihilation photons (511 keV) following the decay of positron emitting nuclides and prompt gamma rays emitted on a sub-nanosecond timescale in the decay of excited nuclei.

This thesis is subdivided in two sections. The first section is about how fast information on the dose delivery can be obtained using positron emission tomography (PET). As a typical PET scan takes at least a few minutes to obtain enough counts for range verification due to the half-lives in the order of 2 to 20 min, instantaneous feedback is not possible. This has lead to the development of prompt gamma ray imaging techniques, which in principle allow real-time feedback on the dose delivery. However, when PET imaging during the irradiation is considered, also the decay of shorter-lived nuclides such as ^{12}N with a half-life of 11 ms will contribute to the information. In the first section, imaging of these shorter-lived nuclides is studied to open the door towards using PET for real-time dose delivery verification.

In the second section, the qualitative differences between PET and prompt gamma ray imaging are investigated. A detailed Monte Carlo simulation framework was created to study the differences in PET and prompt gamma ray distributions using real patient cases.

In chapter 2, the rationale behind using PET and prompt gamma

ray imaging for dose delivery verification in proton therapy is explained. Also, the novel technique to use short-lived positron emitting nuclides to obtain fast feedback with a PET scanner will be introduced.

In chapter 3, ^{12}N nuclei are used to provide fast imaging of the proton range and feedback on the dose delivery.

Chapter 4 shows results from fast PET imaging using nuclides that are only produced on bone.

Chapter 5 describes the components of the Monte Carlo simulation software package that was developed to investigate PET and prompt gamma ray imaging using clinically realistic patient irradiation.

Chapters 6 and 7 contain simulation studies investigating different aspects of PET and prompt gamma ray imaging in a clinical setting. The differences between PET and prompt gamma distributions are investigated, as well as the effect of different PET scanning protocols on the ability to detect clinically relevant differences between the planned and delivered dose distributions.

Chapter 8 contains a summary of this thesis and a future outlook.

Chapter 2

Proton therapy dose delivery verification

The interest in irradiating tumors with protons rather than with high energy photons is rooted in the difference in physical interactions of these particles with patient tissues leading to different dose profiles (Wilson, 1946), as depicted in figure 2.1. A typical high energy photon beam depth-dose profile has a small build-up region of 1 to 2 cm after which a maximum dose is achieved. The dose then decreases slowly as a function of depth until the photon beam exits the patient. The proton beams used in proton therapy do not exit the patient body. Their range inside the patient is determined by the initial kinetic energy. This Bragg peak dose profile, characteristic for the energy deposition of charged particles, has a finite depth and the highest dose is delivered at the end of the particle range.

A single energy (pristine) Bragg peak is typically not broad enough to cover the entire tumor volume, so the dose is spread out in depth by using energy modulation. Using the right combination of energy and fluence of these beams, a flat spread out Bragg peak (SOBP) can be created that spans the entire depth of the tumor. A laterally extended dose profile can be obtained by either passive scattering or pencil beam scanning (PBS) as depicted in figure 2.2. For passive scattering, the beam is broadened using a scatter foil and patient-specific collimators are used to conform the beam to the lateral shape of the tumor. Most modern proton therapy centers are equipped with some form of PBS, which uses a raster of multiple overlapping spots and a range of proton beam energies (so-called energy layers) to obtain full 3D tumor coverage. The proton

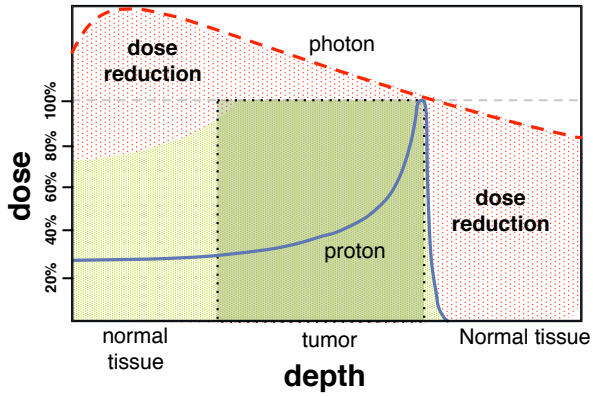

Figure 2.1: Depth-dose curves for a photon (red dashed) and proton (blue solid) beam. Proton beams of different energies and fluences are combined to deliver the spread-out Bragg peak (green). The dose reduction to normal tissue after the tumor and in front of the tumor is depicted as the dotted red area. Figure adapted from Levin et al. (2005)

fluence of each single spot in each energy layer can be optimized to obtain the desired dose distribution that best conforms to the tumor and results in minimal complications due to the dose to normal tissue. The tumor is usually irradiated from multiple directions. This treatment modality is called intensity modulated proton therapy (IMPT).

For specific tumor sites, these physical properties enable the creation of treatment plans that deliver less dose to co-irradiated normal tissue compared to treatment with high energy photons. This either allows tumor dose escalation with the aim to increase tumor control or organ at risk (OAR) dose reduction with the aim to reduce the probability and/or severity of radiation-induced complications. This is especially beneficial for tumors that are close to critical structures, such as the optic nerve or the brain stem, or for pediatric patients for whom secondary malignancy occurrence due to treatment is a serious concern.

2.1 Deviations from the treatment plan

Compared to photon radiotherapy, the delivered dose distribution for proton therapy is more sensitive to deviations from the situation on which the treatment plan is based due to the finite range of the protons and the steep dose gradients in the Bragg peak. These deviations might stem from, among others, ion range uncertainties, day-to-day variations in patient positioning, or anatomical changes in the patient.

Anatomical changes can occur during an irradiation because of or-

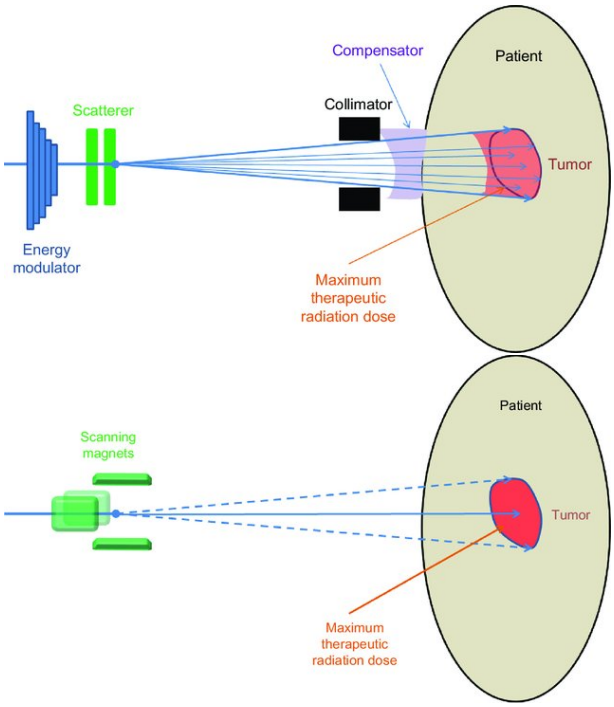

Figure 2.2: *Top*: Passive scattering. Shown are the energy modulator, the scatter foils broadening the beam, the collimator that shapes the lateral edge of the field and the range compensator that shapes the distal edge of the field. *Bottom*: Pencil Beam Scanning (PBS). Shown are the scanning magnets that direct the pencil beam to the desired location. The energy of the beam is determined further upstream. Figures from Wang (2015).

gan motion coupled to e.g. the breathing cycle of the patient. Techniques such as breath-hold and irradiation gating exist to mitigate this problem (Boda-Heggemann et al., 2016). Inter-fractional anatomical changes can be caused by weight-loss over the course of the treatment, filling of organs or cavities such as the bladder, the rectum or the nasal cavity, or by shrinkage of the tumor.

Ion range uncertainties depend on the estimation procedure of the relative stopping power of patient tissue for protons based on the treatment planning X-ray CT. Since the interaction of photons and protons with patient tissue is different, there is no one-to-one relationship between the Hounsfield unit (HU) from the X-ray CT and the proton stopping power of that tissue. The same HU for two tissues might correspond to different stopping powers, and similarly, a difference in HU does not always imply a difference in proton stopping power. These uncertainties force treatment planners to create sub-

optimal plans. For example, rather large margins in the order of 2 to 3.5 % of the proton range plus 1 to 3 mm are introduced around the tumor to ensure the full tumor receives the prescribed dose even when a range deviation occurs (Paganetti, 2012). At Massachusetts General Hospital (MGH) a margin of 3.5 % of the proton range + 1 mm is used. Other facilities, such as MD Anderson, Loma Linda University Medical Center and the Roberts Proton Therapy Center apply a margin of 3.5 % of the proton range + 3 mm. The University of Florida Proton Therapy Institute uses a margin of 2.5 % of the proton range + 1.5 mm. For a deep-seated tumor at a depth of 20 cm, the range margin of 3.5 % + 3 mm represents a potential overshoot of 10 mm into normal tissue, which might receive the full tumor dose. Normal tissue around the tumor is thus unavoidably irradiated. For some sites where the tumor is located close to a critical structure, a treatment planner might then choose to plan a field with the lateral edge close to the critical structure rather than the sharper distal edge, so that range deviations will not cause an over-shoot into the critical structure and the structure is not potentially irradiated due to the range uncertainties. However, as the lateral penumbra of proton therapy fields are in general not sharper than the lateral penumbra of photon irradiation, a potential benefit of proton therapy is lost in this way.

Another source of range uncertainties are treatment planning systems that use an analytical dose calculation engine. An analytical dose calculation can not accurately take into account the effect of complex heterogeneities in the beam path, and the effect on the proton range distal fall-of shape due to multiple Coulomb scattering (Paganetti, 2012). These range deviations cannot be modeled by just taking into account the stopping power and water equivalent path lengths (WEPL) of the materials involved. Analytical dose calculation engines were optimized to better account for these heterogeneities by for instance subsampling each spot, but the gold standard currently is Monte Carlo dose calculation, which is offered by most modern treatment planning systems. This allows for more accurate dose calculation, at the cost of a longer computing time. However, as Paganetti also points out, Monte Carlo simulations also introduce a source of uncertainty in the dose calculation. Physics settings need to be optimized and benchmarked with actual measurements, and a parameter of the Bethe-Bloch energy loss formula which has an effect on the range, the mean excitation energy I of different types of material, is still under debate.

There are several approaches to deal with range uncertainties. Efforts are ongoing to more accurately predict or measure the proton stopping power. For instance, dual energy computed tomography (DECT) (Bazalova, Carrier, Beaulieu, & Verhaegen, 2008; Hünemohr et al., 2014; Möhler et al., 2018; Taasti et al., 2018; Van Abbema, 2017; Van Abbema, Van der Schaaf, Kristanto, Groen, & Greuter, 2012; van Abbema et al., 2015) or Detector-based Spectral CT (Rassouli, Etesami, Dhanantwari, & Rajiah, 2017) provide more information on tissue composition than a regular single energy planning CT,

and thereby can, in principle, produce more accurate stopping powers. Using two or more measurements per voxel at different energies, a more accurate identification of the tissue can be made, since the relation between tissue properties and photon attenuation depends on the photon energy. This will lead to better stopping power determination and a smaller range uncertainty, which will allow proton therapy treatment with reduced safety margins.

The use of protons for radiography or CT has already been proposed by Cormack (1963), but has seen limited clinical application (Johnson, 2018; Schneider et al., 2004). Up to now, the main disadvantage of proton radiography compared to X-ray imaging is the fact that due to multiple Coulomb scattering, the spatial resolution of the images is poor. However, proton radiography in a proton therapy context can give information that an X-ray CT cannot deliver: a direct measurement of the stopping powers for protons of patient tissues. Using high energy proton beams that pass through the patient, the residual energy of the protons after the patient can be measured simultaneously with the location and angle of the proton. Using these data, a proton stopping power map of the patient can be acquired. This map might then be fused with a X-ray CT or MRI image to enhance the anatomical features and spatial resolution. When the proton therapy stopping power is measured directly, sources of uncertainty such as arising from the conversion of X-ray attenuation to stopping power are reduced.

2.2 *In vivo* range verification methods

To fully exploit the physical advantages of proton therapy the delivered dose distribution should be accurately known. *In vivo* measurements of the dose distribution can help to achieve this. Since the particles stop at the end of their range inside the patient, secondary signals that have a strong relation with the dose distribution need to be used for verification of the dose delivery. Most verification methods depend on the imaging of positron-emitting nuclei or prompt gamma rays, which are created via nuclear interactions between the particle beam and the patient. An overview of these nuclear techniques can be found in reviews by Fiedler, Kunath, Priegnitz, and Enghardt (2012); Knopf and Lomax (2013); Kraan (2015); Krimmer, Dauvergne, Létang, and Testa (2018); Parodi (2011, 2015); Parodi and Polf (2018); Studenski and Xiao (2010); Zhu and El Fakhri (2013). A completely different technique currently under investigation, is the detection of thermoacoustic waves generated by a local increase in temperature due to absorbed dose, using an ultrasound probe (Assmann et al., 2015; Hayakawa et al., 1995; Jones, Vander Stappen, et al., 2016; Lehrack et al., 2017; Nie et al., 2018; Patch et al., 2016). The following sections give more details on each of these methods.

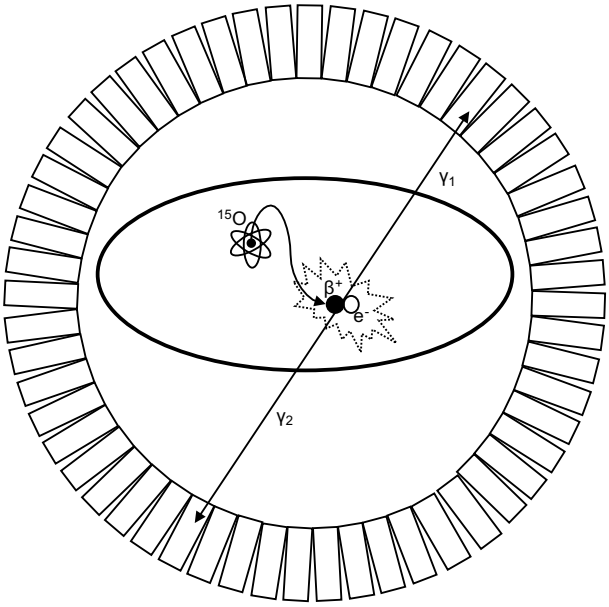

Figure 2.3: Schematic representation of positron emission tomography. An ^{15}O nucleus emits a positron, which travels through the patient body until it annihilates with an electron. This produces two back-to-back photons (γ_1 and γ_2), which are detected in coincidence to determine their LOR.

2.2.1 Positron emission tomography

The method that so far has been tested most extensively in a clinical environment is Positron Emission Tomography (PET), which is schematically depicted in figure 2.3. PET is an imaging technique that is mostly used as a diagnostic tool in nuclear medicine, whereby a radioactive tracer molecule is injected in the patient. This radioactive tracer is a molecule containing a radioisotope, meaning it is unstable and will decay with a certain half-life. For PET, radioisotopes are chosen that decay with the emission of a positron (β^+) particle. The positron travels until it is thermalized, after which it annihilates with one of the surrounding electrons, whereby two 511 keV photons are created. Due to momentum conservation, these photons are emitted nearly back-to-back, meaning in opposite directions. These two photons can then be detected in coincidence by pairs of detectors placed around the patient. These two coincident events define a line of response (LOR) on which the annihilation took place. The use of coincident detection to determine the LOR means that no mechanical collimation is needed as compared to single photon emission imaging techniques used for prompt gamma ray imaging. Combining all

Table 2.1: Longer-lived PET nuclei produced in patient tissue by proton therapy, the reactions that produce them and some of their characteristics. $T_{1/2}$ indicates the half-life of the nucleus. β^+E_{max} shows the maximum positron energy. E_{thresh} shows the threshold energy of the production reaction. Data are obtained from the EXFOR database (Otuka et al., 2014) and the Q-value calculator (https://www.nndc.bnl.gov/qcalc/qcalcr.jsp).

nucleus	$T_{1/2}$	β^+E_{max} (MeV)	reactions	E_{thresh}(MeV)
^{15}O	2.04 m	1.73	^{16}O(p,pn)^{15}O	16.79
^{14}O	70.6 s	1.8, 4.1	^{16}O(p,p2n)^{14}O	30.7
^{13}N	9.97 m	1.20	^{16}O(p,α)^{13}N	5.66
			^{16}O(p,2p2n)^{13}N	35.6
			^{14}N(p,pn)^{13}N	11.44
^{11}C	20.4 m	0.96	^{12}C(p,pn)^{11}C	20.61
			^{14}N(p,α)^{11}C	3.22
			^{14}N(p,2p2n)^{11}C	33.5
			^{16}O(p,αpn)^{11}C	27.50
			^{16}O(p,3p3n)^{11}C	57.6
^{10}C	19.3 s	1.9	^{12}C(p,p2n)^{10}C	34.5
^{30}P	2.50 m	3.21	^{31}P(p,pn)^{30}P	12.7
^{38g}K	7.64 m	2.72	^{40}Ca(p,2pn)^{38g}K	21.9

the LORs detected during a scan, an image reconstruction algorithm such as maximum-likelihood expectation-maximization (Parra & Barrett, 1998) yields an image of the positron emitting nuclide distribution.

For diagnostic PET, this image corresponds to the radiotracer distribution, for instance the glucose uptake distribution imaged with the fludeoxyglucose (FDG) radiotracer. However, for *in vivo* dose delivery verification of proton therapy, the radionuclides are not injected or otherwise supplied to the patient; instead they are created by interactions of the proton beam with patient tissue. During the irradiation, several nuclear reactions create unstable nuclei which decay via positron emission. The most abundant long-lived positron-emitting nuclides that are created by particle beams are ^{15}O, ^{11}C, ^{30}P, and ^{38g}K with radioactive half-lives between 2 and 20 minutes. Table 2.1 shows an overview of the most important PET nuclides that are created in the patient. In soft tissue, which contains mostly carbon and oxygen atoms, most PET counts will come from ^{15}O and ^{11}C. For bone structures, which also contain a sizable fraction of calcium and phosphorus atoms, counts will also originate from ^{30}P and ^{38g}K.

Using these positron emitting nuclide distributions for dose delivery verification can be done in different ways. Since the physical mechanisms of dose deposition and positron emitting nuclide creation are different, there is

no one-to-one correspondence between the measured PET image and the dose distribution. For PET with proton therapy, there is no sharp peak in positron emitter production near the end of the range as is the case for dose deposition. The nuclear reaction cross sections as a function of proton energy describing the production of positron emitting nuclides are shown in figure 5.5. The amount and type of positron emitting nuclides that are produced by a proton beam are dependent on the elemental composition of the tissue, while the dose distribution is mostly insensitive to variations in elemental composition. Another notable difference between the dose distribution and the measured PET image is the fact that below a certain threshold energy no positron emitting nuclides are created any more. This means that the distal edge of the PET image differs from the proton range and the distal edge of the delivered dose distribution. These factors imply that a measured PET image cannot be compared directly with the dose distribution from the treatment plan. Because of the complicated cross section shape as well as the fact that different reaction channels are not easily separable in the PET image, a dose image can also not be obtained or reconstructed from the PET measurement.

However, two approaches exist to verify the dose delivery. The measured image can be compared to an expected image based on a detailed simulation of the treatment and the associated time structures, which requires a close correspondence between the physical treatment and the simulation. This method often uses a Monte Carlo simulation of the dose delivery where the activity distribution at the time of measurement is calculated based on the proton transport and nuclear production cross sections. The measurement of the resulting activity distribution with a PET scanner can then be calculated as well using Monte Carlo simulations, or an approximation of the PET image from the simulation can be made by blurring the activity distributions. Another approach, which does not require Monte Carlo simulations, is comparing the PET images acquired on consecutive days to each other. This will allow the identification of day-to-day variations in the dose delivery such as setup deviations or the sudden filling of organs or cavities. Sources of dose delivery error that might cause a range error but do not change from one day to the next, such as in the Hounsfield unit to stopping power calibration, cannot be identified in this way, as no reference image for the planned case was calculated.

2.2.2 PET imaging geometries and protocols

Three different PET geometries can be discerned to acquire an image for dose delivery verification (Zhu & El Fakhri, 2013), depicted in figure 2.4.

The most simple imaging protocol is *off-line* PET imaging, whereby a PET scanner is placed in the vicinity of the treatment area, but in a different room. This means the patient needs to finish the treatment, and then be transported or guided to the imaging system before the actual verification scan

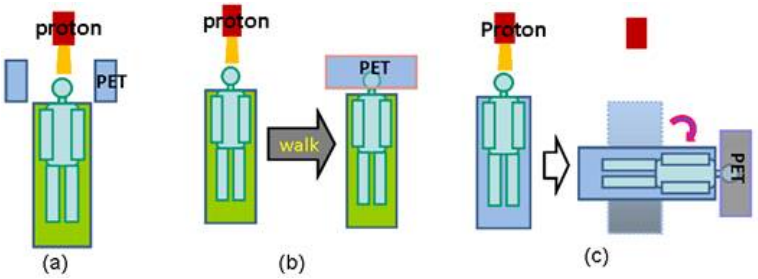

Figure 2.4: Schematic representation of three different positron emission tomography operational modalities for use with proton therapy, taken from (Zhu & El Fakhri, 2013). (a) shows the in-beam or in-situ configuration, which allows PET measurements with the beam on, during spot-pauses, or starting directly after the beam has turned off, (b) shows off-line PET whereby the patient needs to be transported to a clinical PET scanner in another room, (c) shows in-room PET, which uses a PET scanner placed in the treatment room.

can be performed. The advantage of this method is that a regular off-the-shelf clinical scanner can be used, which means no additional integration costs are required. Most clinical PET systems today are sold in combination with a CT or MRI scanner, so with little extra effort, anatomical information can be co-registered. Radiation damage to the scanner is not an issue, as the scanner is not placed in a high radiation environment.

The disadvantage is the long waiting time between the irradiation and the scan. Since the main long-lived contributions to the number of counts stem from ^{15}O and ^{11}C with a half-life of approximately 2 and 20 minutes, a delay of that magnitude can mean a significant reduction in the remaining activity and thus the image quality that can be obtained. Off-line imaging can be characterized by the fact that all ^{15}O has decayed, meaning the main source of counts in the PET image is ^{11}C decays.

The image quality is not only degraded over time due to physical processes, but also due to biological processes. Positron emitting nuclei do not necessarily remain in the same place as where they were created. Instead, due to biological processes, they are transported to other locations, which will lower the correlation between the measured PET image and the dose distribution or the proton range. This effect, biological washout, is often modeled as an overall decrease in activity. A more in-depth overview of biological washout can be found in section 5.4.

A method that is able to measure the positron emitting nuclides more quickly is the *in-room* imaging protocol. This imaging protocol has been investigated in for instance the Francis H. Burr Proton Therapy Center (Min et al., 2013). A PET scanner is placed in the same room as where the proton therapy

treatment is delivered. After the treatment has completed, the patient can be quickly placed in the PET scanner, reducing the time between the therapy and the start of the scan to be in the order of 2 minutes. The main advantage of this method is the fact that the total activity that can be measured is higher than for off-line PET due to the shorter time delay. Also, when the patients are scanned in the same position as where they are irradiated, uncertainty in the PET image due to setup errors and registration mismatches can be reduced.

A full clinical scanner can be used in this protocol, in which care must be taken regarding radiation hardness of the components in the PET scanner. Since the scanner is in the same room as the treatment, it sees a high neutron and gamma ray background. Diblen et al. (2017) measured the degradation of dSiPM sensor performance for a scanner that would be placed *in-room*, and showed that degradation to the point when the scanner cannot be used any more takes place after an irradiation equivalent that corresponds to 3 years of operation. Techniques exist to mitigate this problem, such as switching off the damaged parts of the sensor. PET scanners based on photomultiplier tubes (PMTs) will not be affected by a comparable radiation background.

The measurement protocol that will allow the fastest feedback is *in-situ* dose delivery verification, also called *in-beam* PET. In this protocol, a dedicated scanner is integrated in the irradiation setup. An example of such a scanner is the BASTEI system that was used at the Gesellschaft für Schwerioneforschung (GSI) in Darmstadt, Germany (Crespo, Shakirin, & Enghardt, 2006; Enghardt et al., 1999). PET scanners were also installed at the facilities in Chiba and Kashiwa in Japan (Kurz et al., 2015; Nishio et al., 2010) and at the National Center of Oncologic Hadrontherapy (CNAO) in Pavia, Italy (Bisogni et al., 2017; Ferrero et al., 2018). A regular clinical PET scanner cannot be used, since space needs to be created for the beam to enter from any direction without shooting through the detectors.

Several geometries for an in-situ PET scanner have been proposed. Two iterations of the Japanese OpenPET prototypes have been built and tested: (1) dual-ring open PET, using two concentric rings with a space in the middle for the beam to enter, and (2) a slanted single ring design (Yamaya, 2017). However, the configuration that has been proposed most often is the dual-head geometry consisting of two opposing planar detectors placed close to the patient to maximize detection efficiency without interfering with the proton beam or the movement and rotation of the bed.

Known drawbacks of this dual head setup are the reduced solid angle coverage and the limited angle sampling. The reduced solid angle coverage leads to a lower detection efficiency than a full ring clinical scanner, which is somewhat mitigated by the fact that the planar detectors can be placed closer to the patient than a full ring scanner. This has a positive effect on the scanner spatial resolution, as the effect of photon acollinearity is reduced (Shibuya et al., 2007), but the parallax error is increased (Peng & Levin, 2010). The lim-

ited angle sampling of such a device degrades image quality (Vandenberghe, Mikhaylova, D'Hoe, Mollet, & Karp, 2016). Optimum tomographic imaging requires continuous angular sampling from 0 to 180°. When only a limited angular range is available, imaging artifacts occur which lead to inaccuracies in the image. The addition of time of flight (TOF) information can mitigate some of the effects of the missing angles on the image reconstruction. For example, similar limited angle PET scanner designs are in use for breast imaging. In a simulation study by Lee, Werner, Karp, and Surti (2013), good performance is shown for a scanner with 2/3 angular coverage and 600 ps TOF resolution. When the TOF resolution is improved to 300 ps, the limited angle scanner performs on par with a full ring clinical scanner without TOF information. Such a timing resolution is obtainable with current generation PET imaging hardware.

Placing the PET scanner close to the proton beam means the scanner will see a high level of radiation, which causes damage to the scanner. The performance of in-situ dSiPM sensors was measured for use in clinical irradiation conditions by Diblen et al. (2017). The increasing level of the dark count rate due to neutron radiation damage caused a high level of dead time, and correspondingly a loss of sensitivity. The dark count rate was shown to become too large for successful operation after an irradiation equivalent of only a few weeks of use. As PMTs suffer no performance degradation due to neutron damage, they seem better suited for this application

The in-situ imaging system can be used to measure during the irradiation, either while the beam is on (beam-on PET), during the beam pauses for a pencil beam scanning irradiation or in-between the beam spills of a synchrotron accelerator. PET imaging in-between synchrotron spills was introduced by Enghardt et al. (2004). The highest number of counts is obtained in in-situ imaging, as the physical decay is reduced compared to in-room or offline imaging, implying that the measurement time can be shorter, thereby also minimizing the effect of biological washout.

2.2.3 Short-lived nuclides

When an in-situ imaging system is used to measure while the beam is on or starting right after the beam is turned off, all positron emitters that were created can be seen. This means not only long-lived nuclides with a half-life larger than that of ^{10}C (19 s) play a role, but shorter-lived nuclides will also contribute to the final PET image. Dendooven et al. (2015) have measured the integrated production of these short-lived nuclides to determine which ones are relevant for proton therapy dose delivery verification.

An experiment was performed in which water, carbon, phosphorus and calcium targets were irradiated with a 55 MeV proton beam. The time-activity curve of 511 keV photons was measured each time after the proton

beam was turned off after specific beam pulse lengths. Each pulse length was optimized to detect a specific positron emitting nuclide. The most copiously produced short-lived nuclides are ^{12}N ($T_{1/2}$ = 11 ms) on carbon, ^{29}P ($T_{1/2}$ = 4.1 s) on phosphorus and ^{39m}K ($T_{1/2}$ = 0.92 s) on calcium (Dendooven et al., 2015). No short-lived nuclides were produced on oxygen. The integrated production per proton of these nuclides over the stopping of a 55 MeV proton is $4.46 \pm 0.13 \times 10^{-4}$ for ^{12}N, $1.62 \pm 0.03 \times 10^{-3}$ for ^{29}P and $4.78 \pm 0.04 \times 10^{-3}$ for ^{38m}K (Dendooven et al., 2019).

The ^{12}N nuclide is only produced in measurable quantities on carbon and not on oxygen, so the PET image one would get when measuring the ^{12}N nuclide is dependent on the carbon content of the tissue. ^{29}P and ^{38m}K are produced on calcium and phosphorus, which are mainly present in bone.

The use of these short-lived positron emitting nuclides may remedy one of the fundamental disadvantages of using PET for dose delivery verification: to obtain enough counts for an accurate measurement using these low activity distributions, the measurement time needs to be at least on the order of one half-life. When the main source of activity is ^{15}O or ^{11}C, the measurement time will be 2 to 20 min. This would make instantaneous feedback practically impossible. However, when shorter-lived nuclides are used, such as ^{12}N with a half-life of 11 ms, near real-time feedback on the dose delivery becomes possible. A potential drawback of using ^{12}N imaging is that the production yield is one order of magnitude lower compared to ^{15}O or ^{11}C. Also, the positron range for ^{12}N has a root mean square (rms) value of 18 mm in water. This means that the imaging spatial resolution will be determined by the positron range rather than the scanner performance. However, millimeter-accuracy range determination is still possible with this spatial resolution, as will be shown in chapter 3.

2.2.4 Prompt gamma ray imaging

During the proton irradiation of the patient, several nuclei are excited, or created in an excited state, which decay by the emission of a gamma ray. The emission of these gamma rays occurs on a picosecond timescale after the creation of these excited states. This means that the detection of these prompt gamma rays in principle allows real-time feedback on the dose delivery. Using prompt gamma rays to verify dose delivery was first proposed by Stichelbaut and Jongen at the yearly Particle Therapy Co-Operative Group meeting of 2003 (Stichelbaut & Jongen, 2003). This idea has developed into several distinct techniques, prototypes and clinical applications. An extensive overview of the prompt gamma ray monitoring techniques that have been developed since then is given by Krimmer et al. (2018).

The most dominant gamma rays for proton therapy have an energy of 6.13 MeV and 4.44 MeV. The 6.13 MeV gamma rays are created on ^{16}O via

the $^{16}O(p,p'\gamma)^{16}O$ reaction. For the 4.44 MeV gamma rays, contributions come from both the 4.438 MeV transition in ^{12}C resulting from the $^{12}C(p,p'\gamma)^{12}C$ and $^{16}O(p,p'\alpha\gamma)^{12}C$ reactions and the 4.444 MeV transition in ^{11}B resulting from the $^{12}C(p,2p\gamma)^{11}B$ reaction (Kozlovsky, Murphy, & Ramaty, 2002).

The spatial distributions of these discrete gamma ray lines are more strongly correlated with the Bragg peak dose profile than those of the positron emitters. This should in principle allow easier recovery of the range, and possibly the dose distribution, provided the signal quality and associated level of counting statistics are high enough. Deterioration of the signal quality for prompt gamma rays occurs due to for instance a large neutron background, which is more pronounced for heavier ions such as in carbon therapy (Testa et al., 2008) and also increases with the proton energy.

Several prompt gamma ray detector prototypes have been developed, and some are currently being tested in a clinical setting (Richter et al., 2016; Verburg & Bortfeld, 2016). The techniques employed by these prototypes vary. A mechanically collimated slit system was first proposed by Min, Kim, Youn, and Kim (2006). To optimize detection efficiency and to obtain a better camera resolution, multi-slit/multi-slat configurations have been investigated (Lopes et al., 2018; Pinto et al., 2014).

2.2.4.1 Knife-edge slit camera

A knife-edge slit camera was developed by Ion Beam Applications (IBA) (Smeets et al., 2012). The detector consists of a large tungsten knife-edge shaped slit collimator in front of lutetium-yttrium oxyorthosilicate (LYSO) scintillators, which are read out by silicon photomultipliers (SiPMs) (Perali et al., 2014). The collimator images a 1D prompt gamma profile on to the scintillators in reverse order. This is an extension to the well-known classical pinhole camera, but it uses a slit instead of a hole to obtain proton depth information. The other coordinates can be obtained on a spot-by-spot basis for pencil beam scanning via a synchronization with the beam delivery system. Clinical tests have been performed using the knife-edge slit camera at the OncoRay facility for passively double scattered proton beams (Priegnitz et al., 2016). Shifts in the proton range of 2 to 5 mm could be detected using this technique. However, only overall range deviations can be detected in this way. Very localized shifts, due to e.g. a filling of a cavity, are hard to spatially identify, since passive scattering delivers an entire proton energy layer at the same time, which can correspond to different ranges across the irradiated field. A major source of background signal in these acquisitions are the neutrons, which need to be corrected for in order to obtain the prompt gamma signal. In the discussion, it is mentioned that the majority of the neutron contribution stems from the beam line and environment of the treatment site and is not dependent on the phantom/patient geometry and composition. This would allow a measurement

protocol whereby the same irradiation is delivered to the patient with open collimator, after which it is delivered to a water phantom with a closed detector collimator to estimate and subtract the neutron background.

The knife-edge slit camera has recently been tested in a clinical setting with pencil beam scanning at the University of Pennsylvania (Xie et al., 2017). A range shift retrieval precision of 2 mm is reported, limited mainly by the accuracy of the camera positioning. To obtain this precision, spot aggregation via Gaussian smoothing with a sigma of 4 to 7 mm was incorporated, whereby contributions from neighboring spots are incorporated into the profile to increase the accuracy and precision of the range retrieval.

2.2.4.2 Compton camera

In contrast to using mechanical collimation with blocks of heavy absorbing materials, Compton cameras use electronic collimation (Everett, Fleming, Todd, & Nightingale, 1977). These cameras use a multistage detector to measure the photon scattering angle and residual energy via successive interactions in the detector. From these data, the photon point of origin can be determined to be on a cone through the use of Compton kinematics. The prompt gamma production distribution can then be reconstructed via the intersection/superposition of these cones in three dimensions. The advantage of these cameras is that for the energy range of the prompt gammas produced in proton therapy (4.44 to 6.13 MeV), Compton scattering is the dominant interaction mechanism for almost all materials. However, since the energy of the incident photons is not known in advance, full absorption of the photon needs to occur in a calorimeter, or multiple scattering events need to be recorded to completely fix the kinematics and thus the Compton cone.

2.2.4.3 Prompt gamma spectroscopy

Another method of proton range monitoring is prompt gamma spectroscopy (PGS), pioneered by Verburg and Seco (2014), which does not rely on imaging. Through analysis of the measured energy spectra at the end of the proton range for each pencil beam, information is obtained on both the tissue composition as well as the residual proton range via the steep energy dependence of the cross sections at low proton energies.

A series of simulations is performed for each delivered pencil beam as follows. Firstly, the CT of the patient is converted on a voxel-by-voxel basis to material composition and gamma attenuation. This step includes prior CT information into the range and composition detection method. Secondly, the proton energy spectra are simulated for different range error scenarios through the use of GPU-accelerated Monte Carlo simulations. The output of this simulation step is the number of protons at a specific kinetic energy

that pass through each voxel. This is analogous to what we will describe as the 4D fluence matrix in chapter 5. The fluence matrix is calculated for each range error scenario. Thirdly, the fluence matrices are used to calculate the prompt gamma ray production for each range error scenario. The production is calculated using the voxel-dependent proton energy spectra and the energy-dependent cross sections taken from experimental measurements. Fourthly, the number of detected gamma rays is calculated by correcting for gamma ray attenuation through raytracing and by modeling the detector response through Monte Carlo simulations. Finally, the range verification algorithm determines the proton range error and the material composition by a least square residual optimization over the different proton error scenarios with as free parameters the range error as well as the concentration of carbon and oxygen in the tissue material.

The detector consists of $LaBr_3$ (5% Ce doped) scintillators, read out by photomultiplier tubes and slit collimated with a tungsten collimator, looking towards the end of the proton range (Hueso-González, Rabe, Ruggieri, Bortfeld, & Verburg, 2018). In order to accurately measure both tissue composition and residual range, the amount of detected gamma rays needs to be high, meaning a high level of counting statistics is required. To increase the accuracy of the method, pencil beam spots that are delivered to the same lateral position in the field at a different energy layer which have a nominal range that differs by less than 10 mm are combined in the analysis, and their range error is calculated by simultaneously fitting the parameters for these spots in the optimization procedure.

Mixed beams where a part of the proton beam has gone through a region with a widely different stopping power than that for the rest of the beam (e.g. partly through an air cavity) also pose a problem for prompt gamma spectroscopy, since different ranges will be detected at the same time, making it difficult to estimate range and tissue composition, as the solution is not uniform in the transverse direction.

A final complication is the dependence on the CT information. Other methods, such as PET or the knife-edge slit camera, are able to determine a secondary radiation distribution range independent of the planning CT. As such, a range error compared to the planned dose delivery can also not be calculated independent from the patient CT, but when images that are taken on consecutive days are compared to each other, a change on a day-to-day basis can be detected independently. Prompt gamma ray spectroscopy requires the patient CT as input to make any sort of statement regarding proton range or tissue composition.

2.2.4.4 Prompt gamma timing

Prompt gamma timing (PGT) for range monitoring is a non-imaging method first proposed by Golnik et al. (2014). The technique is based on an accurate measurement of the transit time of protons in the patient. For protons with a penetration depth of 5 to 20 cm in the patient, the transit time is around 1 to 2 ns. Prompt gamma rays are emitted along the particle track for energies above the production threshold. The time difference is then measured between the protons passing a reference plane and the arrival of the prompt gamma rays at the detector. A histogram of this time difference is then defined as the prompt gamma ray time spectrum, which consists of contributions from the particle transit time, as well as the time of flight (TOF) of the gamma from its origination point to the detector. Since the transit time of the proton is dependent on the particle range, a longer range is generally seen as an increase in average transit time as well as in the spread of the prompt gamma ray timing distribution. Measuring statistical moments such as the mean and the standard deviation of the prompt gamma ray timing distribution thus gives information on the particle range.

The detector consists of a fast uncollimated scintillator read out by a photomultiplier tube. During tests of different prototypes of the PGT detector at a clinical IBA Cyclone 230 (C230) cyclotron, a significant drift in the proton bunches relative to the cyclotron RF phase was found on the time scale of hours (Hueso-González et al., 2015). Since the protons are bunched in a certain phase of the RF, the RF was used as a reference for the particle transit time. When the bunches drifted with respect to the RF phase, a change in the mean of the PGT spectrum of 400 ps was measured in 4 hours. This corresponds to a shift of roughly 12 cm, much larger than the millimeter precision that is needed for range verification. To counteract this effect, a beam monitor was developed based on phoswitch detectors, which was used to characterize the cyclotron beam time structure.

Another complicating factor is the proton bunch time spread (Petzoldt et al., 2016). Protons exiting the IBA cyclotron at the maximum energy have a small time spread of 230 ps at 225 MeV beam energy. To obtain lower energies, a graphite or beryllium degrader is placed close to the cyclotron exit as part of the Energy Selection System (ESS). By varying the thickness of the degrader material in the beam path and using momentum selecting slits in combination with dipole bending magnets, different energies can be selected. Since the energy loss in the degrader is a statistical process, fluctuations on a proton-by-proton basis occur. This phenomenon is known as energy straggling, which results in an increase in the momentum spread of the beam. When degrading the energy of the beam to 69 MeV, the bunch time spread increases from 230 ps to 1.4 ns. This bunch time spread is visible as a broadening of the prompt gamma timing signal, making it harder to discern small range deviations. Mo-

mentum limiting slits can be further closed to reduce the bunch width from 1.4 ns to 600 ps at 110 MeV at the cost of decreasing the beam transmission with approximately a factor of 10. This means the incident beam current needs to be increased to obtain similar output currents, or the patient needs to be irradiated longer at lower output currents.

2.2.5 Ionoacoustic imaging

A technique for proton range verification that does not depend on detecting gamma rays is ionoacoustic imaging using ultrasound, first proposed for high energy protons by Sulak et al. (1979). A first application of this technique for proton therapy dose monitoring was investigated by Tada, Hayakawa, Hosono, and Inada (1991). More recently, this work has been continued by Assmann et al. (2015); Jones et al. (2018); Jones, Vander Stappen, et al. (2016); Patch et al. (2016), and a recent overview of the field of ionoacoustics is given by Hickling et al. (2018). The ionoacoustic imaging technique exploits the thermoacoustic effect. Due to the very localized and very fast deposition of energy by a therapeutic particle beam, the temperature of the irradiated tissue can increase in the order of less than a millikelvin. This local addition of heat creates a corresponding ultrasound pressure pulse with a signal in the 0.1 to 10 MHz frequency range with a central frequency of <400 kHz. Detection of this signal can be done with relatively cheap, light-weight and small ultrasound transducers or hydrophones. Simulations showed that a single short proton spot delivering 10 to 100 mGy could be detected by a 5 cm diameter transducer. Another advantage is that the position of the Bragg peak, where most energy is deposited, is measured directly, instead of measuring a proxy of the dose as with PET or prompt gamma ray techniques.

The signal quality that can be measured by the transducers is dependent on the time structure of the beam delivery. If the delivery of the spot is shorter than the acoustic transit time to the transducer, the shape of the detected signal is determined by the shape of the dose deposition. If the delivery of the spot takes longer, the signal quality is degraded. The ideal time profile of a spot for ionoacoustic imaging, delivering the highest signal-to-noise ratio (SNR), is a Gaussian profile with a full width at half maximum (FWHM) of 5 μs (Jones, Seghal, & Avery, 2016). Also, the SNR benefits from higher instantaneous beam intensities. Currently, most clinical accelerators installed at proton therapy treatment facilities do not deliver such a beam time structure. The most widespread type of accelerator is the cyclotron, which delivers a continuous beam structure on a macroscopic level. The microstructure of the beam is determined by the bunch repetition frequency, which is determined by the RF of the cyclotron. For IBA C230 cyclotrons, the RF is 106.325 MHz, leading to a bunch repetition period of 9.4 ns. This is too fast to be seen by most transducers, so the detected time structure is entirely determined by the continuous

beam macrostructure. For synchrotron accelerators, a beam spill macrostructure is seen in the order of several seconds. This is too long compared to the ideal pulse length of 5 μs. At the CNAO synchrotron, high energy protons are accelerated with an RF frequency up to 2.4 MHz (Falbo, Burato, Primadei, & Paoluzzi, 2011), which cannot be easily detected by most transducers. The clinical synchrocyclotrons that are installed at proton therapy facilities might be beneficial for ionoacoustic imaging, as this delivers microsecond pulses at kHz repetition rates, allowing the identification of proton ranges up to 1 mm precision at Bragg peak doses of 10 Gy (Lehrack et al., 2017).

These experimental results look promising, but the main challenge for ionoacoustics to be clinically applicable is the improvement of the SNR to allow good quality measurements at therapeutic doses. Also, most experiments are still based on a transducer or hydrophone submersed in a water tank that is used as a phantom. Many complexities arise when not a homogeneous water tank is used, but a very heterogeneous patient is irradiated. The resulting pressure distribution deforms, as the pressure wave that arises from a unit heat addition is dependent on the properties of the tissue material, mainly the difference in the speed of sound, which leads to a complex system of attenuation and reflection of the waves. To compensate for this behavior, simulations can be performed based on a patient CT by converting the Hounsfield units to material properties.

An advantage of the ionoacoustic measurement technique is that a double-transducer setup can be envisioned in which an ionoacoustic transducer is coupled to a regular ultrasound imaging device to obtain co-registered anatomical information during treatment. However, as is the case for clinical ultrasound imaging, attenuation can degrade image quality for deep-seated tumors.

2.3 Conclusion

PET is the oldest method used to verify the dose delivery from particle therapy. The imaging technology is mature and will be advanced independently from its use in particle therapy as it is widely used in nuclear medicine. The disadvantage of PET is the delayed feedback due to the half-life of the radioactive decay. To image ^{15}O or ^{11}C, measurement times need to be in the order of 2 to 20 min, making instantaneous feedback impossible. When shorter-lived nuclides are imaged, this obstacle can be overcome. Especially imaging of ^{12}N can provide very fast (millisecond) feedback on the proton range, as will be shown in the following chapter.

Prompt gamma ray imaging and ionoacoustic imaging can provide real-time feedback on the dose delivery. Imaging of prompt gamma rays is more difficult from a technological standpoint than PET as only a single pho-

ton is emitted, meaning directional information can only by obtained by either mechanical collimation or a more complicated measurement of multiple interactions for a single photon. The prompt gamma rays are more difficult to detect as their energy of several MeVs is higher than the 511 keV photons used for PET. Also, the neutron background is high for prompt gamma ray imaging, as the measurement is performed while the proton beam is on.

PET has already been used to verify the dose delivery to patients in a clinical setting. Development of dedicated systems is ongoing and they are being tested at clinical sites. Some prompt gamma ray prototypes, such as PGS and the knife-edge slit camera, are currently also tested and used during patient irradiation. Ionoacoustics shows promising results, but clinical application of this technique will take more time.

Part I

Imaging of short-lived positron emitters

Chapter 3

Beam-on imaging of short-lived positron emitters during proton therapy

The following chapter was published as:
Buitenhuis *et al* 2017 *Phys. Med. Biol.* Beam-on imaging of short-lived positron emitters during proton therapy
https://doi.org/10.1088/1361-6560/aa6b8c
Some additions and modifications are implemented in this thesis.

3.1 Abstract

In vivo dose delivery verification in proton therapy can be performed by positron emission tomography (PET) of the positron-emitting nuclei produced by the proton beam in the patient. A PET scanner installed at the treatment position of a proton therapy facility that takes data with the beam on will see very short-lived nuclides as well as longer-lived nuclides. The most important short-lived nuclide for proton therapy is ^{12}N (Dendooven et al., 2015), which has a half-life of 11 ms. The results of a proof-of-principle experiment of beam-on PET imaging of short-lived ^{12}N nuclei are presented. The Philips Digital Photon Counting Module TEK PET system was used, which is based on LYSO scintillators mounted on digital SiPM photosensors. A 90 MeV proton beam from the cyclotron at KVI-CART was used to investigate the energy and time spectra of PET coincidences during beam on. Events coinciding with

proton bunches, such as prompt gamma rays, were removed from the data via an anti-coincidence filter with the cyclotron RF. The resulting energy spectrum allowed good identification of the 511 keV PET counts during beam-on. A method was developed to subtract the long-lived background from the ^{12}N image by introducing a beam-off period into the cyclotron beam time structure. We measured 2D images and 1D profiles of the ^{12}N distribution. A range shift of 5 mm was measured as 6 ± 3 mm using the ^{12}N profile. A larger, more efficient, PET system with a higher data throughput capability will allow beam-on ^{12}N PET imaging of single spots in the distal layer of an irradiation with an increased signal-to-background ratio and thus better accuracy. A simulation shows that a large dual panel scanner, which images a single spot directly after it is delivered, can measure a 5 mm range shift with millimeter accuracy: 5.5 ± 1.1 mm for 1.64×10^8 protons and 5.2 ± 0.5 mm for 8.2×10^8 protons. This makes fast and accurate feedback on the dose delivery during treatment possible.

3.2 Introduction

When a PET scanner takes data with the beam on, also very short-lived nuclides are measured. The most important short-lived nuclide for proton therapy is ^{12}N, which has a half-life of 11 ms (Dendooven et al., 2015). For carbon-rich tissue, the production is such that ^{12}N can dominate the total counts up to 70 seconds after the start of an irradiation. The short half-life, combined with the high production, makes it possible to use in-situ PET to provide feedback on the dose delivery on a sub-second timescale. So far, the integrated production of ^{12}N has been measured, but it has not yet been imaged using a PET system. The purpose of this chapter is to provide a proof-of-principle for the use of beam-on PET imaging of short-lived ^{12}N nuclei for proton therapy dose delivery verification.

3.3 Materials and methods

3.3.1 Irradiation setup

The experiment was performed at the AGOR cyclotron irradiation facility at the KVI-Center for Advanced Radiation Technology (KVI-CART), University of Groningen. This facility operates a fixed horizontal beam line. Figure 3.1 shows a picture of the experimental setup. A beam of molecular H_2^+ ions was accelerated to 90 MeV per nucleon with a bunch repetition frequency of 44.47 MHz. Directly after the exit foil at the end of the beam pipe, an air-filled ionization chamber (the beam intensity monitor, BIM) was placed to measure the beam intensity. During its calibration, the beam intensity was

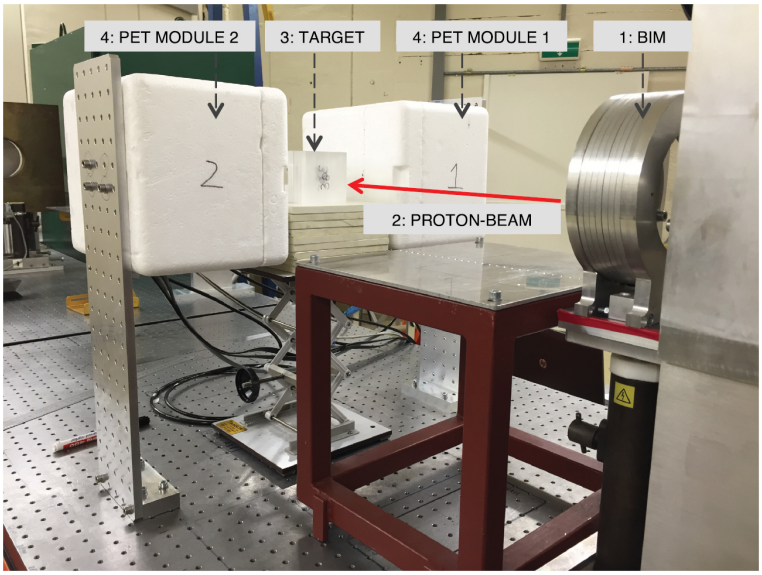

Figure 3.1: The Module TEK PET setup at KVI-CART. 1) Beam Ionization Monitor, used for measuring the beam intensity. 2) 90 MeV/u H^{2+} beam. 3) Target positioned on top of spacer plates. PMMA and graphite targets were used. 4) PET modules from the Module TEK system inside a Styrofoam box.

lowered until the number of protons could be counted with a scintillation detector. The corresponding number of monitor units (MUs) from the ionization chamber was thus related to the number of protons.

Most measurements were done at an instantaneous beam intensity of 6.2×10^8 pps. This is about one order of magnitude lower than a typical beam intensity used in clinical facilities. A beam of 2 cm full width at the target position was used. The width and position were verified using a harp-type (wire grid) beam profile measurement system.

The proton beam was stopped in two target materials: graphite and PMMA. The graphite target was a cube of $50 \times 50 \times 50$ mm^3. The PMMA target was a block of $96 \times 96 \times 110$ mm^3, with the long side of the target placed parallel to the beam direction. The proton beam was centered on the targets. Using the PSTAR database (Berger, Coursey, Zucker, & Chang, 2005), the range of 90 MeV protons in graphite and PMMA was calculated to be 4.2 cm and 5.5 cm, respectively. The targets were placed such that the PET distribution ended just after the center of the field of view (FOV) of the detectors. Vertically, the center of the detectors, the proton beam and the center of the targets were aligned. The distance between the front faces of the detector modules was 32.8 cm.

In order to disentangle the contribution of the short-lived ^{12}N from the longer-lived nuclei in the PET image, the proton beam macro structure was pulsed on a millisecond timescale. The pulsing was controlled by an arbitrary waveform generator (Tektronix AFG 3252C), which controls the voltage on a set of fast electrostatic deflection plates in the injection line of the cyclotron. This way, the beam was either deflected away from or into the cyclotron, delivering the desired time structure.

3.3.2 Module TEK PET system

The Module TEK PET system from Philips Digital Photon Counting (Haemisch, Frach, Degenhardt, & Thon, 2012) was used. This system uses lutetium-yttrium oxyorthosilicate (LYSO) scintillating crystals mounted on digital silicon photomultipliers (dSiPM). In a silicon photomultiplier, the scintillator photons are detected by an array of single photon avalanche diodes (SPAD) operating in Geiger mode. In the digital SiPMs, each microcell is able to detect only one photon per event, after which it has to be actively quenched and recharged to activate it again. The Module TEK system consists of two opposing PET modules. Each module is made from a 2×2 array of tile sensors of 32.6×32.6 mm^2. Each tile consists of a matrix of 4×4 sensor dies on the same printed circuit board (PCB), sharing a common bias voltage. Each die contains 4 pixels in a 2×2 configuration, with each pixel comprising 3200 SPADs, and a common time to digital converter (TDC) chip. The pixels are further divided into 4 sub-pixels, which are used for the trigger threshold. A LYSO crystal of $3.8 \times 3.8 \times 22$ mm^3 is coupled to each pixel, for a total of 16×16 LYSO crystals in a PET module. Since events are triggered at the level of a die, the four pixels of a die are read out at the same time. This means that an event is read out as four photon values, i.e. one for each pixel, and a common timestamp.

In order to minimize noise in the data due to thermally induced triggers, i.e. dark counts, low signal level triggers are suppressed using a trigger threshold. The system was operated in so-called trigger 4 mode, which means that all four individual sub-pixels of a pixel must see a discharge in order to generate a valid trigger. The reduction of dark-count-generated triggers in trigger 4 mode comes at the cost of degraded timing resolution. Haemisch et al. (2012) showed that in trigger 4 mode, the 50% probability level to create a valid trigger is reached after 7 photons have been detected. Since the signal level at which time pickoff is performed is relatively high, a degradation of the timing resolution follows. After the trigger threshold, a validation threshold is introduced, which is related to the spatial distribution of microcell discharges on a pixel (Frach, Prescher, & Degenhardt, 2010). The principle of operation is the same as for the trigger threshold, but the pixel is subdivided in more segments and different validation logic combinations are selectable (Haemisch et al., 2012).

To minimize the dark count rate (DCR), the system temperature was actively maintained at 3 °C using Peltier elements, a copper heat sink, and an ethanol cooling system. The modules were placed in separate Styrofoam boxes, which were continuously flushed with dry nitrogen gas to prevent condensation. The total DCR was further reduced significantly by disabling the top 20% of the microcells that exhibited the highest DCR (Somlai-Schweiger, Schneider, & Ziegler, 2015).

For our application, we need to measure the time of the PET event with respect to the cyclotron RF phase with sufficient accuracy. This creates the possibility to distinguish between events that are correlated with a proton bunch, e.g. prompt gamma rays, and events that are not correlated in time with the proton bunches, e.g. PET events. The cyclotron RF period was equal to 22.5 ns, with proton bunches of about 2 ns full width. Event timing with respect to the RF period was implemented by using the cyclotron RF signal as the clock that drives the sensor time-to-digital converters (TDC). The Module TEK accepts an external clock when a custom firmware is loaded. The clock signal needs to be delivered as a low-voltage differential signal (LVDS). The PET system stops functioning if the clock frequency is too low or too high, so a clock frequency close to the normal operating frequency of 200 MHz is preferred. The cyclotron RF frequency of 44.4652 MHz is too low to be directly used as a clock; so two passive RF frequency doublers (Mini Circuits FD-2+) were used in series to obtain a quadrupled frequency of 177.861 MHz. These doublers introduced a conversion loss of approximately 26 dB at these frequencies. To counteract this attenuation of the signal amplitude, two active wideband RF-amplifiers (Mini Circuits ZHL-1A) were used to boost the signal by 32 dB. The single-ended RF sine was then converted to a LVDS clock using a high-speed converter board from Linear Technologies (LTC6957 HMS 2), which directly fed the clock input of the Module TEK daughter board.

Data was acquired in singles mode and coincidence sorting was done off-line because of a software error in the on-board coincidence sorting algorithm. The Module TEK was connected to a data acquisition laptop by a USB 2.0 interface, which has a maximum raw signaling rate of 480 Mbit/s (Compaq et al., 2000). This is not enough to capture the full singles rate that is expected with the proton beam on, as previously noted by Cambraia Lopes et al. (2016), causing loss of data.

3.3.2.1 Time skew correction

The electronic time skew between TDC-times reported from different dies was corrected for in order to obtain the best possible coincidence resolving time (CRT). A procedure analogous to Cambraia Lopes et al. (2016) was followed to obtain the time skew corrections for all 64 × 64 die-pairs between module 1 and module 2. The distribution of time skew corrections is displayed in figure 3.2.

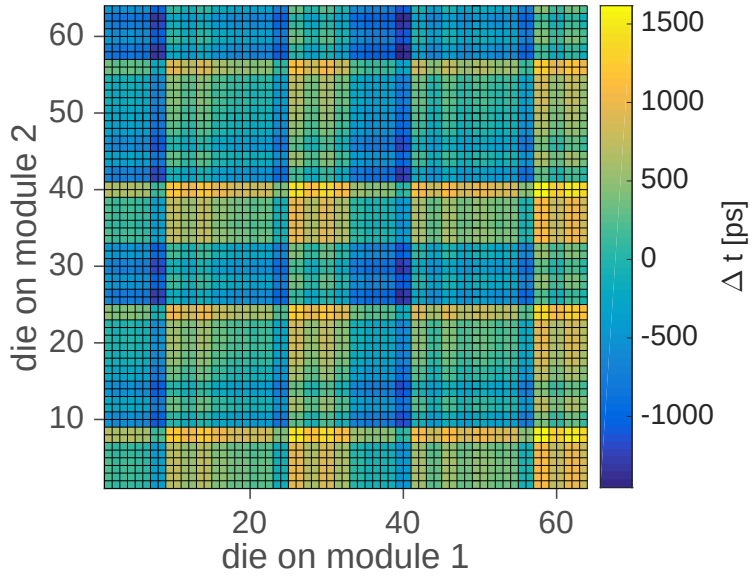

Figure 3.2: Calibration of the time skew of all die-pairs between the two detector modules. Each module comprises 4 tiles containing 16 dies each for a total of 64 dies per module.

A maximum correction of 1.62 ns was found. In trigger 4 mode applying these corrections resulted in a CRT with a full width at half maximum (FWHM) of 0.78 ns.

3.3.3 Efficiency of the detector setup

The coincidence detection efficiency of the detector setup was measured by moving a calibrated ^{22}Na source of 1 mm diameter in the midplane between the detector modules. For this purpose, it was considered a point source. The source has a strength of 382 kBq. By scanning the source from the center to the outer edge of the FOV in the x- and y-direction, the efficiency at different positions was measured. The setup can be assumed symmetrical in the top-to-bottom and the left-to-right directions. The source was thus only scanned in one quarter of the midplane using a grid of 6 × 6 points spaced 6.5 mm apart. Because of symmetry, the efficiency in the entire plane was calculated and fitted using a product of linear functions

$$\text{efficiency}(x, y) = (-a|x| + b) \cdot (-c|y| + d) \tag{3.1}$$

with a, b, c, and d parameters of the fit. The quality of the fit was evaluated using the coefficient of determination (R^2) adjusted for the number of degrees of freedom in the fit.

3.3.4 Beam-on detector performance

3.3.4.1 Beam-on singles count rate

To characterize the performance of our in-situ PET system while the beam is on, the dependence of the count rate on beam intensity was investigated. Due to the USB 2.0 bottleneck described in section 3.3.2, measuring with a continuous beam saturates the data acquisition system at fairly low beam intensities. However, it is possible to take good quality beam-on data, as we will show.

A pulsed beam with a total period of 120 ms and 50% duty cycle, resulting in 60 ms beam-on, followed by 60 ms beam-off was used. The instantaneous beam intensity, meaning the beam-on intensity, was increased from 2×10^7 pps to 5×10^9 pps in several steps. A total measuring time of 120 s was used for all acquisitions. Fresh PMMA targets were installed for each measurement, eliminating any residual activity in the target.

3.3.4.2 Beam-on spectra

To investigate the quality of the beam-on and beam-off data, energy and time spectra were taken for beams of 6.2×10^8 pps and 5.0×10^9 pps. A graphite target was installed and the beam was pulsed with a period of 89 ms and a beam-on duty cycle of 33%, meaning 30 ms beam-on followed by 59 ms beam-off. The total irradiation time was 120 s. A coincidence window of 10 ns was used. A more strict event validation setting was used during the 5.0×10^9 pps measurement, resulting in the suppression of low energy events.

3.3.5 Data analysis

Coincidence sorting was done off-line with an initial coincidence window of 10 ns. The deposited energy and the scintillation crystal in which the interaction took place was defined by the pixel with the maximum recorded energy on the triggering sensor die. Energy cuts were applied after calibrating the optical photon counts, i.e. the detector hits, at 511 keV.

3.3.5.1 Timing calculation at different time scales

Each single event is identified in time by a 16 bit frame-number, with each frame subdivided in 24 bit TDC bins. A frame lasts 368.5 μs and each TDC bin corresponds to 21.96 ps, following from the RF frequency. When the maximum frame-number or TDC bin is reached, the value is reset to 0 and starts

increasing again. The clock time since the start of the measurement was calculated using these values. Since pulsed proton beams were used, the time of the event within the beam pulse, t_{pulse}, was calculated by applying the modulus operator

$$t_{pulse} = t_{clock} \mod T \tag{3.2}$$

where t_{clock} is the clock-time, and T is the period of the pulsing cycle. The same procedure was used to calculate the time of the event with respect to the cyclotron RF signal, t_{RF}

$$t_{RF} = TDC \mod T_{bunch} \tag{3.3}$$

where TDC is the recorded TDC bin and T_{bunch} is the number of TDC bins for one RF cycle.

3.3.5.2 Prompt-gamma rejection

Prompt gamma events are directly correlated with the proton bunches. These prompt gamma counts are background in our PET application, so they need to be separated and removed from the PET counts. Prompt counts are detected during proton bunches, so a histogram was made of the number of counts vs. t_{RF}. The events in the prompt peak were removed from the data stream using an anti-coincidence filter.

3.3.5.3 ^{12}N nuclide detection

^{12}N was identified using the time t_{pulse}. During each beam-on part of a pulse, long-lived and short-lived positron-emitting nuclei are produced and the resulting PET count rate grows on top of a prompt background. When the beam is turned off, the prompt background stops and the PET detectors only detect the radioactive decay of the positron-emitting nuclei. At the time scale of the beam pulsing, the longer-lived nuclides are expected to be seen as a constant background per pulse period under a clearly visible ^{12}N decay ($t_{1/2}$ = 11 ms). As the irradiation progresses, the background from the longer-lived nuclides increases.

A pulsed beam of 6.2×10^8 pps instantaneous beam intensity was used on a graphite target. The total irradiation time was 120 seconds, using a pulsing period of 89 ms. The beam was off from 0 – 59 ms and on from 59 – 89 ms. A coincidence window of 6 ns was applied to the data, and the full energy peak was selected via an energy window of 300 – 650 keV for both detectors. The coincidences corresponding to the prompt gamma rays are cut out of the data using the anti-coincidence filter. The remaining non-prompt PET data was then used to make the time distribution of PET counts within the pulsing cycle.

The total number of detected counts corresponding to ^{12}N nuclei was calculated by fitting the beam-off part of the time spectrum of the coincidences with a ^{12}N decay curve. The decay curve used is

$$A(t) = A_0 \exp(-\lambda_{N_{12}} t_{pulse}) + C \tag{3.4}$$

with A the measured time-activity profile, A_0 the ^{12}N activity at the start of the beam-off period, $\lambda_{N_{12}}$ the known decay constant of ^{12}N, and C the constant activity on this timescale due to longer-lived nuclei. The total number N of measured ^{12}N counts is given by

$$N = \frac{A_0}{\lambda_{N_{12}}} \tag{3.5}$$

3.3.5.4 Imaging

Two-dimensional imaging was implemented by plotting a 2D histogram of the intersection points of the lines of response (LOR) with the midplane between the two detector modules. The width of the positron annihilation spatial distribution is determined by the proton beam size and the positron range. The proton beam full width was about 2 cm, with an RMS width of about 4 mm. For ^{12}N with a 1D RMS range of 18 mm in water (Dendooven et al., 2015), corresponding to 10.6 mm in graphite, the positron range is the main contribution to the width of the annihilation spatial distribution. As the width of this distribution is much smaller than the distance between the detectors, using the two-dimensional imaging method is justified.

A sensitivity correction was applied to the image by dividing the pixel value in the image with the measured efficiency at that point. The sensitivity correction factors were normalized such that the correction factor in the center of the FOV was equal to 1. More sophisticated image reconstruction techniques, such as 3D maximum-likelihood expectation-maximization (MLEM) will in general produce better images. However, for fast range verification on the level of single pencil beams, a 3D reconstruction method is not necessary and will make near real-time feedback impossible.

3.3.5.5 Separation of short- and long-lived nuclides

There is no way to tell whether a coincident event stems from a short-lived or a long-lived nucleus. They both emit a positron that annihilates and emits indistinguishable 511 keV photons. The method used to separate the two contributions is based on half-life analysis. The same irradiation properties as in section 3.3.5.3 were used. An energy window of 300 – 650 keV and a coincidence time window of 6 ns were applied to the data. The first step was to make an image using t_{pulse} from 0 – 40 ms. This contains coincidences that are detected just after a beam pulse has ended, i.e. where the contribution from ^{12}N

is highest. The second step was to make an image using t_{pulse} from 40 – 59 ms. Since the half-life of ^{12}N is 11 ms, this image starts after almost 4 half-lives of ^{12}N. Only 8% of the ^{12}N is left at the start of the second image, which means that its contribution is minimal. Mostly long-lived nuclei are present in this image. The ^{12}N distribution was then calculated by subtracting the long-lived image from the first image, after applying a weighting factor w to the second image of

$$w = \frac{\Delta t_1}{\Delta t_2} = 2.11 \tag{3.6}$$

with Δt_1 and Δt_2 the length of the time window of the first and the second image, respectively. This factor is applied since the number of counts of the long-lived nuclides scales with the length of the time window.

3.3.5.6 Detection of proton range shifts

Measurements were done for two positions of the target that differ by 5 mm in the beam direction. The 50% distal fall-off position x_0 was measured by fitting the distal edge of a 1D projection with a sigmoid function

$$S(x) = \text{base} + \frac{\max}{1 + \exp(\frac{x_0 - x}{\text{rate}})} \tag{3.7}$$

The measured range shift between the two target positions is then defined as the difference between the 50% distal fall-off positions.

3.3.6 Simulation of ^{12}N imaging for a large scanner

A simulation study using the GATE simulation framework (Jan et al., 2004) was performed to estimate the precision and accuracy with which a proton range shift of 5 mm can be seen using ^{12}N imaging with a large dual panel scanner. A single spot from the distal energy layer of an irradiation was simulated, containing 5×10^8 instantaneously delivered protons of 90 MeV. A separate simulation was performed for a spot of 1×10^8 protons. Although the simulations were performed on the basis of the amount of protons described above, the results are rescaled to incorporate the adjusted proton production reported in the corrigendum of the short-lived nuclides production paper (Dendooven et al., 2019). This means the precision and accuracy of the proton range shift correspond to a rescaled delivery of 1.8×10^8 and 8.2×10^8 protons. The imaging procedure started directly after the protons were delivered, and the imaging period was such that all ^{12}N had decayed. Assuming that the distal layer is delivered first, the number of counts from long-lived nuclides is much smaller than that from ^{12}N (Dendooven et al., 2015); long-lived nuclides were therefore ignored in the simulation. In order to be able to compare with the experimental

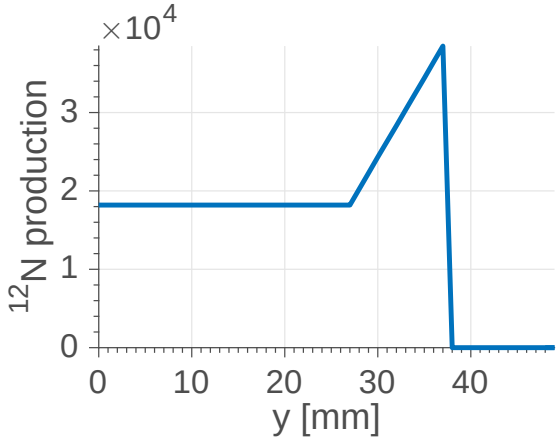

Figure 3.3: An approximation of the ^{12}N production per mm in the beam direction of 5×10^8 protons of 90 MeV on a graphite target used for the GATE simulation study. The transversal direction was a Gaussian shape with a sigma of 3 mm.

results, the phantom consisted of the same graphite target that was used for the experimental measurements, i.e. a $50 \times 50 \times 50$ mm^3 block with a density of 1.7 g/cm^3. Since the ^{12}N production cross-section as a function of energy is not well known, the ^{12}N distribution in the beam direction was approximated by a flat production from 90 – 48 MeV, a linear increase between 48 – 21 MeV, after which the production goes to zero, as seen in figure 3.3. The linear increase was based on a fit to the cross-section data from Rimmer and Fisher (1968). The transversal profile was equal to a Gaussian with a sigma of 3 mm. An overall scaling factor was applied to obtain the experimental value of ^{12}N produced by a 55 MeV proton as measured by Dendooven et al. (2015). The positron energy distribution was implemented according to equation 9.25 from Krane (1988) and the positron stopping process was included in the simulation.

The scanner was a dual panel PET system centered on the target with a separation between the two panels of 40 cm. Each panel was comprised of a 52×52 array of LSO crystals with a size of $4 \times 4 \times 20$ mm^3. An energy resolution of 13% at 511 keV and a timing resolution of 500 ps were used. Coincidences were selected using an energy window of 400 – 650 keV and a coincidence time window of 4.5 ns. Simulations were done for two positions of the target that differ by 5 mm in the beam direction. Imaging and detection of proton range shifts were performed as described in section 3.3.5.4 and 3.3.5.6.

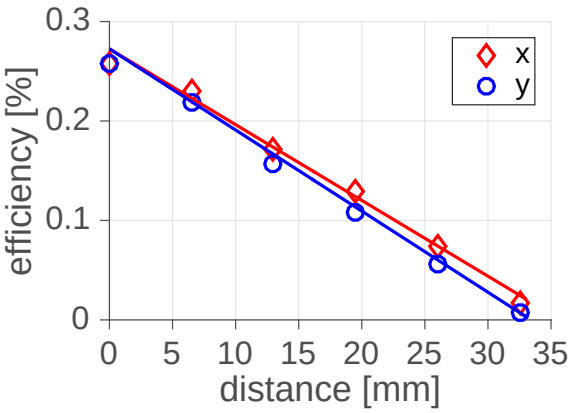

Figure 3.4: Coincidence detection efficiency in the midplane between the detectors along the horizontal (x) and vertical (y) axes as a function of the distance from the center of the FOV. The lines show the result of a fit applied to the data according to equation (1).

3.4 Results

3.4.1 Efficiency of the detector setup

The measured coincidence detection efficiency along the central axes in the midplane between the detectors is shown in figure 3.4. The fit, applied to all the 6×6 data points, corresponds to equation (1) with parameters $a = 0.015\ \text{mm}^{-1}$, $b = 0.54$, $c = 0.015\ \text{mm}^{-1}$, and $d = 0.50$, which gives the detection efficiency in percent. The adjusted coefficient of determination for this fit is $R^2 = 0.9938$, which means the fit is very good. A maximum efficiency of 0.27% is reached in the center of the FOV.

3.4.2 Beam-on detector performance

3.4.2.1 Beam-on singles count rate

Figure 3.5 shows the singles count rate of the entire PET system, as a function of instantaneous beam intensity for the PMMA target, averaged over the 120 s irradiation (labeled "all") as well as the average singles count rates during the beam-on and beam-off periods separately. The beam-off count rate grows linearly with the beam intensity.

At a beam intensity of approximately 0.5×10^9 pps, the beam-on count rate starts to saturate, resulting in a decreasing beam-on count rate after 3.5×10^9 pps. Using a linear fit of the first two points, the slope of the beam-on

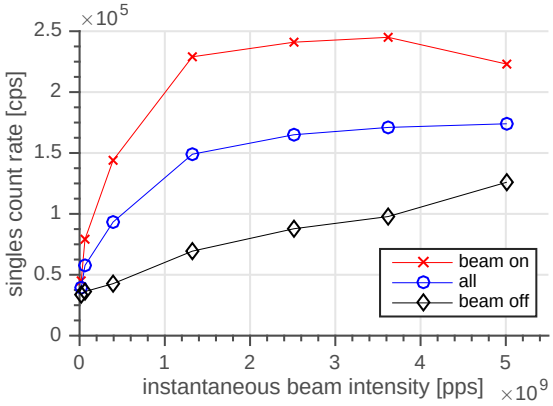

Figure 3.5: Singles count rate as a function of instantaneous beam intensity on a PMMA target, when using a pulsed beam of 120 ms period, 50% duty cycle, and a total irradiation time of 120 s. Shown are the count rate averaged over the 120 s irradiation ("all") as well as the average singles count rates during the beam-on and beam-off periods separately

count rate at low beam intensities is equal to 7.7×10^{-4} counts/incident proton. Since the saturation at low intensities is minimal, this value can be used to estimate the total singles count rate an in-situ PET scanner has to handle during beam-on. The total solid angle coverage of our detector setup using two heads is approximately 0.27 steradian. The expected singles count rate during beam-on for any scanner configuration is then calculated to be 2.9×10^{-3} count/(incident proton × sr). The offset of 0.30×10^5 cps at zero beam intensity is caused by the intrinsic radioactivity of the LYSO crystals.

Natural lutetium contains the radioactive isotope ^{176}Lu, which decays at a rate of 200 Bq per cm^3 of LYSO. For the crystal volume of 163 cm^3 LYSO of the entire system, the background radioactivity is thus equal to 0.33×10^5 Bq. Since these decays happen inside the scintillation crystals, practically all of them will produce a valid trigger on the sensor die and end up in the data stream.

3.4.2.2 Beam-on spectra

The energy and time spectra are shown in figure 3.6. Using a linear energy calibration with only the 511 keV photopeak, the energy spectra end at 1280 keV. This represents full saturation of the dSiPM sensors, when all microcells on a pixel have discharged. The 1275 keV peak from ^{22}Na falls within this saturation region. It is possible to correct the energy calibration for this saturation effect, but since only the identification of the 511 keV photopeak is of importance for

PET, no correction was applied.

Figure 3.6(a) shows spectra of all recorded coincidences of this measurement. The FWHM of the timing spectrum for the measurement at a beam intensity of 6.2×10^8 pps is equal to 1.1 ns. This timing spectrum is worse than the spectrum measured at an intensity of 5.0×10^9 pps, since the full width at tenth of maximum (FWTM) is larger. This broadening of the peak is due to the higher fraction of low energy photons in the data set. In general, lower energy photons will have a broader coincident time peak caused by the fixed level of time pickoff. These low-energy photons are suppressed in the measurement at an intensity of 5.0×10^9 pps, because a higher validation setting was used.

The full data set was then divided in beam-off and beam-on coincidences. Figure 3.6(b) shows spectra for coincidences recorded during the beam-off period (59 ms), while figure 3.6(c) shows the spectra during the beam-on period (30 ms). The FWHM of the time spectrum for the beam-off data of the measurement at an intensity of 6.2×10^8 pps is 1.0 ns, and for the beam-on data it amounts to 1.5 ns.

The beam-on data contain contributions from PET annihilations as well as prompt gamma rays, which are directly correlated in time with the protons. Applying an anti-coincidence constraint with the proton bunches removes most of the prompt counts. This procedure is shown graphically in figure 3.7. The prompt counts are separated and removed from the non-prompt counts. Coincidences with at least one event between t_{RF} bin number 600 and 750 are marked as prompt and removed from the data stream. Some events outside this window are also removed, since they are part of a coincidence where the other event is inside the window. The amount of removed events outside of the window depends on the CRT of the detectors, and the size and position of the source between the detectors. Figure 3.6(d) shows the spectra of the beam-on data with the anti-coincidence constraint applied. Most photons with energies above 511 keV are removed using this technique. A sharp 511 keV photopeak remains and the total energy spectrum looks identical to the beam-off spectrum (Figure 3.6(b)). The time-spectrum of the 6.2×10^8 pps measurement is also improved to a FWHM of 1.1 ns. Figure 3.6(e) shows the data that was removed using the constraint, i.e. the counts that are in coincidence with the proton bunches. The FWHM of the time distribution of the 6.2×10^8 pps measurement is 1.6 ns.

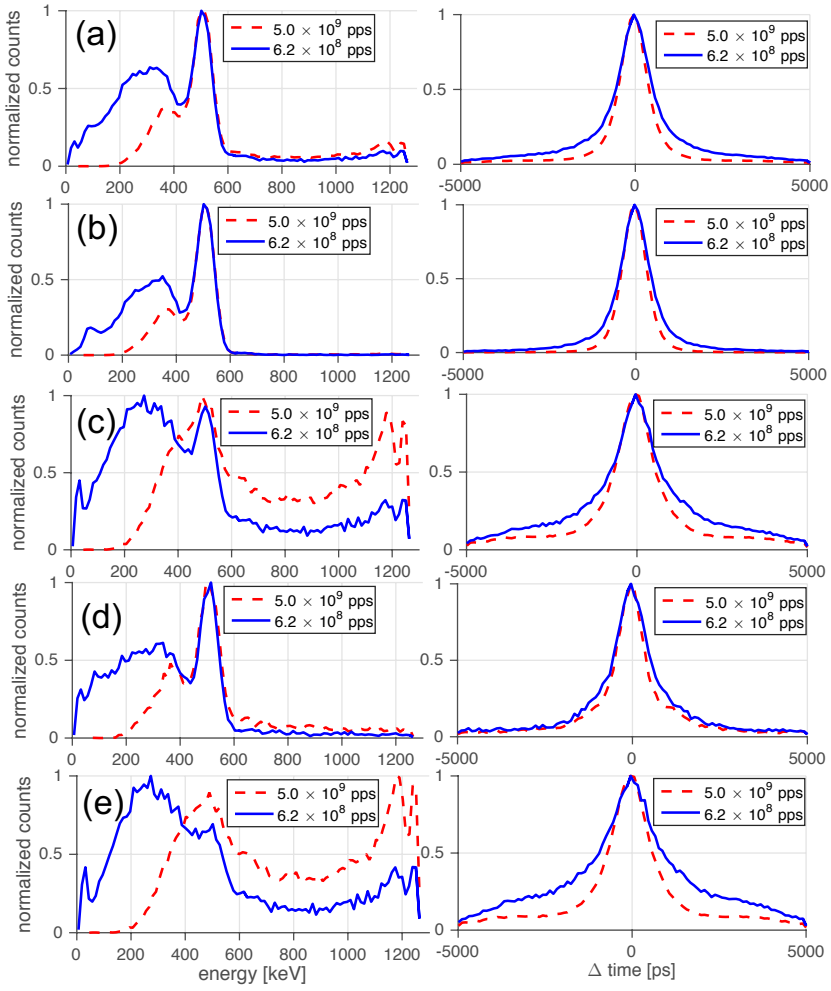

Figure 3.6: Energy (left) and time (right) spectra of coincidences in a pulsed irradiation using the graphite target. The spectra are normalized to their own maximum. (a) All data. (b) Data from the beam-off period (59 ms). (c) Data from the beam-on period (30 ms). (d) Coincidences from the beam-on period that do not coincide with a proton bunch. Prompt gamma counts are removed. (e) Coincidences from the beam-on period that do coincide with a proton pulse, mainly prompt gamma related coincidences

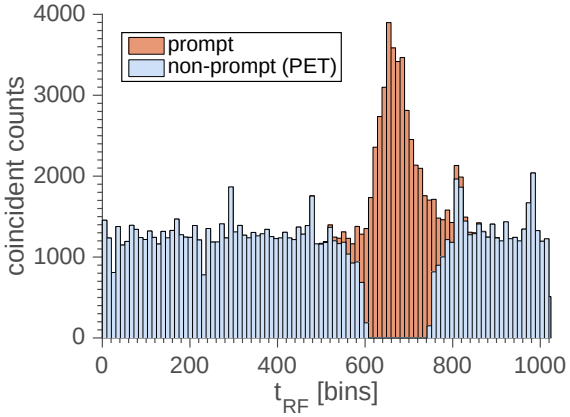

Figure 3.7: Distribution of coincident events over the RF cycle of 1024 TDC bins using the graphite target with a beam intensity of 6.2×10^8 pps. The t_{RF} of both events comprising the coincidence is shown. Events coinciding with the proton bunch can be seen around bin number 700.

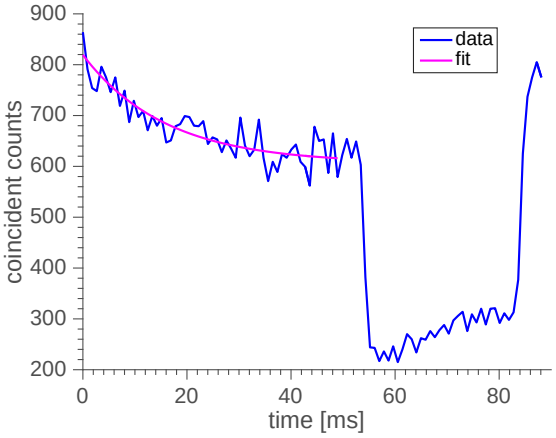

Figure 3.8: Distribution of coincident events as a function of t_{pulse} for a graphite target. The beam is off from 0-59 ms, and on from 59-89 ms. A fit of the ^{12}N decay during the beam-off period is shown.

3.4.3 ^{12}N nuclide detection

The coincidence counts vs. t_{pulse}, measured as explained in section 3.3.5.1, are shown in figure 3.8. When the beam was turned on at t_{pulse} = 59 ms,

the coincident count rate decreased from 6.2×10^2 counts per 0.89 ms bin to 2.2×10^2 counts per bin, which is a reduction of 65%. This indicates a loss of PET data by this amount during beam-on due to the data transfer limit (see section 3.3 and 3.9). A fit of the ^{12}N decay was performed from 0 – 50 ms. The total number of ^{12}N counts above the constant activity due to the longer-lived nuclides is 4.0×10^3.

3.4.4 Imaging, separation of short- and long-lived nuclei

The results of the 2D ^{12}N imaging procedure from section 3.3.5.4 are displayed in figure 3.9. The ^{12}N image (figure 3.9(c)) contains mostly positive pixels, which indicates a net contribution of ^{12}N counts. Negative values occur due to statistical fluctuations.

One-dimensional projection profiles on both axes are shown in figure 3.10. The ^{12}N profiles as seen in figure 3.10(c) are in both the x– and y–direction broader than the profiles of the longer-lived positron emitters in figure 3.10(b). Figure 3.10(d) is a comparison of the long-lived and ^{12}N profiles for the first target position (labeled as "0 mm"). A widening of the profiles is clearly seen. The width (RMS) of the sensitivity corrected transversal profile is 8 ± 3 mm for the long-lived positron emitters and 12 ± 3 mm for ^{12}N. The quadratic difference of 9 ± 5 mm is interpreted as being due to the range of the ^{12}N positrons, which have a 1D RMS range of 10.6 mm in graphite. This is consistent with the measured increase in the width of the transversal profile. The 1D RMS positron range for ^{15}O, the nuclide that provides most of the long-lived contribution, is 0.7 mm in graphite and thus negligible with respect to both the beam width and the PET scanner spatial resolution.

A sigmoid was fitted to the distal edge of the profiles in the beam direction for the images of the long-lived positron emitters (figure 3.10(b)) and ^{12}N (figure 3.10(c)). The proton range shift of 5 mm was measured by the difference in the x_0 parameter of the fit. For the profiles of the long-lived nuclides in figure 3.10(b), a shift of 5.6 ± 0.4 mm is measured between the two target positions, while a shift of 6 ± 3 mm is found for ^{12}N in figure 3.10(c).

3.4.4.1 Simulation of ^{12}N imaging for a large scanner

The results of the simulations of 90 MeV protons stopped in a graphite target that is imaged by a large dual panel PET scanner (see section 3.3.6) are displayed in figure 3.11. For a spot of 8.2×10^8 protons, the total number of detected coincident counts is equal to 1.2×10^4. The whole positron emitter distribution falls within the FOV of the detector, so the loss of counts at the entrance of the target (around y = -30 mm) due to positron escape is visible as a steeper decrease compared to the distal edge of the ^{12}N profile (at y = 14 mm). The shift of the target by 5 mm was measured by the x_0 parameter of the sig-

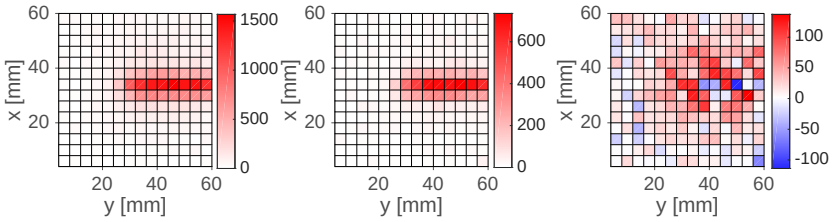

Figure 3.9: 2D images of the coincident counts for the first target position of the graphite target. The beam enters from the right in the $-y$ direction. A PET detection sensitivity correction was applied. (a) The image is made using t_{pulse} from 0 – 40 ms, including both ^{12}N and long-lived nuclei. (b) The image is made using t_{pulse} from 40 – 59 ms, including mostly long-lived nuclei. (c) The ^{12}N image is obtained by subtracting the weighted long-lived image from the first image.

moid (equation 7) that was fitted to the distal edge. A shift of 5.2 ± 0.5 mm is found. When the same procedure was applied for a spot of 1.64×10^8 protons, a shift of 5.5 ± 1.1 mm is found.

3.5 Discussion

3.5.1 Beam-on detector performance

From the singles count rates, figure 3.5, it can be seen that the count rate of the Module TEK suffers from saturation above a beam intensity of approximately 0.5×10^9 pps. Not all events are transmitted by the data acquisition system. The beam-on singles count rate even decreases for intensities beyond 3.5×10^9 pps. However, the beam-on data that is transmitted is of good quality; see figure 3.6. Once the prompt events that coincide with the proton bunches are removed from the data via an anti-coincidence filter, high-quality PET energy and time distributions result. This shows that it is possible to take good PET data during beam-on by removing prompt counts using the anti-coincidence filter.

Helmbrecht et al. (2016) point out that for typical PET block detectors, it is challenging to perform prompt-gamma-ray-free imaging, due to pile-up of positron annihilation photons and prompt gamma rays. They used a PET detector with LSO crystals and a cyclotron with a proton bunch repetition period of 9.4 ns and a proton energy dependent bunch duration of 0.2 – 2 ns. LSO has a characteristic decay time of 40 ns. So if a prompt gamma ray is detected, it is not possible to detect a 511 keV photon using the same detector without pile-up before the next proton bunch. Whether a detector can be used for beam-on PET then depends on this pile-up probability, which in turn depends on the count rate and thus detector surface area. Helmbrecht et

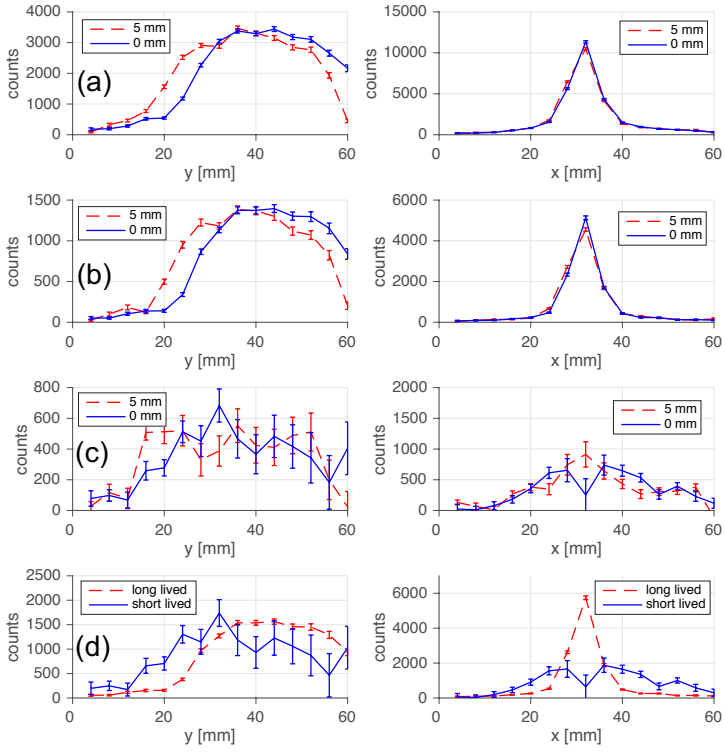

Figure 3.10: 1D projection profiles of the 2D images of figure 3.9 for the first target position (labeled as "0 mm") and for the target shifted by 5 mm. The beam enters from the right in the -y-direction. The x-direction is transversal to the beam. The profiles are normalized to an equal number of total counts. (a) t_{pulse} from 0 – 40 ms. (b) t_{pulse} from 40 – 59 ms. (c) ^{12}N profile. (d) Comparison of the long lived and ^{12}N profile for the "0 mm" target position.

al. use a Siemens PET block detector of 52 × 52 mm^2 at 18.5 cm from the beam. The count rate measurements that we have presented show a count rate of about 55 kcps per cm^2 detector area at 18.5 cm distance from a 1 nA beam. For the block detector, this means a count rate of about 1.5 Mcps. In this case, a beam-on 511 keV PET count will often be summed with a prompt gamma count. Helmbrecht et al. mitigate this problem by a pile-up rejection technique that removes these events. The PDPC Module TEK PET system we used is based on dSiPMs that are read out at the level of a die. This basic detector unit

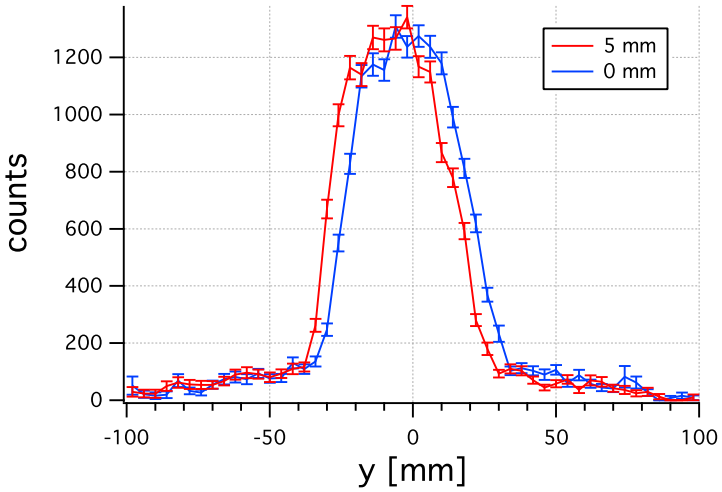

Figure 3.11: 1D ^{12}N profiles from simulations of 90 MeV protons stopped in a graphite target that is imaged by a large dual panel PET scanner. The instantaneous delivery of 9.3×10^8 protons in a single beam spot is assumed. Protons travel from the left in the positive y-direction. Profiles for two target positions shifted by 5 mm in the -y-direction are shown.

has a surface area of about 0.6 cm^2, greatly reducing the pile-up with prompt gamma rays. The measurement at a near-clinical instantaneous beam intensity of 5.0×10^9 pps shows that it is possible to use the anti-coincidence filter to obtain good 511 keV identification and prompt-gamma rejection.

For shorter proton bunch periods, the prompt gamma ray time window represents a larger fraction of a period and consequently a smaller fraction of PET events will pass through the anti-coincidence filter. Higher energy protons, due to a slowing down time in the order of nanoseconds, exhibit a broadening of the prompt gamma time peak, again reducing the fraction of PET events that pass through the anti-coincidence filter. For example, the Ion Beam Applications (IBA) C230 fixed-energy cyclotron, which is widely used in proton therapy, has a bunch repetition period of 9.4 ns and a bunch duration of 0.2 ns FWHM at its maximum energy of 230 MeV up to 2 ns at 70 MeV (Petzoldt et al., 2016). The longer slowing down time of higher-energy protons is in a sense compensated by the shorter bunch duration. To investigate the influence of these two properties on the anti-coincidence filter, an average value of 150 MeV with a bunch duration of 1 ns is used. The slowing down time of 150 MeV protons in a PMMA target is approximately 1.3 ns according to figure 2 of Golnik et al. (2014). These effects need to be combined with

the PET time resolution of approximately 0.5 ns FWHM. The time resolution can be quadratically summed with the bunch duration, which leads to a bunch duration of 1.1 ns FWHM. This can be convolved with the slowing down time of 1.3 ns, leading to a prompt gamma pulse with a full width of approximately 2.4 ns. If the anti-coincidence window is increased by 0.5 FWHM on each side to capture the full prompt gamma peak, 3.5 ns are discarded out of a total period of 9.4 ns. This would lead to a decrease in the accepted PET count rate during beam-on of 37%. So when using the clinical beam structure of the IBA C230 cyclotron, it would still be possible to use the anti-coincidence filter to remove prompt counts from the beam-on data.

3.5.2 Imaging

To obtain an image of only the ^{12}N nuclides, a method was developed to subtract the long-lived background from the image including ^{12}N. An increase of 9 ± 5 mm in the transversal size of the ^{12}N PET profile was measured, which is consistent with the ^{12}N positron range in graphite of 10.6 mm RMS. The same effect plays a role in the beam direction as well, causing a broadening of the distal edge. However, a broadening of the distal edge can also be due to a different energy dependence of the ^{12}N production cross section compared to production cross sections of the long-lived nuclides.

Dendooven et al. (2015) show that the PET signal during the delivery of the distal layer of a patient irradiation (in case it is delivered first) will be largely dominated by ^{12}N. In our measurements, the low detection efficiency of the PET system was in a sense compensated by a long measurement time of 120 s. Due to this long measurement time, the number of counts from long-lived nuclides was much larger than it would be in a clinical irradiation of a distal layer. The resulting large correction for long-lived nuclides contributes to the uncertainty in the ^{12}N profiles. A simulation was performed to estimate the improved uncertainty in a clinical irradiation of a distal layer. When simulating a large dual panel scanner that focuses on the distal edge of the ^{12}N production, 1.2×10^4 coincident counts are detected for a spot of 9.3×10^8 protons. This is a few times more than in the measurements presented where we obtained ^{12}N 1D profiles containing about 4.0×10^3 counts (see section 3.10). The simulations demonstrate that a large dual panel scanner, imaging a single spot from a clinical irradiation directly after it is delivered, can measure a 5 mm range shift with millimeter accuracy: 5.5 ± 1.1 mm for 1.8×10^8 protons and 5.2 ± 0.5 mm for 9.3×10^8 protons. Due to the absence of a long-lived contribution and the higher number of counts, this is substantially better than the shift of 6 ± 3 mm deduced from the experiments presented in this work. The accuracy of this method can be compared to that of the knife-edge slit prompt gamma camera, which is the prompt gamma ray imaging device closest to clinical implementation. Figure 17 of Perali et al. (2014) shows that approximately

1×10^9 protons of 100 MeV are needed to obtain a precision of 0.5 mm (1σ), and 2×10^8 protons are needed for a precision of 1 mm (1σ). The ^{12}N imaging technique can thus reach the same precision using an equal number of protons.

3.5.3 Clinical implementation and cost

During a patient irradiation, one could separate ^{12}N from the long-lived nuclides by for instance introducing an artificial beam-off period of 100 ms every second, or by extending the spot-switching time between different spots in a pencil beam scanning irradiation, or by using the PET data measured in-between synchrotron spills or in-between energy layers. This way, contributions from previous irradiation fields are also removed, thus providing ^{12}N PET images free from contamination from earlier fields. Integration over (part of) the distal edge can be used to obtain better statistical accuracy, with the drawback of averaging the proton range measurement over a larger area.

Using ^{12}N imaging, accurate feedback on the dose delivery can be obtained within seconds after the start of the treatment. This technique can thus be used for on-line adaptive treatment or as an immediate indicator for off-line replanning, just as any dose delivery verification technique based on prompt gamma rays. All these techniques can potentially stop an irradiation in (near) real time when a deviation from the intended dose delivery is measured. In a more sophisticated implementation, one can envision an automatic feedback to the beam delivery system to e.g. slightly adjust the beam energy to the measured proton range. An interesting option is to use a carefully selected set of "pilot" spots from the distal layer for which the time structure is optimized for ^{12}N imaging, by e.g. allowing a sufficiently long time between these spots. If no deviations are detected using these pilot spots, one can have some confidence that the full irradiation will be delivered as intended. If deviations are detected, the treatment plan might, depending on the nature of the deviations, be recalculated on-line after which the irradiation can be completed. For example, an overall range deviation due to the uncertainty in the translation of planning CT to proton stopping power could be instantly corrected. The same in-situ PET system can also be used to acquire a separate image after the dose has been delivered, in the same way as PET is nowadays in use in a few therapy facilities. Such an image will be of better quality than the ^{12}N image due to the improved spatial resolution and statistics, and can be used for off-line adaptive treatment.

Cost is an important aspect of the implementation of *in vivo* dose delivery verification. In the following, we investigate a number of relevant factors in the comparison of an in-situ dual panel PET system with the prototype of the knife-edge slit prompt gamma camera (Perali et al., 2014). Both systems are based on comparable scintillation detectors: 2 to 3 cm thick LSO/LYSO scintillators read out by a suitable photosensor (photomultiplier tubes or SiPMs).

As the PET scanner has a larger surface area, the material cost of the PET system is expected to be higher. For the PET scanner described in section 3.7, the total LSO scintillator volume is 1.7 dm^3. The prompt gamma camera contains 0.5 dm^3 of LYSO, but a thick tungsten collimator is needed, partially offsetting the lower detector cost. We show in this paper that modern PET technology is suitable for proton therapy, even for beam-on imaging. Regular off-the-shelf PET modules can thus be used to construct an in-situ scanner. This application will directly profit from the technological advancements in PET imaging used for nuclear medicine. Concerning integration in the irradiation environment, we see no substantial difference between a dual panel PET scanner and a prompt gamma imaging device.

3.6 Conclusion

We have provided a proof-of-principle for the PET imaging of ^{12}N as a tool for proton therapy dose delivery verification. Using a PET system with a small detector unit surface area, pile-up between 511 keV annihilation photons and prompt gamma rays is limited and it is possible to reject events coinciding with proton bunches for prompt-gamma-ray-free PET imaging. A method was developed to subtract the long-lived background from the ^{12}N image by introducing a beam-off period into the cyclotron beam structure. Since the ^{12}N image disappears with a half-life of 11 ms, an estimate of the long-lived image can be obtained 40 ms after the beam is turned off. This background image can then be subtracted from the ^{12}N image. A range shift of 5 mm was measured as 6 ± 3 mm using the ^{12}N profile. A larger, more efficient, PET system with a higher data throughput capability will allow beam-on ^{12}N PET imaging of single spots in the distal layer of an irradiation with an increased signal-to-background ratio of the ^{12}N image and thus better accuracy. A simulation shows that a large dual panel scanner that images a single spot at the beginning of the dose delivery, can measure a 5 mm range shift with millimeter accuracy: 5.5 ± 1.1 mm for 1.64×10^8 protons and 5.2 ± 0.5 mm for 8.2×10^8 protons. This makes fast and accurate feedback on the dose delivery during treatment possible.

Chapter 4

Short-lived PET nuclide imaging of bone-like targets

4.1 Introduction

A similar experiment as in the previous chapter was performed to investigate the imaging of short-lived nuclides produced on bone. Since bone contains the elements calcium and phosphorus, which are not present in soft tissue, additional positron emitting nuclides are produced when bone is irradiated. Proton beams usually do not stop in bone, but they might pass through bone on their way to the tumor. Imaging of the nuclides produced on bone can give additional anatomical information on a timescale of several seconds, as demonstrated by Hsi et al. (2009). In Dendooven et al. (2015), the most copiously produced short-lived nuclides produced on calcium and phosphorus are identified. The production of these nuclides as measured by (Dendooven et al., 2019) is shown in table 4.1.

Table 4.1: Short-lived nuclides produced on phosphorus and calcium targets during the stopping of a 55 MeV proton.

nuclide	$T_{1/2}[s]$	target	production per 55 MeV proton
^{29}P	4.14 s	phosphorus	$1.62 \pm 0.03 \times 10^{-3}$
^{30}S	1.18 s	phosphorus	$3.9 \pm 0.4 \times 10^{-4}$
^{38m}K	924 ms	calcium	$4.78 \pm 0.04 \times 10^{-3}$

4.2 Experimental setup

A phantom was designed to mimic an irradiation of bone embedded in soft tissue. The phantom, as shown in figure 4.1, consists of three regions. First, an entrance region comprised of 3 cm PMMA with a density of 1.18 g/cm^3. The second region consists of compacted calcium phosphate powder ($Ca_3(PO_4)_2$) with a density of 0.84 g/cm^3 in a thin plastic box embedded in a PMMA slab of 1 cm. Calcium phosphate is used as a target material as it contains an equivalent amount of P and Ca atoms per cubic centimeter as cortical and compact bone. The beam is stopped in a thick PMMA absorber of 6 cm. The size of the target perpendicular to the beam was 7×7 cm^2. The range of the 90 MeV proton beam in this phantom was calculated using SRIM (Ziegler, Ziegler, & Biersack, 2010) to be 5.9 cm. The placement of the detectors and the beamline was identical to what was described in chapter 3. The target was placed such that the calcium phophate insert was in the center of the FOV of the detector. An instantaneous beam intensity of 8×10^8 pps was used. The target was refreshed after each experiment by replacing it with identical components that had not (recently) been irradiated. However, as only one thick PMMA absorber of 6 cm was available, this part of the target was not refreshed.

4.3 Data analysis

Data were recorded in singles mode and coincidence sorting was applied offline. A coincidence window of 6 ns and an energy window of 300 – 650 keV were used to select the photopeak of coincident events. Data analysis was performed similar to described in chapter 3.

4.3.1 Detection of short-lived nuclides

During the irradiation of the target, both short-lived and long-lived nuclides were produced. Besides the short lived nuclides, ^{29}P, ^{30}S and ^{38m}K, the following long-lived nuclides were produced: ^{10}C ($T_{1/2}$ = 19.3 s), ^{15}O ($T_{1/2}$ = 122 s), ^{30}P ($T_{1/2}$ = 150 s), ^{38g}K ($T_{1/2}$ = 456 s), and ^{11}C ($T_{1/2}$ = 1223 s). These nuclides all emit a positron, which annihilates and produces indistinguishable 511 keV photons. To separate the PET image of the short-lived nuclides from the long-lived nuclides, the beam was pulsed. Since the half-lives of the short-lived nuclides are so close together and the number of expected counts was low, it was impossible to separate each short-lived contribution based on half-life. An overall beam pulsing structure was thus chosen such that the three short-lived nuclides with a half-life of around 1 s could be separated from the long-lived nuclide with the shortest half-life (^{10}C). A pulsing structure of 6 s beam off followed by 3 s beam on was adopted with a total irradiation time of 5 minutes, leading to 8×10^{10} protons delivered.

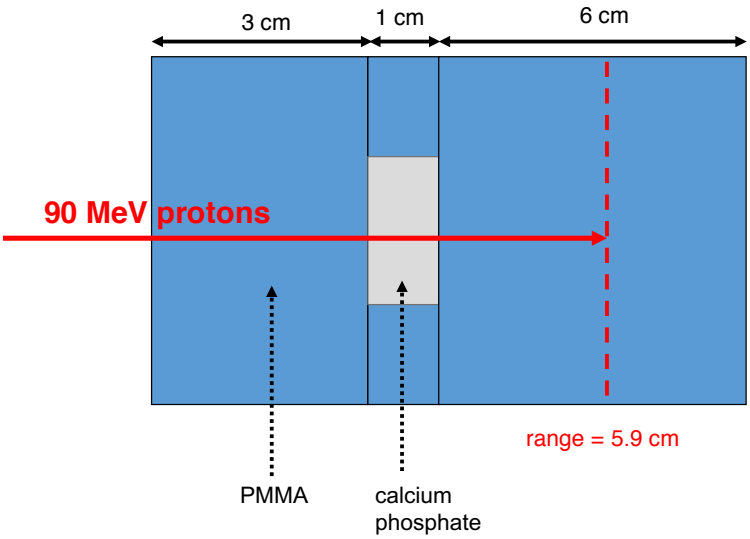

Figure 4.1: The phantom designed to mimic an irradiation of bone embedded in soft tissue. Soft tissue is simulated by PMMA slabs displayed in blue. In the middle PMMA slab, a piece of compacted calcium phosphate powder (displayed in grey) is placed as a substitute for bone. The range of the 90 MeV proton beam is indicated by the dashed red line

The short-lived nuclides were identified using a histogram of the time t_{pulse} (equation 3.2). By calculating t_{pulse}, the relevant time variable is the time relative to the beam pulsing time sequence, thus creating a combined histogram that sums over all beam pulses. During each beam-on part of a pulse, long-lived and short-lived positron-emitting nuclei are produced and the resulting PET count rate grows on top of a prompt background. When the beam is turned off, the prompt background stops and the PET detectors only detect the radioactive decay of the positron-emitting nuclei. At the time scale of the beam pulsing, the longer-lived nuclides can be approximated by a constant background under a combined decay spectrum with contributions of all short-lived components. ^{10}C cannot be considered a constant during the 6 s of decay, but the level of statistical fluctuations in the measured histogram do not allow the addition of an extra component in the fitting procedure. As the production of ^{10}C is only 3.7% of the production of the short-lived nuclides (Dendooven et al., 2019), it was not included separately in the analysis.

The coincidences corresponding to the proton bunches were cut out of the data using the anti-coincidence filter described in section 3.3.5.2. The remaining non-prompt PET data was then used to make the time distribution

of PET counts within the pulsing cycle. The total number of detected counts corresponding to the short-lived nuclei was calculated by fitting a histogram of the beam-off part of the time spectrum of the t_{pulse} of the coincidences with a multi-component decay curve. The decay curve used was

$$A(t) = \sum_i A_{0_i} \exp(-\lambda_i t) + C \tag{4.1}$$

with $A(t)$ the measured time-activity profile, t ranging from 0 to 6 s, A_{0_i} the activity of the i^{th} positron emitter at the beginning of the combined beam-off period, λ_i the known decay constant of the i$^{\text{th}}$ positron emitter, and C the constant activity on this timescale due to longer-lived nuclei. The total number N_i of nuclides at the start of the beam-off period of the i^{th} positron emitter is given by

$$N_i = \frac{A_{0i}}{\lambda_i} \tag{4.2}$$

4.3.2 Imaging of short-lived nuclides

The imaging of short-lived nuclides from calcium and phosphorus was done analogous to sections 3.3.5.4 - 3.3.5.5. Two-dimensional image reconstruction was implemented by recording a histogram of the intersection of the LORs with the mid-plane between the two detectors, the plane in which the proton beam is located. A reconstruction grid of 2×2 mm^2 was used. The reconstruction was corrected for the spatial dependence of the coincidence detection efficiency. Since this reconstruction grid size was of the order of half the crystal pitch, the image reconstruction technique would yield an image with rapidly varying intensities as some pixels in the grid would be unlikely to be filled. So a technique was used to smooth the image. The end-points of the LORs were uniformly randomized over the crystal surface, see figure 4.2. As the detector only provides information on the pixel that detected an interaction, the position within the pixel is not known, so randomizing the LOR end-points over the crystal surface does not take away any imaging information. This randomization increases the spread of the intersection of the LORs with the midplane between the detectors, going from a discreet grid to a more continuous distribution, and thereby smoothing the image.

Separation of short- and long-lived nuclides was based on reconstructing the image from a selected window in the time profile of events from the beam-off part of the irradiation cycle. Two windows were defined: a window for the short-lived nuclei from 0-4 s and a window for the long-lived nuclei from 4-6 s. The contribution of ^{38m}K and ^{29}P at the start of the second window is 5.0% and 50% of the activity at the start of the first window, respectively. To obtain an image reflecting contributions of the short lived components, the image of the second window was weighted by the ratio of the widths of both

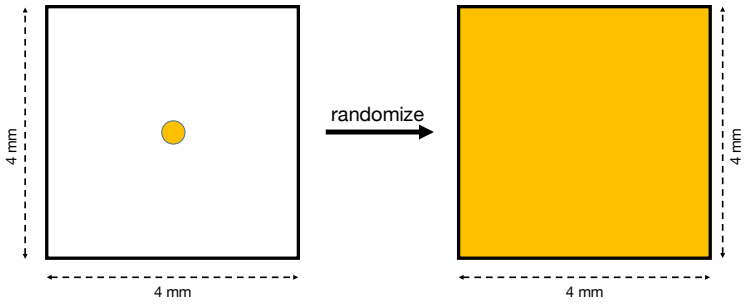

Figure 4.2: Randomization procedure of the LOR endpoints. The dot on the left shows the endpoint of each LOR before the randomization. The endpoint is randomly redistributed across the whole crystal surface.

windows (i.e. a factor of 4/2) and subtracted from the image of the first window. Since at the start of the second image, ^{29}P is still present in a sizeable fraction, the resulting image was more weighted towards the shorter-lived nuclei, being mainly ^{38m}K.

4.3.3 Detection of shifts

Measurements were done for three positions of the target, the nominal position and two positions shifted by 5 and 10 mm respectively with respect to the nominal one. Shifts in the position of the calcium phosphate target were measured by a difference in the centroid of the 1D projection. The centroid A_c is defined as

$$A_c = \sum_i y_i x_i \tag{4.3}$$

with x_i the depth position at bin i, and y_i the weight of that position from the 1D projection, normalized by

$$\sum_i y_i = 1 \tag{4.4}$$

When shifting the target, a substantial portion of the activity distribution moved outside the field of view of the scanner. This would have a biasing effect on the centroid position. To avoid this, a window was chosen around the central peak, so that it had an equal size of 40 mm for each beam position. The window was set to 12-52 mm for the target in the central ("0 mm") position. For the 5 mm and 10 mm target position, the window was shifted to 18-58 mm and 22-62 mm respectively.

The effect of the randomization of the LOR endpoints on the centroid measurement was investigated. The mid-plane reconstruction was repeated 4 times for each measurement with a different random seed, yielding slightly varied images. The centroid was calculated for each of these images.

4.4 Results

4.4.1 Detection of short-lived nuclides

The coincidence counts vs. t_{pulse}, measured as explained in section 4.3.1, are shown in figure 4.3. When the beam turned on at t_{pulse} = 6 s, the coincident count-rate decreased due to the data transfer limit. A multi-component fit of the decay of the short-lived nuclei was performed from 0 – 6 s. Since the half-lives of ^{30}S and ^{38m}K are approximately in the order of a second, fitting them separately resulted in large uncertainties, since they are more or less interchangeable in the fitting procedure. From Dendooven et al. (2019), we can conclude that the integrated production cross-section of these three nuclides from the stopping of a 55 MeV proton is highest for ^{38m}K. The four-component exponential fit (equation (4.1)) can thus be reduced to a two-component fit

$$A(t) = A_{0_S} \exp(-\lambda_s t) + A_{0^{29}P} \exp(-\lambda_{^{29}P} t) + C \tag{4.5}$$

with $A(t)$ the activity measured at time t ranging from 0–6 s, A_{0_S} and $A_{0^{29}P}$ the activity of the two short-lived nuclides (^{30}S and ^{38m}K) and ^{29}P at the beginning of the beam-off period, λ_s and $\lambda_{^{29}P}$ the decay constants of the two short-lived nuclides and ^{29}P, and C a constant representing the decays from long-lived components. The total number of the two short-lived nuclides and ^{29}P detected counts with 1 sigma error is $2.8 \pm 0.5 \times 10^4$ and $1.1 \pm 0.3 \times 10^5$ counts respectively.

4.4.2 Imaging of short-lived nuclides

Figure 4.4 shows the 2D images of the detected counts of the short lived nuclides, corrected for sensitivity. The calcium phosphate target was centered in the FOV of the detector. As seen, most of the counts in the right, short-lived, image are distributed around the position of the calcium phosphate target in the center of the FOV. Negative values might occur due to statistical variations in low-count pixels.

One-dimensional projection profiles of the 2D images are shown in figure 4.5 for the 0 mm and 5 mm shifted measurement, and in figure 4.6 for the 0 mm and 10 mm shifted measurement. For all three measurements, the profile along the x-axis (perpendicular to the beam direction) is slightly wider in the short-lived profile. This corresponds to the higher positron end-point

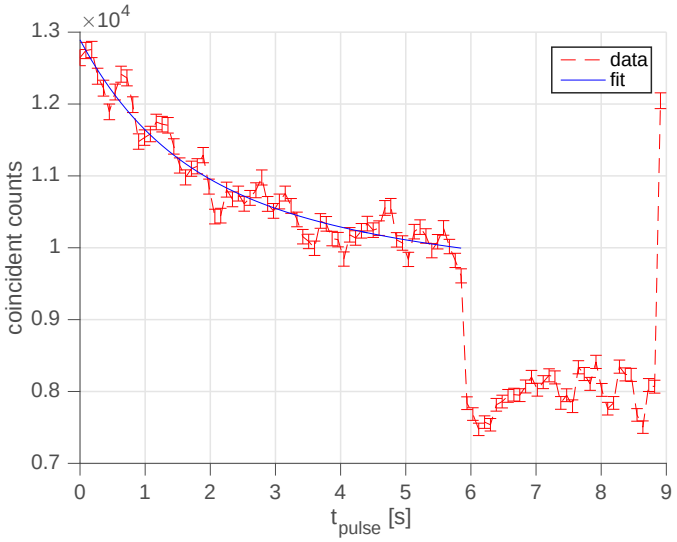

Figure 4.3: Distribution of coincident events as a function of t_{pulse} for the calcium phosphate target displayed in figure 4.1. The beam is off from 0 - 6 s, and on from 6 - 9 s. A fit of the two-component exponential decay during the beam-off period is shown.

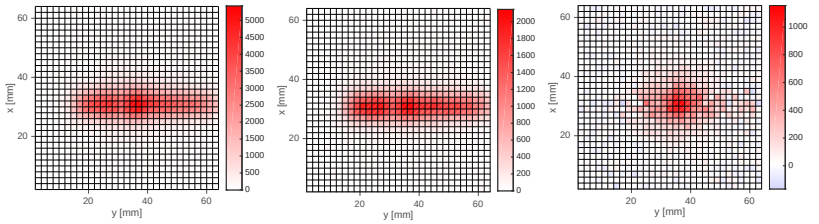

Figure 4.4: 2D images of the coincident counts for the first target position ("0 mm") of the calcium phosphate target. The beam enters from the right in the –y direction. The calcium phosphate is located around y = 33 mm. A PET detection sensitivity correction was applied. (left) The image is made using t_{pulse} from 0 – 4 s, including both short-lived and long-lived nuclei. (middle) The image is made using t_{pulse} from 4 – 6 s, including mostly long-lived nuclei. (right) The short-lived image is obtained by subtracting the weighted long-lived image from the first image.

energy of the short-lived nuclides compared to the long-lived nuclides. ^{15}O has an end-point energy of 1.7 MeV, while ^{38m}K and ^{29}P have a positron end-point energy of 5.0 MeV and 3.9 MeV respectively (NNDC, 2015). The effect, however, is less severe than for ^{12}N (see figure 3.10).

Table 4.2: Measured shifts of the target using the centroid. The centroid value of the 10 mm and 5 mm shifted target are subtracted from the reference position ("0 mm"). Runs correspond to a different initialization of the random seed in the spread of the LOR endpoints across the crystal pixel surface.

run	centroid 10 mm shift $\pm\sigma$ [mm]	centroid 5 mm shift $\pm\sigma$ [mm]
1	8.9 ±1.2	3.9 ±1.4
2	8.8 ±1.2	3.8 ±1.4
3	9.0 ±1.2	3.7 ±1.4
4	8.8 ±1.2	3.6 ±1.4

In the y-direction (parallel to the beam direction), the profiles show a sharp peak at the position of the calcium phosphate insert, in figure 4.5 for the initial target position ("0 mm") at approximately y = 33 mm. Another peak is seen in the final block of the target setup, at approximately y = 25 mm.

4.4.3 Detection of shifts

The shift of the target was measured using the centroid defined in equation (4.3). The results of the measured shift in four runs with different random seeds can be seen in table 4.2. Using four runs, the centroid shift was measured as 8.8 ±1.2 mm to 9.0 ±1.2 mm for the target shifted by 10 mm. A shift of 5 mm was measured as 3.6 ±1.4 mm to 3.9 ±1.4 mm.

4.5 Discussion

4.5.1 Imaging of short-lived nuclides

The one-dimensional projection profile for both the long-lived and short-lived window (top and middle row of figure 4.5 and figure 4.6) show two distinct peaks along the y-axis. These peaks correspond to the last two sections of the target, i.e. the calcium phosphate insert and the final PMMA block. The peaks in the calcium phosphate insert (around y = 33 mm for the initial target position) can be explained by the time-structure of the beam delivery in combination with the imaging time windows. They were chosen to be sensitive to the short-lived nuclei that are produced on calcium and phosphorus. So in the short-lived window of the initial target position (top row of figure 4.5), the peak of the calcium phosphate insert is higher than in the long-lived window. The second peak (around y = 25 mm for the initial target position) is due to activity build-up in the final PMMA slab. This part of the target was not refreshed between each irradiation, since only one slab of that size was available. Long-lived activity (mainly ^{11}C) was built up in this part of the target. For

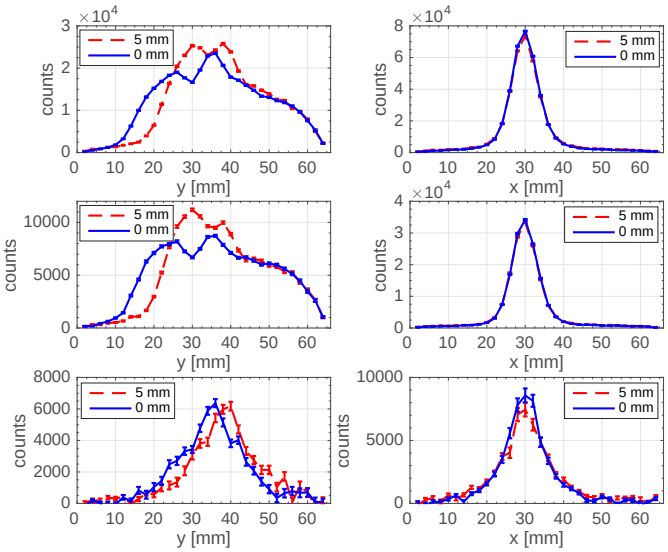

Figure 4.5: 1D projection profiles of the 2D images of figure 4.4 for the first target position (labeled as "0 mm") and for the target shifted by 5 mm. The beam enters from the right in the -y-direction. The x-direction is transversal to the beam. The "5 mm" profiles are normalized to have an equal number of total counts as the "0 mm" profiles. (top) t_{pulse} from 0 – 4 s. (middle): t_{pulse} from 4 – 6 s. (bottom) short-lived profile.

this reason, the peak-to-peak ratio of the calcium phosphate and PMMA slab changes between each irradiation. However, this has little effect on the ability to measure and image the short-lived nuclides present in the calcium phosphate insert. This indicates that the longer-lived activity built up by previous fields is not an essential problem for imaging the short-lived nuclides. Since ^{11}C can be approximated well by a constant activity on this time-scale of 6 seconds, it is subtracted as long-lived activity.

4.5.2 Detection of shifts

From table 4.2 follows that the applied shifts of 5 and 10 mm are measured within the one-sigma margin of error. However, for all runs, the shift is underestimated in the measurement by about 1.2 mm, which might point to a systematic error in the experiment. Since the four runs are not independent measurements but only differ in the LOR randomization procedure, it is not yet possible to draw this conclusion.

During a clinical irradiation, a PET image of the irradiated bony

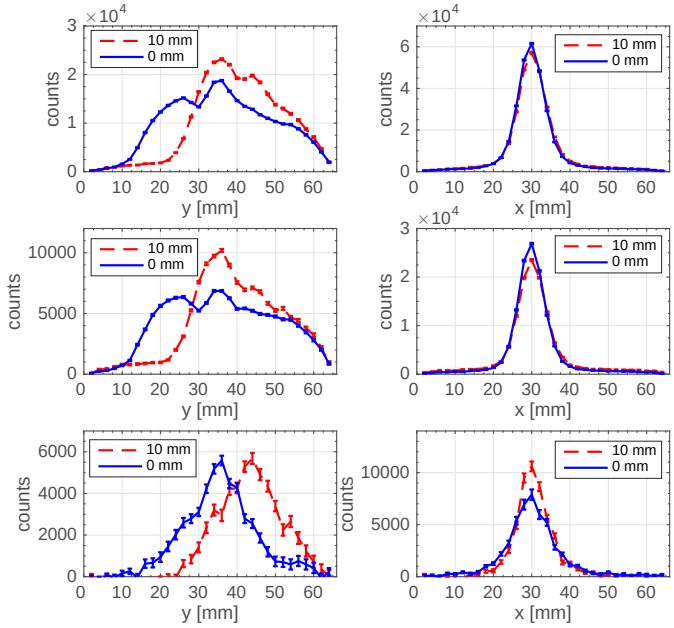

Figure 4.6: 1D projection profiles of the 2D images of figure 4.4 for the first target position (labeled as "0 mm") and for the target shifted by 10 mm. The beam enters from the right in the -y-direction. The x-direction is transversal to the beam. The "5 mm" profiles are normalized to have an equal number of total counts as the "0 mm" profiles. (top) t_{pulse} from 0 – 4 s. (middle): t_{pulse} from 4 – 6 s. (bottom) short-lived profile.

structures can be obtained shortly after an irradiation has started using the short-lived nuclides that are produced on bone. Typically, irradiation of bone is not the primary target of the treatment plan. More often, a proton beam must pass through bone to reach the tumor site. As such, the distal end of the proton beam does not end in bone tissue, making this type of imaging less suitable for range verification of proton beams. However, a fast PET image can be used to highlight the different sections of bone that were irradiated and confirm that the location is as expected, serving as an independent check of the patient positioning and anatomy, at no *additional* radiation dose to the patient.

4.6 Conclusion

An experiment was performed to measure the PET image of short-lived nuclides that are produced on bone tissues, most notably ^{38m}K and ^{29}P with a

half life of 924 ms and 4.14 s respectively. The long-lived background was subtracted from the PET image by introducing a beam-off period of 6 seconds into the cyclotron beam structure. An estimate of the long-lived image was obtained from 4 to 6 seconds after the beam was turned off. This background image was then subtracted from the image containing the short-lived nuclides. Using four runs, a target shift of 10 mm was measured as 8.8 ± 1.2 mm to 9.0 ± 1.2 mm. A target shift of 5 mm was measured as 3.6 ± 1.4 mm to 3.9 ± 1.4 mm. As is the case for the ^{12}N measurements, the signal to background ratio decreases as the irradiation progresses. The best signal to background ratio resulting in the best imaging resolution is obtained for measurements at the start of the irradiation.

Part II

Simulation studies

Chapter 5

Simulation software

5.1 Introduction

Several software packages exist for Monte Carlo modeling of proton therapy, such as GATE (Jan et al., 2004) and TOPAS (Perl, Shin, Schümann, Faddegon, & Paganetti, 2012). However, at the time this research project was started, their track record was not yet as established as it is today. In order to be flexible regarding implementation of the simulation details and to get a lightweight simulation for a high level of statistical precision, a software package has been developed in-house for Monte Carlo simulations of patient irradiation. The major components of the software are described in this chapter. Chapter 6 utilizes this software for a qualitative study of the differences between PET and prompt gamma ray imaging for a representative patient case. This study was executed in an early phase of the research project. Some aspects of the software have been modified and adapted after this study. The most recent results using three additional patients are presented in chapter 7. Differences of the simulation software between the two studies are indicated in the relevant chapters.

The software package for *in vivo* dose delivery verification is based on a custom application for proton dose delivery, using the Geant 4.10.3 toolkit (Agostinelli et al., 2003). In order to obtain clinically relevant results, all simulations are based on real patient cases. These patients were part of a study at the University Medical Center Groningen (UMCG) into the clinical benefit of proton therapy. They were treated with conventional photon radiotherapy, but a treatment plan was also made for proton irradiation. The Monte Carlo software package is designed to be able to generate dose distributions as well

as the spatial distributions of positron and prompt gamma ray emitting nuclei using a treatment plan from a treatment planning system (TPS), to introduce deviations such as range and positioning errors in the dose delivery simulation and to investigate the effect of these errors on the positron emitting nuclide and prompt gamma distributions. A schematic representation of the workflow is depicted in figure 5.1. In a further step, the positron emitting nuclide distributions were used to perform simulations of PET scans of the irradiation, but this is outside of the scope of this thesis.

5.2 Proton therapy simulation

The treatment plans were simulated using a Geant 4.10.3 application, which was developed at KVI-CART. This simulation software takes as input the treatment plan converted to a Geant4 macro, the planning CT data, a conversion table from CT data to Geant4 materials and the timing information of the beam delivery. The software then simulates proton transport and generates a 3D delivered dose map, positron emitting nuclide distributions representing the amount of nuclides present at the end of the irradiation taking into account the specific time structure of the beam delivery and radioactive decay, as well as the cumulative prompt gamma emission distributions representing the total signal that could be captured by a prompt gamma ray imaging device.

5.2.1 Conversion of planning CT to tissue composition

The treatment planning CTs were rebinned on a $1 \times 1 \times 1$ mm^3 voxel grid, and used as a phantom for the proton transport calculations in Geant4. To be able to simulate proton dose delivery in Geant4, the patient CT data which are expressed in Hounsfield Units (HU) have to be converted to Geant4 materials with a specific density and elemental composition. This is not straightforward, since there is no one-to-one correspondence between HU and stopping power of tissues. Different tissues can have the same HU value in the CT, and materials with identical stopping powers for protons can correspond to different HUs in the CT (Paganetti, 2012). The most common method to correlate HU to human tissue is based on measurements done by Schneider, Bortfeld, and Schlegel (2000). Schneider et al. measured different materials in a CT scanner and from this data constructed a conversion table between HU and elemental composition and density of tissue samples. Our method builds on this work by interpolating between these elemental composition values to obtain smooth transitions between materials (see figure 5.2). Because of the poor soft-tissue contrast of CT images, the method of Schneider et al. cannot accurately distinguish between e.g. white and grey brain tissue, as experimentally observed by Parodi, Paganetti, et al. (2007). This shortcoming however is of little importance for the results obtained in the present more theoretical study. A total of

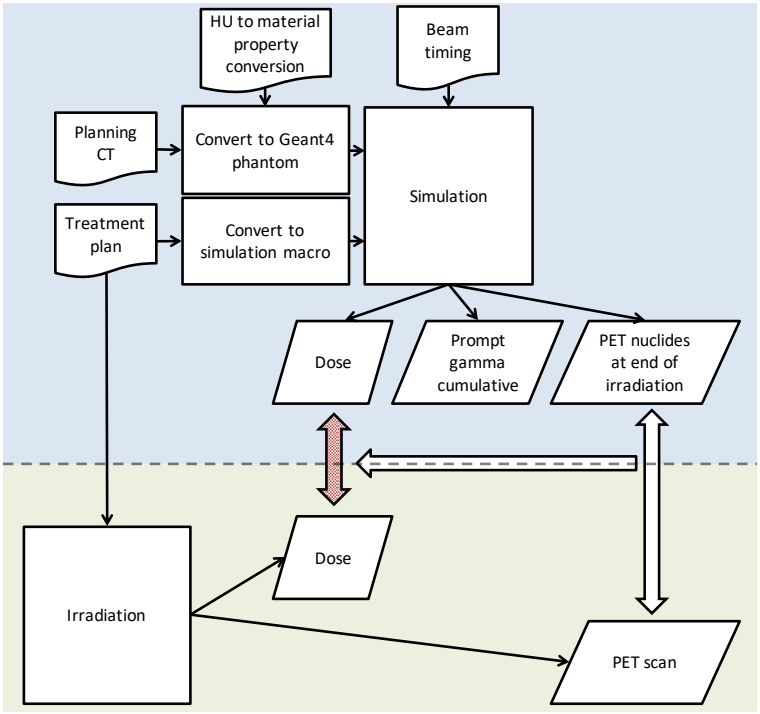

Figure 5.1: Schematic representation of the simulation software package (blue background) and how it could be incorporated to validate the delivered dose to the patient from an actual irradiation (green background). The goal of *in vivo* dose delivery verification would be to compare the delivered dose maps (red arrow), however, this cannot be measured directly. Instead, the measured PET image can be compared to the predicted PET image (vertical white arrow), which gives information on the difference in dose delivery. A similar scheme could be made for prompt gamma ray imaging by replacing the PET scan with the prompt gamma image and comparing to the predicted prompt gamma image. Ideally, the comparison of the measured PET image with the predicted distribution of PET nuclides gives information on the delivered dose in relation to the predicted dose (indicated by the white horizontal arrow)

537 different tissue materials were defined. The elemental composition of these materials was taken from the interpolated data extracted from Schneider et al.. The mass density of the materials was calculated using the elemental composition and the electron density calibration curve of the scanner that was used for the planning CT at UMCG. The calibration is performed using a set of calibration materials with known composition and electron density in a Gammex phantom. The electron density calibration data are displayed in figure 5.3.

To calculate the absolute electron density from the relative electron

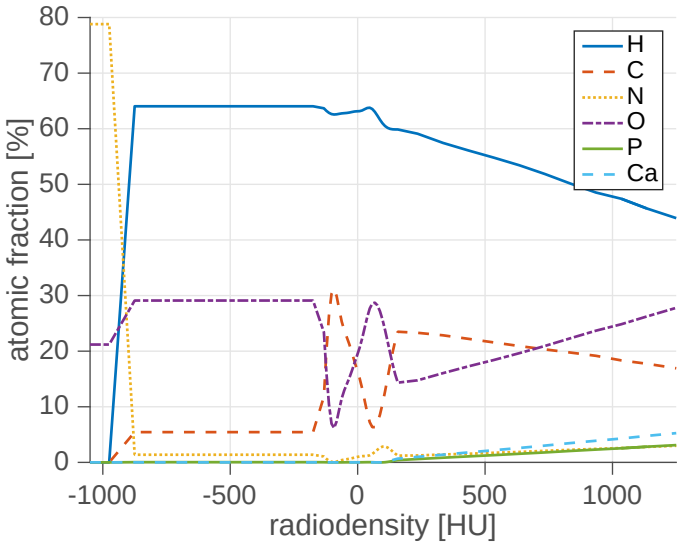

Figure 5.2: Elemental composition of tissue as a function of radiodensity (HU). These values are the percentage of atoms of the given type relative to the total number of atoms. This must not be confused with mass fractions.

density to water, the following formula was used

$$\rho_e = \frac{\rho_{e_{rel}} \cdot n_{e_{water}} \cdot N_A \cdot \rho_{water}}{m_{water}} \tag{5.1}$$

where ρ_e is the absolute electron density, $\rho_{e_{rel}}$ is the electron density relative to water, $n_{e_{water}}$ is the number of electrons in a water molecule (10), N_A is Avogadro's constant, ρ_{water} is the mass density of water and m_{water} is the mass of a water molecule (18.015 28 g mol^{-1}).

From the elemental composition of the material, the number of electrons per voxel n_e was calculated with

$$n_e = \sum_i z_i \epsilon_i \tag{5.2}$$

where i loops over all elements present in the tissue, z_i is the charge number of that atom, and ϵ_i is the relative abundance of that element in the tissue. This average number of electrons was calculated from the tissue compositions used in Schneider et al. (2000). From the CT measured electron density and the electron density in the tissue composition data, we could calculate the molecular

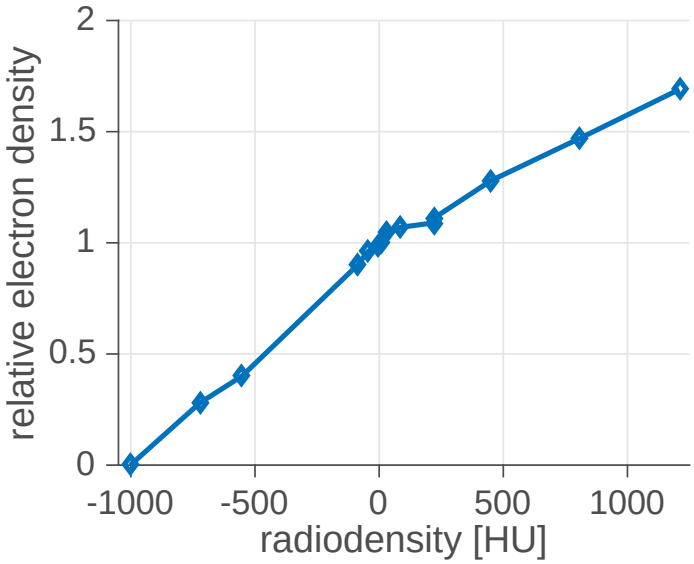

Figure 5.3: Relative electron density (relative to water) calibration data taken with the CT scanner that was used to take the planning CTs. Data retrieved from UMCG, Department of Radiotherapy, private communication.

density ρ_{mol} using

$$\rho_{mol} = \frac{\rho_e}{n_e} \tag{5.3}$$

The mass density of the material was then calculated by multiplying the molecular density with the molecular mass

$$\rho = \rho_{mol} \cdot \sum_i m_a^i \epsilon_i \tag{5.4}$$

where m_a^i is the atomic mass of the element. Using this method, the density of the material in the planning CT was calculated using the elemental composition from Schneider et al. and the electron density from the CT calibration data. The resulting density as a function of radiodensity is displayed in figure 5.4. The tissue composition used in this calculation is displayed in figure 5.2.

5.2.2 Fluence-based approach to calculate PET and prompt gamma ray distributions

Geant4 offers built-in physics models of nuclear reactions to keep track of the production of radioactive nuclei and prompt gamma rays. It does this by adding

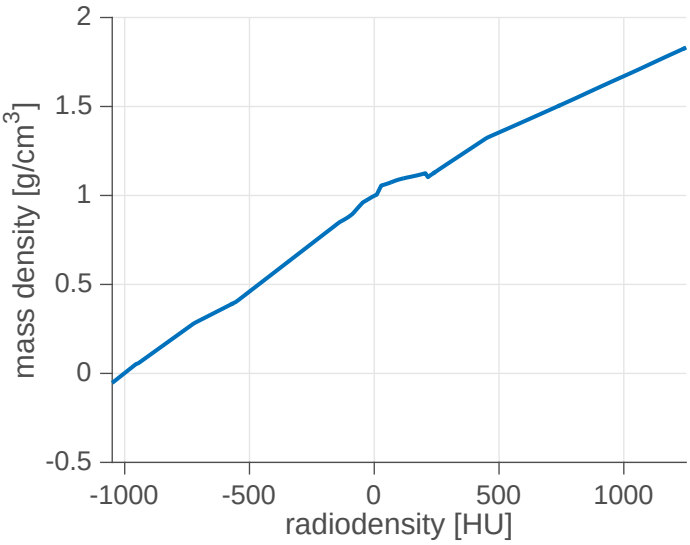

Figure 5.4: The mass density calculated using elemental composition information from Schneider et al. (2000) and the electron density calibration data of the scanner that was used to make the planning CTs. Mass densities smaller than 0 are due to extrapolation, and are replaced with the smallest non-negative value (7.8×10^{-3} g/cm^3) used in the simulations.

a process that simulates inelastic collisions of the proton beam with the tissue nuclei. There are two downsides to this method. The first is that it will lead to poor statistics for a practical number of simulated primary particles. The production cross sections of positron emitting nuclei and prompt gamma rays are of the order of 10 to 100 mbarn (see figure 5.5). This means that the likelihood of the interaction is relatively small, and a lot of primary particles are needed to provide sufficient statistics. The second problem is that the cross sections following from the Geant4 physics models are known to differ substantially from experimental cross sections (Böhlen et al., 2010), which, when used, will lead to a distribution that has a poor correlation with experimental measurements. To remedy these problems, a fluence-based approach was implemented which can be combined with experimental production cross sections to obtain production distributions. This approach is similar to the approach used for the FLUKA simulations performed by Parodi, Ferrari, Sommerer, and Paganetti (2007). Those simulations by Parodi et al. did not include the time structure of the irradiation, nor the decay of the positron emitting nuclides during the irradiation. These effects are taken into account in this software package.

In order to be able to accurately simulate the PET and prompt

gamma ray production, a Geant4 fluence scorer was developed. This scorer keeps track of a 4D fluence matrix with dimensions x,y,z and E, which tracks the path length of protons through a voxel at a specific kinetic energy. After each 100 ms of the irradiation time, the fluence scorer calculates positron emitting nuclide productions and the production of prompt gamma rays from these protons. The decay of the PET nuclides during this time is taken into account. Fractional (non-integer) production of nuclides is calculated using the integrated path length for each voxel and the relevant cross section. This acts as a variance reduction technique. The program incorporates experimental cross sections of 10 different reaction channels which are relevant for PET production in biological tissues. The channels leading to a positron emitting nuclide whose cross sections are incorporated into the software package, are:

- ^{16}O(p,pn)^{15}O
- ^{16}O(p,p2n)^{14}O
- ^{12}C(p,pn)^{11}C
- ^{14}N(p,2p2n/α)^{11}C
- ^{16}O(p,pαn)^{11}C
- ^{12}C(p,p2n)^{10}C
- ^{14}N(p,pn)^{13}N
- ^{16}O(p,2p2n/α)^{13}N
- ^{31}P(p,pn)^{30}P
- ^{40}Ca(p,2pn)^{38}K.

These cross sections were piece-wise linearly interpolated to best match with the experimental data from the EXFOR database (Otuka et al., 2014).

Concerning the prompt gamma rays, the most dominant gamma-ray transitions were included, with energies E_γ = 6.13 MeV and 4.44 MeV. This choice is based on the fact that these prompt gamma rays have a more favorable relationship with the Bragg peak compared to the ensemble of all prompt gamma rays, as experimentally demonstrated e.g. by Verburg and Seco (2014). It is thus assumed that the prompt gamma imaging system used to image the signal has an energy resolution such that the 6.13 MeV and 4.44 MeV gamma rays are distinguishable from other radiation, as is e.g. the case for the detector used by Verburg and Seco. The 6.13 MeV gamma rays are created on ^{16}O via the ^{16}O(p,p'γ)^{16}O reaction. For the 4.44 MeV gamma rays, we included both the 4.438 MeV transition in ^{12}C resulting from the ^{12}C(p,p'γ)^{12}C and ^{16}O(p,p'$\alpha\gamma$)^{12}C reactions and the 4.444 MeV transition in ^{11}B resulting from the ^{12}C(p,2pγ)^{11}B reaction as no conceivable imaging system can separate these two transitions. The prompt gamma ray production cross sections were taken from Kozlovsky et al. (2002).

The reaction cross sections vs. proton energy are shown in figure 5.5. The most important produced nuclides are ^{15}O and ^{11}C. Both of these are produced with a high probability in soft tissue and have a good correlation with delivered dose. ^{30}P and ^{38g}K are mostly produced in bone structures and as such

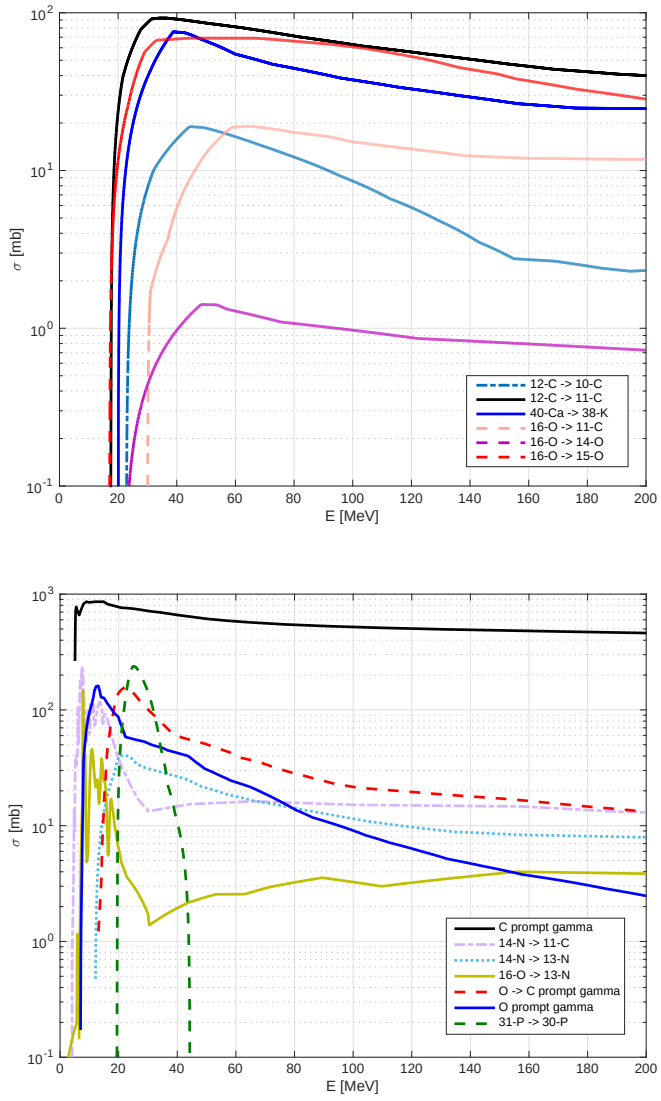

Figure 5.5: Overview of the production cross sections included in the simulation software. The vertical axis displays the cross section in millibarn and the horizontal axis displays the proton energy in MeV. The prompt gamma ray cross sections are labeled as follows: 'O prompt gamma' indicates the 6.13 MeV prompt gamma ray from the ^{16}O(p,p'γ)^{16}O reaction, 'O -> C prompt gamma' indicates the ^{16}O(p,p'$\alpha\gamma$)^{12}C reaction resulting in a 4.44 MeV prompt gamma, and 'C prompt gamma' includes both 4.44 MeV lines from ^{12}C(p,p'γ)^{12}C and ^{12}C(p,2pγ)^{11}B.

do not play an important role in distal edge detection and correlate poorly with the edge of the dose distribution.

To calculate the production of the PET nuclides and prompt gamma ray emissions, the program loops through all elements in the fluence matrix. For each voxel, it calculates the material composition by using the Geant4 defined materials to obtain the relevant mass fractions and density of that material. From this data, we calculate the atomic density in each voxel

$$n = \frac{\rho \cdot w}{m} \tag{5.5}$$

where n is the number density of the nuclei, w is the mass fraction of the nuclei, m is the atomic mass and ρ is the mass density. Next, the experimental cross sections are used to calculate N, the density of nuclei produced in a voxel

$$N(x, y, z) = \sum_{E=0}^{E_{max}} n \cdot F(x, y, z, E) \cdot \sigma(E) \tag{5.6}$$

where F is the fluence and $\sigma(E)$ is the production cross section. This leads to fractional (non-integer) production of nuclei, which acts as a variance reduction technique.

An unevenly spaced energy binning was implemented for the fluence matrix to provide a higher resolution at lower proton energies, where the cross section changes more rapidly (see figure 5.5). From 0 to 3 MeV the fluence was not tracked, since this is below the energy threshold of all cross sections. From 3 to 60 MeV, a fine bin width of 1.5 MeV was chosen. From 60 to 216 MeV, the fluence was sampled using 13 MeV bins, since the cross section changes only gradually in this energy range. No proton energies above 216 MeV were used during the treatment simulations.

5.3 Physics list

The physics list was chosen and implemented using the Geant4 reference physics list for hadrontherapy and medical applications. The following physics list items were included in the simulations:

- EmStandardPhysics_option4
- HadronPhysicsQGSP_BIC_HP
- EmExtraPhysics
- HadronElasticPhysics
- StoppingPhysics
- IonBinaryCascadePhysics
- NeutronTrackingCut
- HadronElasticPhysicsHP

- DecayPhysics
- RadioactiveDecayPhysics

A secondary particle tracking cut of 10 μm was implemented and a maximum step size of 0.1 mm was set. Validation measurements of some of these models were performed by Grevillot et al. (2010). The reference physics list of the TOPAS (Perl et al., 2012) software package overlaps with this physics list, as it contains: EmStandardPhysics_option4, HadronPhysicsQGSP_BIC_HP, DecayPhysics, IonBinaryCascadePhysics, HadronElasticPhysicsHP and StoppingPhysics.

5.4 Biological washout

To obtain the best relationship of the PET image with the dose distribution, it is important that positron emitters created by the therapy do not move from their point of origin before they decay. Due to metabolic processes inside the patient however, positron-emitting nuclei are transported away from where they were created. The PET image will then be blurred and will have an overall lower level of counts if nuclei are transported outside the field of view of the scanner. This phenomenon is called biological washout of the PET nuclei and causes a degradation of the image quality.

5.4.1 Formalism

In the literature, several methods have been used to investigate the effect of biological washout of positron emitters created by hadron therapy. Each group uses a slightly different method to determine the washout parameters. The so-called three component model introduced by Mizuno et al. (2003) is often used to describe the effect of biological washout on the total count rate of the PET scanner. The effective count rate for a certain region of interest in a living subject including biological processes can be described as

$$A_{eff}(t) = A_{phys}(t) \cdot C_{bio}(t)$$

where A_{phys} is the physical count rate that one would get purely from the radioactive decay of all the PET nuclides, but modified by a biological factor C_{bio}

$$C_{bio} = M_f \exp(-\lambda_f t) + M_m \exp(-\lambda_m t) + M_s \exp(-\lambda_s t) + B$$

where M_f, M_m and M_s are the fractions of the fast, medium and slow washout components, corresponding to their respective decay constants λ_f, λ_m and λ_s. The model was slightly adapted by Helmbrecht et al. (2013) to include a factor B, which signifies the fraction of positron emitters that do not undergo biological processes, or at least not in the timescale under investigation. The factor

B needs to be included to account for longer lived nuclides or radiation background. Not including such a factor skews the half-life to larger values. The fractions M and B should be constrained by

$$M_f + M_m + M_s + B = 1$$

to keep the effective activity at $t = 0$ equal to the physical activity since there has not been any biological washout at $t = 0$.

$$A_{eff}(0) = A_{phys}(0)$$

There is no quantitative data on the blurring of the PET image due to diffusion of nuclei or metabolic transport inside the field of view of the scanner. Mizuno et al. (2003) report a broadening of the widths of profiles, but no conclusions can be drawn from this one observation.

5.4.2 Experimental data

To obtain the values M, B, and λ, experiments have been done on rabbits and rats by Mizuno et al. (2003), Tomitani et al. (2003), Hirano et al. (2013), Ammar et al. (2014), Ten Haken, Nussbaum, Emami, and Hughes (1981), Grogg et al. (2015) and Toramatsu et al. (2018). There is only one paper with patient-data, i.e. from Helmbrecht et al. (2013). The animal experiments all roughly followed comparable protocols. First the animal was anesthetized and positioned for irradiation to either the brain or a muscle. After irradiation, the animal was scanned as soon as possible with a PET scanner in list-mode acquisition. After scanning long enough and waiting until all the produced activity had decayed, the animal was killed. It was then placed in the same position, and irradiated and scanned in the same way. The difference in time-activity profiles between the dead and the live condition is then attributed to the biological processes which are not present any more in the dead animal. Fitting the curves with the model, values for M, B and λ are obtained.

The fitted washout parameters are summarized in table 5.1. Considering the fact that biological washout parameters are dependent on beam ion, target tissue composition, chemical reactions of the PET nuclide, and metabolic processes that are dependent on tissue type and patient specific parameters, it is not trivial to interpret the data in table 5.1. From this data we can make several recommendations. First of all, a fast washout component in the order of a couple of seconds was only seen by Mizuno et al. (2003) and Toramatsu et al. (2018). Helmbrecht et al. (2013) were also specifically looking for this component using irradiation of 14 patients, however no contribution was found in the data. For all patient cases the fitted M_f parameter was close to zero, indicating no fast washout contribution. In the discussion of this result they pose the hypothesis that fast washout components most likely come from

radioactive carbon nuclides that are created in a blood vessel and are quickly washed away. Since blood flow in the tumors under investigation might be low, the fast component might not be visible in their data. If there is a short washout component in the order of 2 s with a fraction of roughly a third of all counts, this will have a major impact on PET imaging. Since there is no other data that corroborates these two measurements, we consider the component not to be present in general.

The medium component in the order of 20 to 300 s was seen in most of the experiments, except by Ammar et al. (2014) for protons. This is due to the fact that Ammar et al. decided to fit the proton irradiation with a one-component model. Data from this experiment however shows that there is a difference in biological washout between protons and carbon irradiation. Since almost all of the biological washout experiments were done with carbon beams, and Ammar et al. conclude that biological washout for protons might be faster than for carbons, it is necessary to bias the washout parameters for protons to a fast washout with a high fraction. This is the worst case scenario for PET imaging, and by using this worst case scenario, results can only improve if washout turns out to be slower.

In table 5.1, an experiment using high energy photons to determine the ^{15}O decay and medium washout component is included (Ten Haken et al., 1981). This washout value should also be applicable to proton irradiation, as during the first minutes after the start of a proton irradiation mainly ^{15}O is seen, which is not produced in large quantities during e.g. a carbon ion irradiation. This might also be in line with what Ammar et al. conclude, since target fragmentation is the production method of positron emitters for both high energy photons and protons.

Table 5.1: Measured half lives and fractions for the biological washout models from different publications.

paper	$T_{1/2,fast}[s]$	M_{fast}	$T_{1/2,medium}[s]$	M_{medium}	$T_{1/2,slow}[s]$	M_{slow}
Mizuno 2003 rabbit brain	2.0 ± 1.8	0.35 ± 0.03	$1.4 \pm 0.2 \times 10^2$	0.30 ± 0.03	$1.0 \pm 0.2 \times 10^4$	0.35 ± 0.01
Mizuno 2003 rabbit thigh	$1.0 \pm 0.8 \times 10^1$	0.30 ± 0.04	$2.0 \pm 0.5 \times 10^2$	0.19 ± 0.03	$3.2 \pm 0.4 \times 10^3$	0.52 ± 0.02
Tomitani 2003 rabbit thigh			$2.5 \pm 0.7 \times 10^2$	not given	$5.5 \pm 0.5 \times 10^3$	not given
Hirano 2013 rat brain			$1.2 \pm 0.4 \times 10^2$	not given	$8.3 \pm 2 \times 10^3$	not given
Helmbrecht 2013 human brain	not seen	not seen	156 ± 5	0.438		
Ammar 2014 mouse brain ^{12}C			249.0	0.19	3527	0.35
Ammar 2014 mouse brain proton			not seen	not seen	2094	0.75
Ten Haken 1981 rat scalp photon			$1.9 \pm 0.3 \times 10^2$	not measured		
Grogg 2015 rabbit head proton			69.31			
Grogg 2015 rabbit bone proton			108.3			
Toramatsu 2018 rabbit brain ^{10}C + ^{11}C	2 ± 1	0.2 ± 0.05	$1.4 \pm 1 \times 10^2$	0.32 ± 0.03	$1.0 \pm 0.3 \times 10^4$	0.48 ± 0.04
Toramatsu 2018 rabbit brain ^{15}O	not seen	not seen	$5.8 \pm 0.1 \times 10^1$	0.62 ± 0.01	$1.7 \pm 0.2 \times 10^3$	0.38 ± 0.02

A slow component with a half-life in the order of 300 to 10 000 s was also seen in most experiments that were designed to look for this component. The range of this value is from 2094 to 10 191 s with a fraction of 0.75 to 0.35 respectively. The 2094 s value comes from the proton irradiation by Ammar et al.. Since the data was only fitted with a one-component model, and given the fact that a process with a shorter biological half-life might be present, it is unsurprising that this value is biased to a shorter half-life and a higher fraction. The spread in half-life and fraction is quite large. However, for in-situ and in-room scanning of approximately 2 minutes during or directly after the irradiation, the slow component half-life is not very important and can be approximated by a constant non-decaying fraction.

5.4.3 Incorporation in simulation software package

When simulating in-room and in-situ PET after a proton irradiation, biological washout of the PET nuclei needs to be taken into account. Proton therapy centers that will use the washout parameters to compare measured and simulated PET scans, will probably tune the parameters to obtain the best possible match between the two. For our use-case, i.e. a pure simulation study of PET, it is less important to obtain conformity to an experiment. The goal was to investigate PET in a realistic way that might be used in the clinic.

In this case, it is better to stay on the pessimistic side and use conservative values for the washout parameters, which means short half-lives and a relatively large fraction. Given that the fast component is most likely not present, and the slow component can be approximated by a fraction without washout, only the medium component is of interest. Grogg et al. (2015) reported the lowest value for the biological half-life, i.e. 69.31 s. The highest reported fraction is 0.438 by Helmbrecht et al. (2013). This resulted in a one-component model with $T_{1/2} = 69.31$ s, $M = 0.438$, and $B = 0.562$ for all tissues and for all nuclei, which was implemented in the simulation software.

Chapter 6

Comparison of PET and Prompt Gamma Imaging – a representative case

6.1 Introduction

This study evaluates the applicability of PET and prompt gamma imaging for *in vivo* dose delivery verification in a strongly heterogeneous region. It has been known for a long time and experimentally verified by Urie, Goitein, Holley, and Chen (1986) that a Bragg peak loses its characteristic shape on the distal side of a complex heterogeneity. Similar effects will occur in the secondary radiation distribution. Therefore, the optimization of imaging techniques for *in vivo* dose delivery verification cannot be done based on irradiation of simple phantoms. The dose distributions used for studying dose delivery verification should be clinically representative, and thus not too simple. A lack of clinically realistic structure in the distribution of dose and in the production of secondary radiation limits the clinical relevance of the results. By using a realistic head-and-neck patient case, we investigated a rather complex situation due to the heterogeneity in composition and density of the irradiated tissues. The patient was used as an extremely heterogeneous phantom to investigate the PET and prompt gamma imaging techniques. This patient category was chosen, as it is one of the major indications for which proton beam radiotherapy is considered beneficial for the patient.

To our knowledge, the only direct comparison of positron annihila-

tion photons and prompt gamma rays in real patient cases to date is the study by Moteabbed, España, and Paganetti (2011). Moteabbed et al. compared prompt gamma ray production and positron emitter production for range verification in proton therapy by means of Monte Carlo patient studies for 4 clinical cases in different anatomical regions, focusing on differences between a passive scattering Spread Out Bragg Peak (SOBP) delivery and a pencil beam irradiation. The correlation of the prompt gamma and positron emitting nuclei distributions with the dose distribution was quantified by means of 2D maps of the difference in distal falloff positions; consistency of this difference over the irradiated area was considered to be an important factor. This led to the conclusion that the verification potential of prompt gamma ray imaging and positron emission tomography depends on the dose delivery technique (scattering or scanning) and on anatomical characteristics of the distal edge region, such as the heterogeneity.

We consider the primary purpose of *in vivo* dose delivery verification to be the ability to detect discrepancies in delivered dose distribution versus planned dose. Density changes are a major risk factor causing such discrepancies. To compare the applicability of PET and prompt gamma ray imaging, we introduced density changes to the patient. These density changes serve as a proxy for anatomical changes, which will have an effect on the distal edge of the dose distribution. While the introduced density change might not be realistic in itself, the effect on the distal edge of the dose distribution is clinically relevant. We studied the sensitivity of both techniques to detect the change in the dose delivery by investigating differences in the PET and prompt gamma ray distributions caused by these density modifications. The detection of these differences will be more difficult in tissue where density and elemental composition vary sharply as a function of location. In order to obtain results that are comparable to clinical working conditions, we selected a typical head-and-neck case that is strongly heterogeneous.

6.2 Materials and Methods

6.2.1 Treatment simulation and secondary radiation calculation

The treatment simulation was executed using the software package described in chapter 5. In order for the simulated dose to equal the treatment dose of one fraction (the field simulated has a planning target volume dose contribution of 0.46 Gy per fraction), the simulation output was scaled with a factor of 714, since only 1 in 714 protons was simulated. In the simulation of the treatment, the proton fluence was recorded in $1 \times 1 \times 1$ mm^3 voxels as a function of energy in 4 MeV bins. This constant bin-width is different than what is described in the previous chapter, as the simulation was performed with an earlier version of the software. The fluence was then combined with experimental cross sections

for the PET isotopes and the prompt gamma rays to calculate distributions of both types of secondary radiation.

The production of the following PET nuclides was calculated: ^{15}O, ^{11}C, ^{10}C, ^{14}O, ^{30}P, ^{38g}K, and ^{13}N, produced on the elements C, N, O, P and Ca. In this chapter, we only show results for the dominant positron emitting nuclides: ^{15}O and ^{11}C. These nuclides are shown separately, even though they emit identical 511 keV photons, in order to investigate the effect of each nuclide on the total PET image. The time sequence of the spot scanning irradiation and the decay of the PET nuclides during the irradiation were included in the simulation. Biological washout of the PET nuclides was not included in the simulations. The washout model described in section 5.4 was not yet finalized when the simulations were executed, and fewer experiments were performed at that time. Omitting the biological washout has the effect of an overall higher number of nuclei available for PET imaging. Also the distribution of PET nuclides has a higher contribution from spots that were irradiated early in the irradiation, since the simple washout model acts as an additional non-selective half life for the PET activity. Biological washout does not have an effect on the prompt gamma ray distributions.

We used a distal-edge-last irradiation time structure as this optimizes PET imaging of the distal edge, which is most relevant for *in vivo* dose delivery verification. We have analyzed the PET nuclide distributions at the end of the irradiation. This represents the situation of a cyclotron-based facility, most commonly used for proton therapy, with PET imaging starting directly after the irradiation (possibly after one field). We thus assumed that PET data could not be obtained while the beam is on due to a too high radiation flux. This is however not a principle impossibility; high-count rate detectors with suitable electronics and data acquisition can allow PET imaging while the beam is entering the patient (see e.g. Buitenhuis, Diblen, Brzezinski, Brandenburg, and Dendooven (2017); Cambraia Lopes et al. (2016); Crespo et al. (2005); Sportelli et al. (2014)). In the case of a synchrotron-based facility, PET imaging is possible in-between beam spills, allowing in general a larger number of counts to be obtained (Enghardt et al., 2004).

The 1 mm resolution in the simulations was (deliberately) a few times better than the image resolution one can hope to achieve in practice. Therefore, in order to represent a measured image more closely, a realistic spatial resolution that models the imaging resolution was introduced by applying 3-dimensional Gaussian blurring with a FWHM of 4 mm. This is a realistic imaging resolution for PET, but has not yet been achieved for prompt gamma ray imaging. The blurring was applied before the analysis discussed in section 6.2.3 is performed.

6.2.2 Clinical treatment details

In this study, the patient was a head-and-neck case that could potentially benefit from proton therapy by sparing the salivary glands and thereby reducing the risk and/or severity of xerostomia (dry mouth syndrome). The treatment was planned using the Elekta XiO Proton (Elekta AB, Stockholm, Sweden) treatment planning system. The irradiation used a spot scanning beam delivery with three coplanar fields of which one was selected for our simulation. In the selected field, the proton beam entered the patient through the back of the neck at a gantry angle of 180° and a couch angle of 0°. The total irradiation time of this field was 132 s with a switching time of 5 ms between spots and 50 ms between different energy planes. A grid of 37 × 31 × 33 spots was used, of which 7227 spots were filled. The field irradiated a region from the nose down to the upper lung. In this chapter, we present sagittal slices from the region surrounding the mouth.

6.2.3 Sensitivity to compromised dose delivery

The sensitivity of both secondary radiation sources to reflect changes in the delivered dose distribution was studied by introducing artificial inserts into the patient anatomy at the level of the treatment planning CT. Although the inserts themselves are unrealistic anatomical changes, they induce changes in the proton transport that are representative of those encountered in clinical practice. Spherical inserts of air and dense water (water with a density of 1.5 g/cm^3) with diameters of 5 mm and 10 mm were used. The maximum proton energy after the insert was calculated to be 140 MeV. The effect of the inserts on the secondary radiation production was quantified by two methods, as described below.

Firstly, we considered the (absolute) difference between the distributions for the unmodified patients and the patients modified by the introduction of an insert. This method accounts for the need of the secondary radiation to be both sensitive to changes and to produce a strong signal. When a relative difference would be used, a small difference with respect to a small value would be considered just as important as a large difference with respect to a large value. As this is unwanted behavior, the absolute difference between the distribution was used. Secondly, a 2D distal edge map was constructed. The spherical inserts have an effect on the distal edge of the proton field: an air insert extends the proton range whereas a dense water insert shortens it. A similar effect is produced on the distal edge of the secondary radiation distributions. The position of this distal edge was determined for all line profiles in the beam direction (the Y-direction in our case), resulting in a 2D map of the distal edge. This process is illustrated in figure 6.1. Most commonly, the distal edge position of a distribution has been quantified as the position for which

a certain fraction (usually between 20 % and 50 %) of some maximum (most common the overall maximum or the maximum closest to the distal edge) of the line profile is crossed, with these parameters adjusted to achieve the best results. The end-point of the radiation distribution is calculated for each line-profile in the beam-direction using this relative threshold, resulting in a 2D map. We found this method to be of limited use in our study because of the heterogeneity of the tissue in the beam path. In figure 6.1 can be seen that the production of ^{15}O is abruptly decreasing because of the oral cavity near the distal edge. When a relative threshold was used, the 50 % distal edge in the ^{15}O distribution was triggered by the presence of the oral cavity where no PET nuclides are produced, not by the end-point of the protons, which lies distal to the oral cavity. Due to the energy threshold of the production cross sections, only a small portion of the radiation was produced after the oral cavity. Another complicating factor was that the maximum in the line profile changes when a dense water insert is applied because of the increase in production at the location of the insert. This caused the 50 % distal falloff to be at another level and it led to another location of the distal edge caused solely by the change in maximum. Proton range differences in heterogeneous tissues could not be reliably measured this way. Better results were achieved when defining the distal edge position using an absolute threshold level; a level that was the same for all profiles and thus does not depend on details of each profile: when following a line profile starting beyond the distal edge (where the profile is zero) towards the incoming proton beam, the distal edge position was defined as the first position at which the profile crosses the threshold. The threshold was chosen at a level as low as possible just above the statistical fluctuations of the distribution. Subtracting the distal edge maps of the unmodified patient from those of a modified patient, the distal edge difference map due to an insert was obtained. This distal edge difference was relatively stable with respect to the value of the threshold, as long as it was chosen above the level of the statistical fluctuations, but below the level where heterogeneities play a role.

6.3 Results

6.3.1 Production of PET nuclides and prompt gamma rays

Figure 6.2 shows results of the translation of the planning CT (into density and atomic concentration of oxygen and carbon), and of the simulation of the irradiation: the physical dose distribution, the amount of ^{15}O and ^{11}C positron emitters present at the end of the irradiation and the amount of 6.13 MeV and 4.44 MeV gamma rays created during the whole irradiation. We remind the reader that the positron emitter and prompt gamma distributions reflect the combination of proton fluence, energy dependent cross section and elemental composition. The shapes of the ^{15}O and 6.13 MeV distributions are somewhat

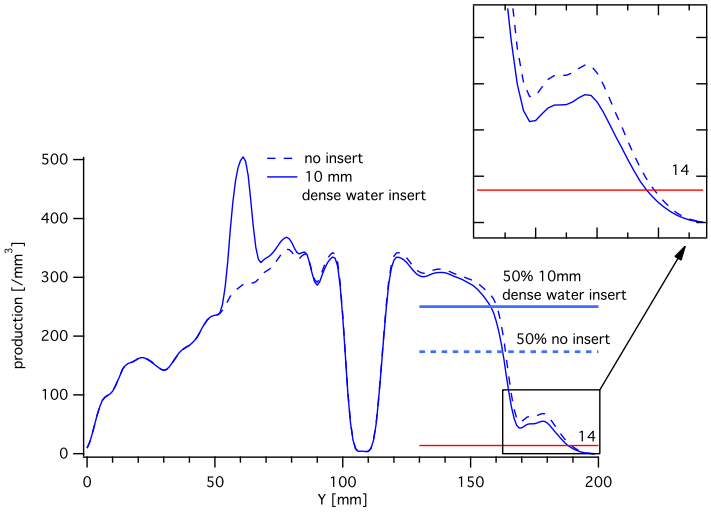

Figure 6.1: Illustration of the distal edge detection method. Shown are line profiles through the insert of produced ^{15}O for the unmodified patient and for the patient modified with a 10 mm dense water insert at Y = 60 mm. The beam enters from the left in the presented profile. Indications are placed for the 50 % distal falloff level as well as for the absolute threshold level of 14 radionuclides /mm^3. A cavity filled with air is present at Y = 108 mm, causing a production of 0. The oral cavity filled with air is located at Y = 170 mm, forcing an abrupt change in production of ^{15}O.

similar as they are both produced solely on ^{16}O. The difference between the ^{15}O and 6.13 MeV distribution stems from a different energy dependence of the cross sections. The ^{15}O production cross section has a higher threshold, its cross section maximum is at higher energy, and the cross section stays relatively large at higher energies whereas the 6.13 MeV gamma ray cross section drops quickly and continuously with increasing energy, which causes the highest production to be close to the distal edge. The 4.44 MeV gamma ray is produced on both ^{12}C and ^{16}O whereas ^{11}C is produced on ^{12}C, ^{14}N and ^{16}O. Although the production of ^{11}C on ^{14}N is rather unimportant because of the low abundance of nitrogen in the human body, it is taken into account in the simulations. The production on more than one target nuclide complicates the interpretation of the ^{11}C and 4.44 MeV gamma ray distributions in terms of the elemental composition. One does easily observe that they are more similar to each other than to the ^{15}O and 6.13 MeV distributions. Differences in the energy dependence of the cross sections similar to those discussed above for the production of ^{15}O and the 6.13 MeV gamma ray also play a role.

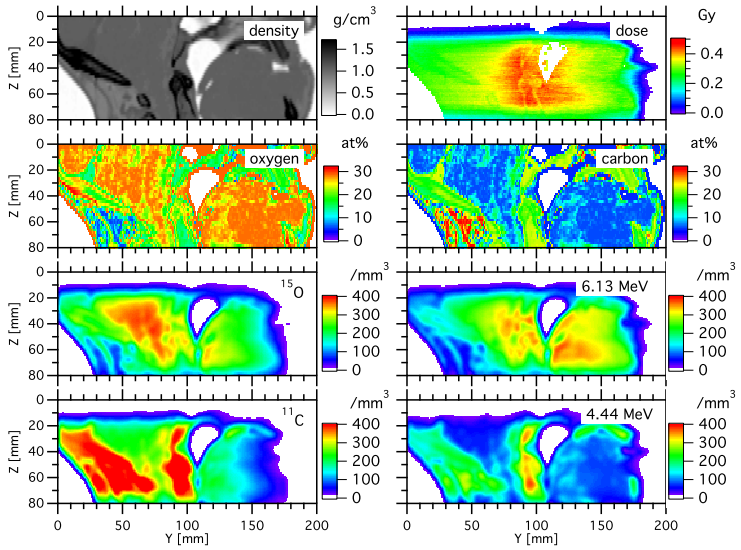

Figure 6.2: Results of the simulations. Shown is a sagittal slice through the location where the insert will be placed (see figure 6.3). The beam enters from the left. Results of the planning CT translation: mass density (top left) and atomic concentration of oxygen and carbon (2nd row). Results of the simulation of the irradiation: physical dose distribution (top right), amount of ^{15}O (3rd row left) and ^{11}C (bottom left) positron emitters present at the end of the irradiation and number of 6.13 MeV (3rd row right) and 4.44 MeV (bottom right) gamma rays created during the whole irradiation. In order to visualise the patient outline and air-filled features, the image value is set to white for an energy deposit below 2 % of the maximum in the dose distribution, for less than 0.1 g/cm^3 mass density in the oxygen and carbon atomic concentration images and for values below 5 % of their own maximum for the other secondary radiation distributions.

6.3.2 Sensitivity to compromised dose delivery

Figure 6.3 shows the effect on the secondary radiation distributions of introducing a 10 mm dense water and a 5 mm air insert in terms of the difference between the distributions for the unmodified (without the insert) and modified (with the insert) patients. The changes at the location of the insert are readily understood based on the density and composition of the inserts. Interestingly, for the 4.44 MeV gamma ray, the dense water insert is hardly visible. By chance, the change in density and elemental composition due to the insert, combined with the specific treatment plan details and reaction cross sections results in an equal amount of 4.44 MeV gamma rays produced in this region with or without the insert.

However, this study concentrates on the clinically more relevant ef-

fect the inserts have on the distribution of the secondary radiation beyond the insert. Obviously, a shortening of the proton range (dense water insert) leads to a decrease of production in the distal edge area, while an extension of the range (air insert) produces the opposite effect. The fact that the effects of a high- and low-density insert are opposite is seen all along the region between the insert and the distal edge. The streaks seen above and below the inserts are indicative of the statistical accuracy of the Monte Carlo simulations. The number or protons simulated was taken sufficiently high to ensure that these statistical effects are significantly smaller than the effect of the 5 mm spherical insert, see figure 6.3, right.

For the PET nuclides distributions, the modified patient distributions show a sizable change compared to the unmodified one over the whole region from the insert to the distal edge. For the prompt gamma ray distributions, the change in the modified patient is more concentrated at the distal edge. Also, the prompt gamma ray distributions show a large change immediately beyond the insert, a region where the PET nuclides show very little change. These differences have their origin in the different energy dependence of the respective cross sections. The prompt gamma ray cross sections decrease more rapidly with increasing energy beyond their low-energy maximum than the PET nuclide production cross sections. This effect is illustrated in figure 6.4 where line profiles along the Y-coordinate through the center of the insert are compared. A change in density basically shifts the production distributions beyond this density change. So in regions where the secondary radiation distribution is flat on a distance scale larger than the size of the insert, the insert will not cause a difference in the production.

Only in regions where the production cross section shows a slope, a density change may lead to a difference in production. The distal edge of course represents a slope in the production that will always show a change when density changes along the proton path occur. Target underdosage or additional dose to normal tissue will be directly caused by such differences. Assurance of a correct distal edge position, which is related to the proton beam range, is therefore a primary application of *in vivo* dose delivery verification. However, our realistic clinical example shows that along the proton beam path, the situation is more complicated. For example, just beyond the insert, PET nuclide production is constant in a homogeneous region (between Y $\approx$ 70 to 80 mm) and thus the insert shows no effect on the local PET nuclide production. A change in production of secondary radiation is always indicative of a change with respect to the treatment plan, but from the absence of a local change in secondary radiation it can not be concluded that no density changes have occurred.

The distal edge region is the least visible in the ^{11}C distribution because the distal edge of the irradiation is in oxygen-rich, carbon-poor tissue (see figure 6.2) and the production cross section of ^{11}C on ^{16}O is rather small. The

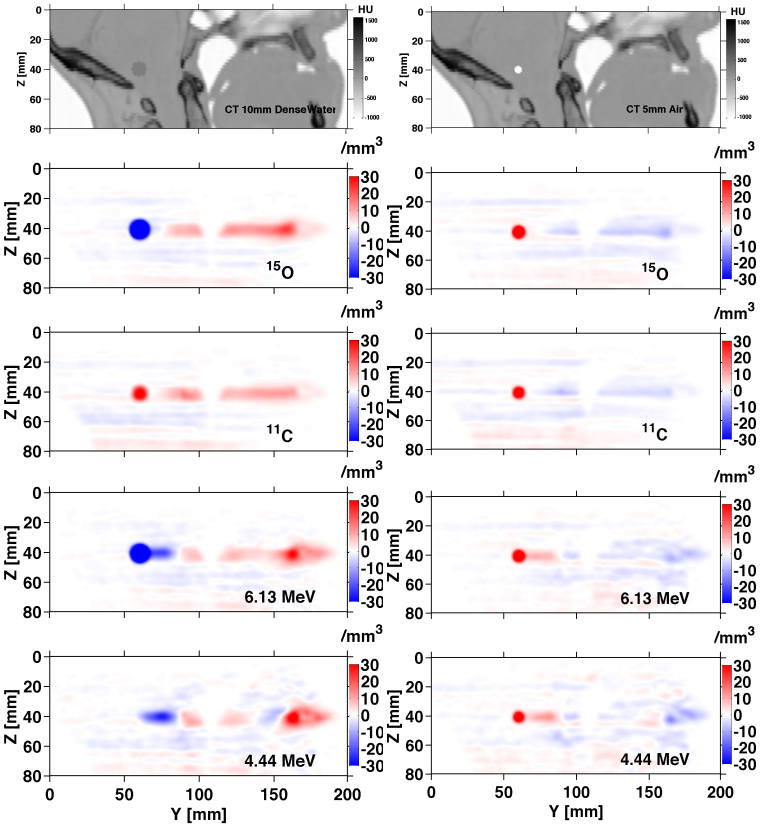

Figure 6.3: The effect of a 10 mm dense water (left column) and 5 mm air (right column) insert. The top row shows the inserts (at Y = 60 mm, Z = 40 mm) in the density distribution as implemented in the treatment planning CT. Shown is the difference of the secondary radiation distributions, unmodified minus modified patient. Red regions indicate a lower production in the modified CT and blue regions indicate a higher production. The same sagittal slice, going through the center of the inserts, as used throughout the chapter is shown.

effect of the inserts is similar for ^{15}O and both prompt gamma rays. However, for the prompt gamma rays and the dense water insert, the effect at the distal edge extends over a larger region in Y than for the PET nuclides due to the lower reaction threshold of the prompt gamma rays combined with the presence of the small air cavity in the distal region (see figure 6.2, top left, at Y ≈ 170 mm, Z ≈ 40 mm). The protons lose a factor 1000 less energy in this cavity, so the proton range shortening caused by the insert is amplified in the region where prompt gamma rays have a high production cross section.

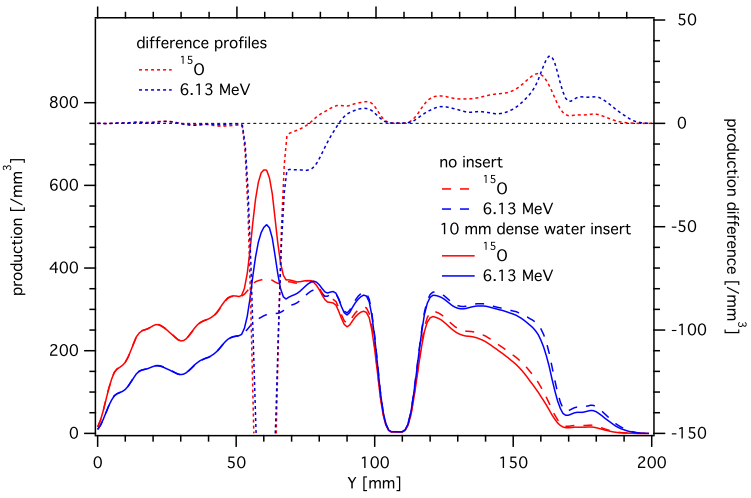

Figure 6.4: Line profiles along the Y-coordinate through the center of the insert. The solid and dashed lines (left vertical scale) show the profiles through the ^{15}O (red) and 6.13 MeV (blue) production distributions for the patient with a 10 mm diameter dense water insert and without an insert. The dotted lines (right vertical scale) show the difference of the profiles between the patient without and with insert (these are thus profiles through the difference distributions shown in figure 6.3).

The distal edge maps of the PET and prompt gamma distributions (see section 6.2.3) are determined using an absolute threshold of 14 radionuclides/mm^3, a level at which the statistical fluctuations in the distributions are sufficiently small but the heterogeneities do not yet play a role. Figure 6.5 shows the distal edge difference maps for the 10 mm dense water and 5 mm air inserts. Distal edge difference maps of the dose distributions are included for reference, using an absolute threshold of 21.5 mGy (5 % of the SOBP dose). The comparison of the dose distal edge images with the PET and prompt gamma ray distal edge images show that distal edge differences in the PET and prompt gamma ray distributions can serve as a proxy for distal edge differences in dose distributions.

The difference in range is clearly seen at X = 110 mm, Z = 40 mm, the location of the insert in the coronal plane. The 10 mm dense water insert produces a change in proton range roughly of the same magnitude but of opposite direction as the 5 mm air insert since the absolute value of the change in areal density with respect to the unmodified patient is very similar, about 0.5 g/cm^2 through the center of the insert. Since the inserts are spherical, the maximum range change will occur at the location of the center of the insert and taper off to zero at the edges. This means that the larger insert, while introducing com-

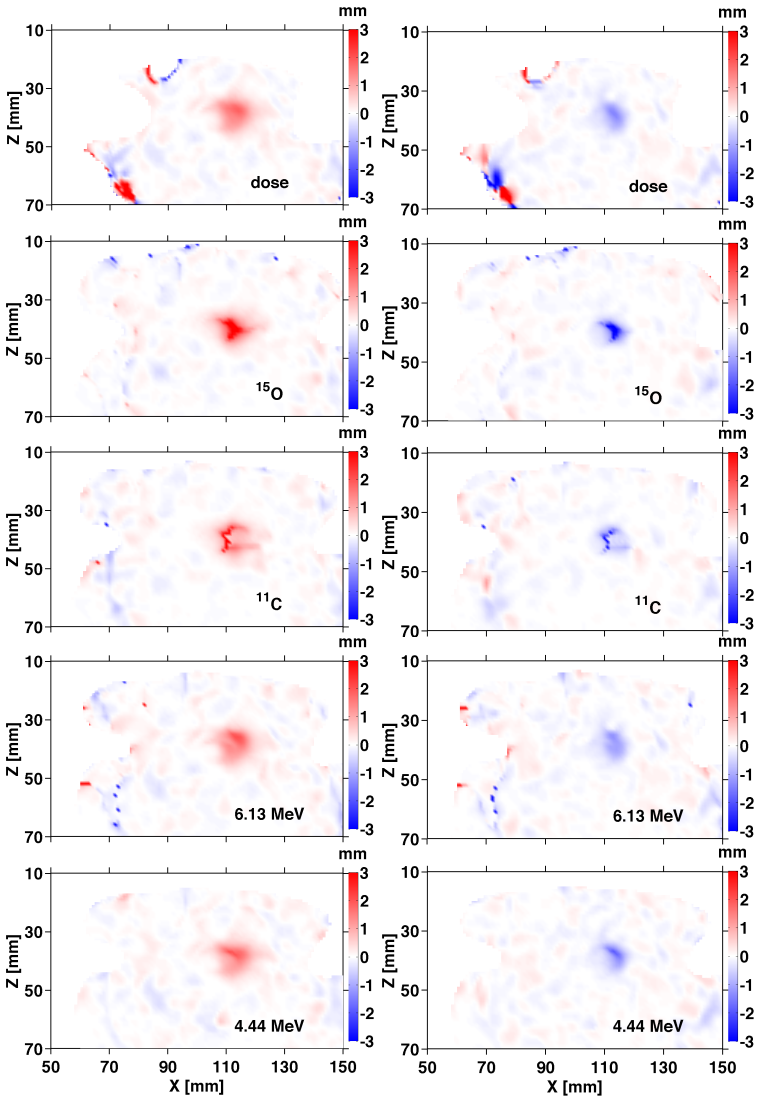

Figure 6.5: Distal edge difference maps for the 10 mm dense water (left column) and 5 mm air inserts (right column). The insert is located at X = 110 mm and Z = 40 mm. The distal edges are determined using an absolute threshold and the difference is calculated between the distal edge maps of the unmodified patient and the modified patient. Red regions indicate a decrease in distal edge and blue regions indicate an increase in distal edge. This is shown for the dose (top row), PET nuclides (2nd and 3rd row), and prompt gamma rays (4th and 5th row).

parable proton range shifts, is easier to detect since the affected region is larger. It is interesting to observe that the spherical inserts do not necessarily show a circular effect in the distal edge difference maps; this is most dramatically seen for ^{11}C. The origin of this lies in the heterogeneity in elemental composition of the irradiated tissue, the presence of a small air cavity in the distal edge region (see figure 6.2, top left, at Y $\approx$ 170 mm, Z $\approx$ 40 mm) and the different energy dependence of the reaction cross sections. The distal edge change caused by the inserts is most clearly seen in the ^{15}O distribution; both prompt gamma ray distributions show comparable performance while the ^{11}C is most susceptible to the tissue heterogeneity and therefore has the weakest correlation with the presence of the insert.

6.4 Discussion

Imaging of PET nuclides and prompt gamma rays are methods intended for *in vivo* dose delivery verification. To be clinically useful, the distributions of PET nuclides and prompt gamma rays should be sensitive to dose delivery deviations. We have performed a Monte Carlo simulation study of a typical head-and-neck case, characterized by a strongly heterogeneous irradiated volume (both in density and composition). In the case studied, ^{15}O and the 6.13 MeV and 4.44 MeV prompt gamma rays show a similar sensitivity to artificial anatomical changes and resulting dose changes, as indicated in the sagittal profile. Looking at the distal edge position, the ^{15}O distribution is somewhat more sensitive to anatomical changes and dose changes than the prompt gamma rays. For both analysis methods, ^{11}C is least sensitive. The effect of anatomical changes along the proton path on the production of PET nuclides and prompt gamma rays is complex as it depends on the combination of the irradiation parameters, the density and elemental composition of the irradiated tissue and the energy dependence of the nuclear reaction cross sections. Because of this complexity, other clinical cases with different tissue characteristics and different irradiation parameters may show different results. It follows that optimization of *in vivo* dose delivery verification requires detailed investigations of a variety of clinical cases; irradiation on simple phantoms do not capture the full complexity of the problem.

The Monte Carlo studies on different patient cases by Moteabbed et al. (2011) show that tissue heterogeneities result in non-uniform differences between the distal edges of the dose distribution and the PET nuclide and prompt gamma ray distributions: across the field of irradiation, large fluctuations in the distal edge differences are observed. Our study shows a similar effect caused by tissue heterogeneities by looking at changes in the PET nuclide and prompt gamma ray distributions caused by density changes along the beam path. Our study is however more directly related to imaging for *in vivo*

dose delivery verification as it indicates how images will change due to dose delivery deviations.

Verburg and Seco (2014) demonstrate that the 6.13 MeV and 4.44 MeV prompt gamma rays have a more favourable relationship with the Bragg peak than the ensemble of all prompt gamma rays. The production cross section of these combined gamma rays shows an energy dependence similar to that of the PET nuclides: a relatively high threshold, a broad peak and a slow decrease at higher proton energies. We observe in our study that changes in 6.13 MeV and 4.44 MeV prompt gamma ray production along the beam direction due to a change in density are more peaked at the distal edge than changes in PET nuclide production (figure 6.3). Taking into account the ensemble of prompt gamma rays would show a picture similar to that of the PET nuclides as the different behaviour has its origin in the different energy dependence of the cross section as compared to that of the 6.13 MeV and 4.44 MeV gamma rays.

6.5 Conclusion

Using detailed Monte Carlo simulations, we have shown that dose delivery deviations in the case of heterogeneous tissues, exemplified in our case by the introduction of density changes along the proton path of a typical head-and-neck clinical case, have a rather complex effect on the production of PET nuclides and prompt gamma rays: it depends on the combination of the irradiation parameters, the density and elemental composition of the irradiated tissue and the energy dependence of the nuclear reaction cross sections. We have shown that for the case studied, ^{15}O demonstrates overall the highest sensitivity to a compromised patient treatment delivery. The deviations due to the 5 mm insert that could be identified show that changes in the order of the treatment planning margin can be identified. The study of other patient categories will show whether the fact that ^{15}O shows the largest modification to its distal edge position is rather general or whether other signals have the largest sensitivity in other cases. We conclude that without further data there is currently not yet a unique answer as to which imaging modality is best for all patient treatments; continued optimization of both PET and prompt gamma imaging is needed to arrive at the best clinical implementation for all patient categories.

Chapter 7

Comparison of PET and Prompt Gamma Imaging – additional patients

7.1 Introduction

This study aims to provide a quantitative measure of the differences between PET and prompt gamma ray imaging in proton therapy treatments as well as to investigate optimal imaging protocols. In chapter 6, a single field for a single irradiation was examined in detail regarding the local differences in distal edge position and the challenges in the detection of anatomical changes. The results from additional case studies are presented in this chapter. Irradiation of two head and neck patients and one spinal sarcoma irradiation were simulated and analyzed using the simulation software described in chapter 5. Two types of deviation from the treatment plan were investigated: patient mispositioning/misalignment and an overall range deviation introduced by e.g. an uncertainty in the conversion of the planning CT Hounsfield units to proton stopping power.

7.2 Materials and Methods

7.2.1 Treatment plans

Three anonymised treatment plans were obtained from the radiotherapy department of the UMCG. This procedure was in compliance with the guidelines to share patient data for research in an anonymous way. The plans were chosen to represent typical patients that will receive proton therapy treatment in The Netherlands. Treatment plans, planning CTs and dose distributions as calculated by the treatment planning system (TPS) for two head and neck patients and one spinal sarcoma patient were anonymized and used in this study. The specifics of the irradiation properties are summarized in table 7.1. The treatment plans were created using robust optimization in the RayStation TPS (RaySearch Laboratories), which entails the separate optimization of each pencil beam weight under possible variations of tissue stopping power and patient misalignment of up to 3 % and 3 mm. When using robust optimization, the effect of possible stopping power deviations and misalignment on the resulting total dose distribution is minimized at the treatment planning phase. The dose distributions of separate fields might look counter-intuitive as a result of the optimization procedure, however the overall dose distribution is robust against deviations in the individual fields.

Dose distributions from the treatment planning system can be seen in figures 7.1, 7.2 and 7.3. The first head and neck patient receives two coplanar anterior fields, each 45° from the vertical. Dose is delivered around the skull base as well as left and right of the cervical spinal cord. The second head and neck patient receives four non-coplanar fields irradiating mainly the left side of the skull base and neck. The effect of the robust optimization can be seen, as the dose is delivered using several patched fields. The spinal sarcoma patient is placed in the prone position to allow better beam access to the tumor. Three coplanar fields are planned, one in the y-direction and two fields 40° on each side, irradiating respectively the center, the right and the left side of the tumor.

7.2.2 Beam model

To accurately model the proton transport in the patient, a good model of the delivered proton beams is required. In the present, theoretical, study, a comparison cannot be made against real measurements from an irradiation. The only references are the dose maps that are produced by the TPS. Using an extension to the TPS developed by RaySearch, as much information as possible was extracted about the beam model used for the IBA scanning nozzle model that was used to generate the treatment plans. This information was utilized to create the beam model for the Monte Carlo simulations.

The proton beams were modeled as 2D single gaussians in the

Table 7.1: Properties of the treatment plans for the first head and neck (h&n 1), the second head and neck (h&n 2) and the sarcoma patient. Energy range denotes the nominal energy range. Range shifter thickness is indicated in Water Equivalent Thickness (WET). Field directions and couch angles are given with respect to the y-axis (anterior-posterior).

property	h&n 1	h&n 2	sarcoma
fields	2	4	3
range shifter WET [mm]	75	40	40
field 1			
field angle [°]	45	305	0
couch angle [°]	0	340	0
energy range [MeV]	104 to 202	75.2 to 188	75.4 to 147
spots	1.1×10^4	5.3×10^3	2.2×10^4
protons simulated	1.49×10^8	8.27×10^7	1.39×10^8
irradiation time [s]	64.1	63.6	79.1
field 2			
field angle	315	210	320
couch angle	0	40	0
energy range [MeV]	104 to 205	75.2 to 216	75.4 to 147
spots	1.1×10^4	2.4×10^3	1.7×10^4
protons simulated	1.50×10^8	3.01×10^7	1.43×10^8
irradiation time [s]	64.9	65.3	71.0
field 3			
field angle		55	40
couch angle		20	0
energy range [MeV]		75.2 to 177	71.8 to 147
spots		5.4×10^3	2.1×10^4
protons simulated		8.56×10^7	1.44×10^8
irradiation time [s]		60.3	76.6
field 4			
field angle		150	
couch angle		320	
energy range [MeV]		75.2 to 216	
spots		2.7×10^3	
protons simulated		3.49×10^7	
irradiation time [s]		66.1	

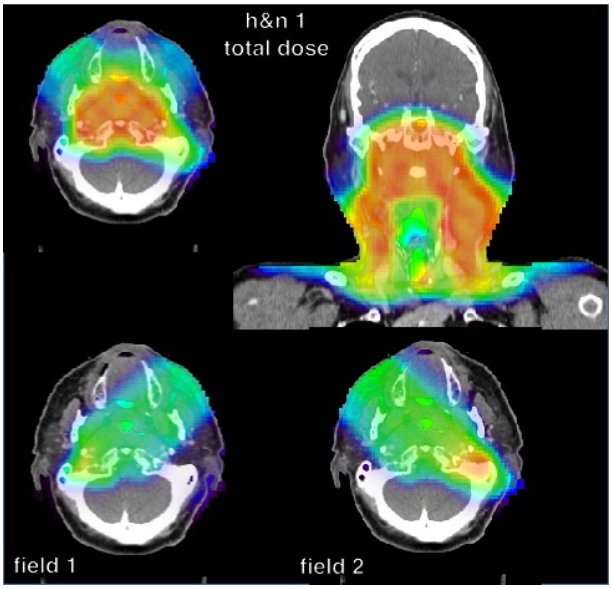

Figure 7.1: Dose distributions from the treatment planning system overlaid on the patient CT for the head and neck 1 irradiation. Each dose distribution uses a color scale that is normalized to its own maximum.

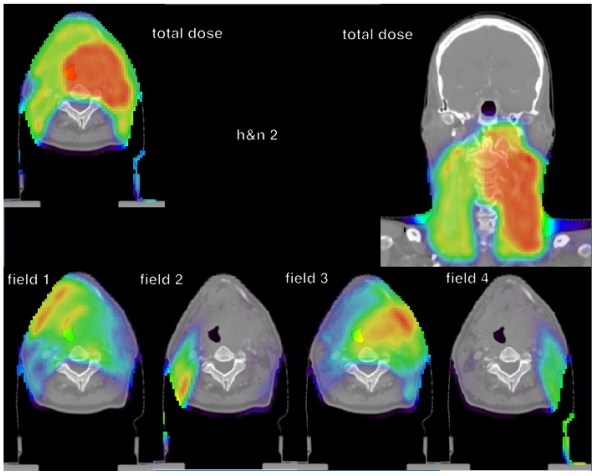

Figure 7.2: Dose distributions from the treatment planning system overlaid on the patient CT for the head and neck 2 irradiation. Each dose distribution uses a color scale that is normalized to its own maximum.

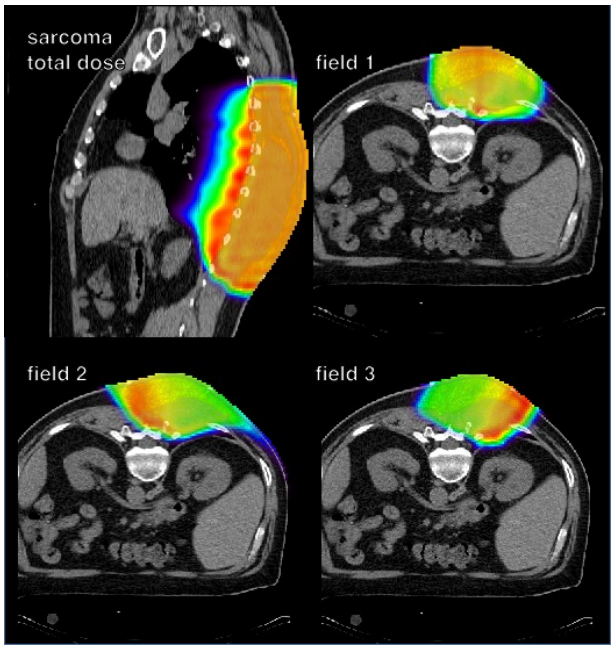

Figure 7.3: Dose distributions from the treatment planning system overlaid on the patient CT for the sarcoma irradiation. Each dose distribution uses a color scale that is normalized to its own maximum.

transversal direction with the FWHM given by the treatment plan. A virtual source axis distance (VSAD) was implemented as depicted in figure 7.4, corresponding to the VSAD obtained from the treatment plans. In the left-right direction, a VSAD distance of 2.25 m was used. Perpendicular to that, in the superior-inferior direction, a VSAD distance of 1.83 m was used. Primary protons were generated in the so-called generator plane perpendicular to the isocenter-VSAD direction. Their initial position was sampled from the 2D gaussian distribution and their direction was given by the spot-VSAD direction, leading to parallel initial proton trajectories within a spot. A PMMA range shifter was placed in between the initial position of the protons and the patient so that the energy loss and scattering in the range shifter was included in the simulation.

7.2.2.1 Energy distribution of the primary proton beam

The initial energy of the primary protons in the Geant4 simulations was sampled according to the spectra used in the RayStation TPS for dose calculations. These spectra were extracted from the TPS in three batches, a low energy batch

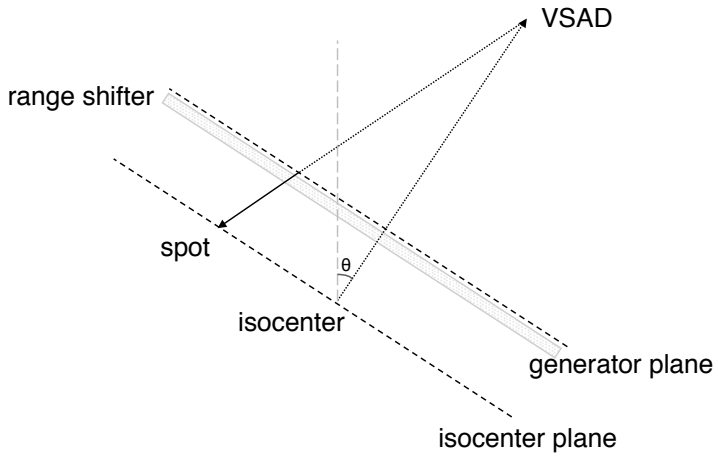

Figure 7.4: Geometry of the simulated beam model. The isocenter position and gantry angle (θ) are used to create the isocenter plane. The virtual source axis distance (VSAD) describes the virtual 'focus point' from which the pencil beams seem to originate. The VSAD can have a different value for both transversal directions. Primary protons are generated in the generator plane, just above the range shifter, with a direction given by the VSAD-spot direction. In the generator plane, their initial position is determined using a 2D single Gaussian distribution.

from 75.2 to 106.1 MeV, a middle energy batch from 147.1 to 170 MeV and a high energy batch from 187.5 to 209.1 MeV. Figure 7.5 shows the extracted high energy spectra that were available as input to the simulations. We were unable to extract spectra from the TPS for energies in between these batches, due to an upgrade of the RayStation software that rendered the extraction method unusable. The nominal energy of the spectra shown in figure 7.5 is a label used in the TPS to describe the beam being delivered to the patient. Both the average and peak energy of each spectrum are lower than the nominal energy describing the beam. A peak close to the nominal energy is seen, along with a low energy tail with a weight about a factor of 10^2 to 10^3 lower. For the highest energies, a clear separation between the peak and the low energy tail is seen, with nothing in between. A physical reason for this effect is not known to us, but we have modeled the energy distribution as shown in order to maintain conformity between the treatment plans and the simulations.

In the treatment plan, additional nominal beam energies were used for which no spectrum was available. To approximate their sampling distribution, the closest spectrum with a lower nominal beam energy was used and the energy of the spectrum was scaled up according to the ratio of nominal beam energies, while keeping the same shape. Specifically in the range be-

tween 106.1 to 147.1 MeV, no input spectra were available and the energy was sampled using this interpolation procedure.

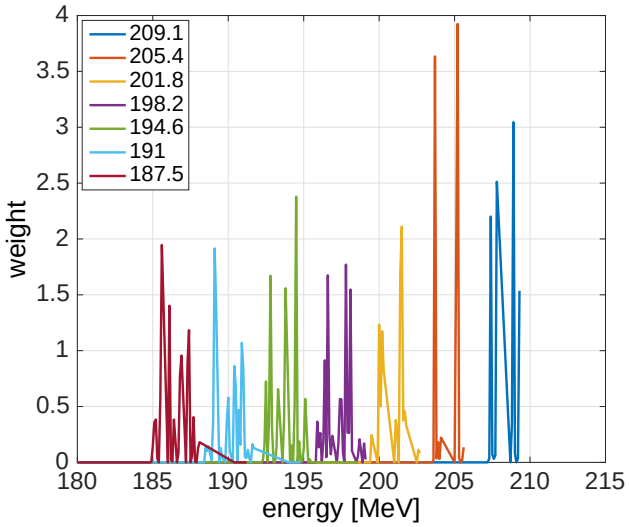

Figure 7.5: Energy distribution of layers with a high nominal energy extracted from the RayStation treatment planning software. The nominal energy [MeV] for a spectrum is given by the label. The weight of the distribution is unnormalized. The sharp spikes in the figure are caused by the shape of the histograms.

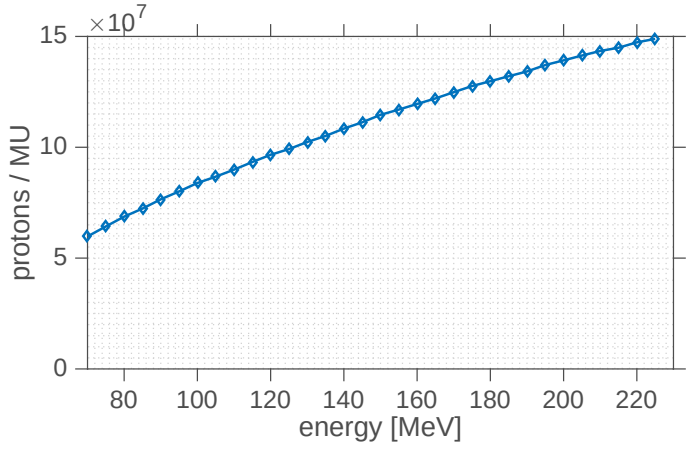

Figure 7.6: Protons per monitor unit (MU) as a function of the nominal beam energies.

7.2.3 Time structure of the beam delivery

The order in which the fields and energy layers are delivered to the patient and the associated timing structure have an effect on the PET image measured after the irradiation has completed. For the simulations, the energy layers were irradiated in ascending order, starting with the irradiation of the lowest energy and ending with the highest energy, which contributes to the distal edge of the irradiation. This optimizes the number of positron emitting nuclides that are still available to be imaged by a PET scanner and have not yet decayed. Irradiating in this way has no effect, positive or negative, on the prompt gamma ray image that can be measured. The timing structure used for the simulations are typical values for an IBA C230 cyclotron with pencil beam scanning. A spot-to-spot switching time of 1.5 ms was implemented as well as an energy switching time of 1.2 s. The proton beam intensity through the scanning nozzle was assumed to be 1.5×10^{10} pps for all beam energies. The irradiation time of each spot was determined by the beam intensity and the amount of protons to be delivered. The time structure of the beam delivery combined with this beam intensity led to irradiation times of 60 to 80 s per field. Each field was simulated independently using the clinical beam intensity scaled down with a factor of 1×10^{3} to obtain reasonable simulation times.

7.2.4 Proton fluence calibration

The treatment planning software gives the weight of each spot in each energy layer as a fraction of the total amount of monitor units (MU) that will be delivered to the patient. To simulate the proton delivery, this number of MUs needs to be converted to an amount of protons. The number of protons per monitor unit as a function of the nominal beam energy from the RayStation TPS at the UMCG is displayed in figure 7.6. The shape of the relationship follows the stopping power in air for protons as the MUs are measured during an irradiation with an air ionization chamber.

7.2.5 Statistical precision of the simulations

The precision of Monte Carlo simulations depends on the number of simulated primary particles. Simulating more primary particles increases the precision of the results at the cost of longer simulation time. For the simulations discussed in this chapter, a fixed proportion of primary particles was used: 1 in 1000 protons. The resulting level of statistical precision of the simulation outcomes was investigated.

The first field of the sarcoma patient was simulated 10 times, and each simulation was split in 150 parallel independent jobs. To ensure statistical independence between all datasets, each job was initialized with a different

(random) value of the seed for the random number generator (RNG) in the code. After the simulations had finished, each split simulation was merged using the data merger to yield 10 independent simulations of the same irradiated field. The variability between these simulations was analyzed on a voxel-by-voxel basis using the coefficient of variation CV, which is defined as the relative standard deviation

$$CV = \frac{\hat{\sigma}}{\hat{\mu}} \times 100\%$$

where $\hat{\sigma}$ is the sample standard deviation of the voxel, and $\hat{\mu}$ the sample mean, using $N = 10$ samples. The distribution of CV values for this simulation has many values close to zero and a long tail. This is caused by two phenomena. Firstly, many voxels at the edge of the region of interest will have a value of zero, since no particles have reached that far. The CV of identical values is 0, leading to many voxels with a CV of 0. At the edge of the irradiation field, the number of particle interactions drops to 0. In this region, the value of some voxel is determined by very few interactions, leading to a very high variability. This causes the long tail of CV values.

Removing the voxels described previously from the dataset can improve the usability of our CV dataset in determining the variability of the simulations. This is implemented by a cut on the original data, removing voxels with a value less than 10% of the global maximum, forcing the CV dataset to values inside the proton field.

7.2.6 Secondary radiation images

During the simulation, the production of prompt gamma rays and PET nuclides was calculated. For the prompt gamma rays, a cumulative image of the gamma rays with E_γ = 6.13 MeV and 4.44 MeV is created that represents the total emission of these gamma rays during the simulated field. The simulated PET nuclides are ^{15}O, ^{14}O, ^{11}C, ^{10}C, ^{13}N, ^{30}P and ^{38}K, produced on the elements O, C, N, P and Ca. Decay during the irradiation as well as biological washout during the irradiation are taken into account, resulting in an image per nuclide that represents the nuclide distribution at the end of the irradiation of each field.

In this chapter, we compare the two imaging modalities' ability to detect a compromised dose delivery, so secondary radiation images are created that represent realistic imaging scenarios that could be implemented in a clinical work-flow.

For PET imaging, two different scanning scenarios are investigated. *(i)* a scan of 120 s directly after the first field is irradiated. This approach ensures the distal edge of the field does not overlap with contributions from other fields, leaving a sharper edge at the distal end of the field. *(ii)* a scan of 120 s after the final field. This maximizes the total irradiated volume at the time of

the PET scan, leading to potentially more available counts. For this second protocol, decay and washout of the nuclides during the gantry rotation is also taken into account. A gantry rotation speed of 360 °per minute is assumed with an additional delay of 5 s between the end of the motion and the start of the irradiation of the next field.

For prompt gamma ray imaging, the image that can be obtained depends on the measurement technique used and the way the detector system is synchronized with the irradiation. For instance, separate low-statistics images of each pencil beam spot could be obtained, or an image of an energy layer in the case of passive scattering (Richter et al., 2016). To compare the images of PET and PGI that one could measure, a combined prompt gamma ray emission map for the two gamma ray lines is created. This corresponds to a hypothetical prompt gamma ray imaging device that sums the detected counts during the irradiation. In this way, the ability is lost to extract information regarding the elemental composition of the irradiated tissue, as is done by e.g. Verburg and Seco (2014) and Hueso-González et al. (2018). However, this approach is comparable to the type of images one could obtain by e.g. the knife-edge slit camera (Smeets et al., 2012).

For both PET and prompt gamma ray imaging, a realistic spatial resolution that models the imaging resolution was introduced by applying 3-dimensional Gaussian blurring with a FWHM of 4 mm. This resolution is realistic for a typical clinical PET scanner and has yet to be achieved by most prompt gamma ray imaging devices. The clinically most advanced prompt gamma ray imaging prototype, the knife-edge slit camera, obtained a 1D spatial resolution of 21 mm FWHM (Smeets et al., 2012).

7.2.7 Sensitivity to compromised dose delivery

The sensitivity of PET and prompt gamma ray imaging to detect changes in the delivered dose distribution was studied by modifying the treatment in two ways:

- A positioning deviation was implemented by applying an isocenter position shift of 3 mm in the superior direction with respect to the planning isocenter. This lateral shift is chosen as it will produce an effect for all fields, in contrast with for instance a shift in the dorsal-ventral direction, which would yield no difference for fields with a gantry and couch angle of 0°.

- To simulate a deviation in the calculated proton range, the planning CT HU to proton stopping power conversion procedure was modified. The patient was altered by increasing the mass density with 3 percent while keeping the tissue composition the same.

7.2.7.1 Gamma index analysis

The sensitivity to a compromised dose delivery is investigated using the gamma index (Low, Harms, Mutic, & Purdy, 1998), which is often used in radiotherapy to evaluate differences in dose distributions. The dose paradigm will be used in the formalism, but the method can directly be applied to all other types of 3D images, such as the prompt gamma ray image or the PET image. The gamma index combines two analysis components: dose difference and distance to agreement (DTA). Dose difference δ is defined as

$$\delta(\vec{r}_m, \vec{r}) = D(\vec{r}) - D_m(\vec{r}_m)$$

with D_m the reference dose distribution, D the dose distribution that is compared to the reference, $\vec{r}$ a 3D position vector and $\vec{r}_m$ the position in the reference dose distribution. The distance to agreement is incorporated using a term r, which is defined as the distance between the positions $\vec{r}$ and $\vec{r}_m$

$$r(\vec{r}_m, \vec{r}) = |\vec{r} - \vec{r}_m|$$

The gamma index $\gamma(\vec{r}_m)$ at point $\vec{r}_m$ is then defined as

$$\gamma(\vec{r}_m) = min\{\ \Gamma(r_m, r_c)\ \} \quad \forall \vec{r_c}$$

with

$$\Gamma(r_m, r_c) = \sqrt{\frac{r^2(\vec{r}_m, \vec{r}_c)}{\Delta d_M^2} + \frac{\delta^2(\vec{r}_m, \vec{r}_c)}{\Delta D_M^2}}$$

with Δd_M the DTA criterion and ΔD_M the dose difference criterion. Typically the DTA criterion is set to 3 mm and the dose difference criterion is set to 3 %. Whenever the gamma index $\gamma(\vec{r}_m)$ for a voxel is larger than 1, it is said to have failed the criteria, and when it is smaller than or equal to 1, the voxel has passed the criteria. However, some information is lost when approaching the gamma index as a pass/fail analysis tool. More information can be extracted by investigating the distribution of gamma values of the entire 3D image.

Using the dose paradigm to compare planned dose distributions to e.g. simulated dose distributions, values of the gamma index larger than 1 are usually a bad sign. They indicate dissimilarity where it was not expected. However, in this use-case, we are interested in the imaging protocol and modality that shows the largest deviation when a compromised dose delivery occurs. When the images of the compromised dose delivery are compared to the images of the planned dose delivery, high gamma values indicate a large sensitivity to detect these changes.

Table 7.2: Simulation variability expressed using the coefficient of variation (CV). The first distribution set uses $1 \times 1 \times 1$ mm^3 voxels. The second distribution set contains the same data rebinned on a $2 \times 2 \times 2$ mm^3 voxel grid, reducing the variability. Mean, median and standard deviation of the CV values are calculated using all voxels that exceed 10 % of the global maximum of the distribution.

distribution	mean CV [%]	median CV [%]	std. dev. CV [%]
1) dose	3.4	2.6	2.8
1) ^{15}O	1.95	1.86	0.64
1) ^{11}C	2.03	1.90	0.73
1) 6.13 MeV gamma	2.61	2.34	1.17
1) 4.44 MeV gamma	2.05	1.90	0.78
2) dose	1.62	1.29	1.00
2) ^{15}O	0.99	0.93	0.33
2) ^{11}C	1.02	0.95	0.37
2) 6.13 MeV gamma	1.30	1.17	0.57
2) 4.44 MeV gamma	1.03	0.95	0.39

7.3 Results and discussion

7.3.1 Simulation variability

The histogram and boxplot of the CV distribution of the dose and ^{15}O production can be seen in figure ??. An overview of descriptive statistics of the CV distributions can be seen in table 7.2. The simulation results were obtained for a voxel size of $1 \times 1 \times 1$ mm^3. This fine voxel grid is useful for simulation purposes, but leads to a high voxel-to-voxel variability. To analyze the variability of the simulations on a grid that more closely resembles the introduced imaging resolution of 4 mm FWHM, the simulation results were rebinned on a $2 \times 2 \times 2$ mm^3 voxel grid. For the dose distribution, this means averaging the values within the new voxel, while the values were summed for the prompt gamma ray and PET production distribution.

When rebinning the data on the $2 \times 2 \times 2$ mm^3 voxel grid, the mean, median and standard deviation of the CV distribution are reduced to about half of the values for the fine grid. The average deviation from the mean simulated value is equal to 1.62 % for the dose distribution, 0.99 % and 1.02 % for the ^{15}O and ^{11}C production distribution respectively, and 1.30 % and 1.03 % for the 6.13 MeV and 4.44 MeV gamma ray distributions respectively. Variability is lower for the production distributions, since partial production of nuclides was allowed. Partial production means that one interaction in a voxel could produce a fraction of a nucleus. Overall, the total number of produced nu-

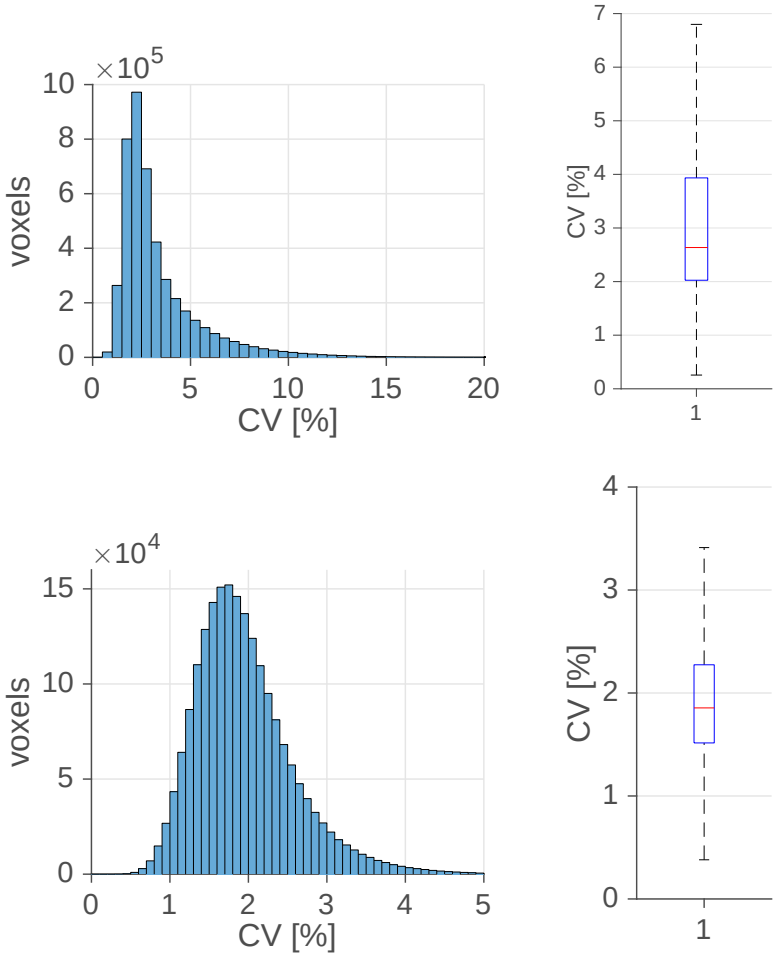

Figure 7.7: Histogram and boxplot of the CV distribution of the dose (top) and ^{15}O (bottom) distribution. For the boxplot, the central mark is the median, the edges of the box are the 25th and 75th percentiles and the whiskers extend to the most extreme data points not considered outliers. Outliers are not displayed.

clei will remain the same as for the physical unfractionated production, but the Poisson noise due to the lower level of simulated protons is reduced. This method of calculating the production acts as a variance reduction technique. The value of 0.99 to 1.30 % variability in voxel values for the production distributions provides confidence that the statistics level of 1 in 1000 simulated

protons is enough to be able to draw conclusions from our simulations.

7.3.2 Gamma index analysis

A typical result to illustrate the 3D gamma index analysis is shown in figure 7.8. Shown are slices of the 3D gamma index image for the sarcoma patient using the first PET scanning protocol, i.e. a scan of 120 s directly after the first field is delivered. The PET image of the planned situation is compared to the case where the isocenter was shifted 3 mm and to the case where the patient density was increased by 3 %. Several observations can be made from these images.

When the tissue density is increased by 3 %, an effect is measured equally over the entire irradiated volume. Roughly, the proton range is decreased by 3 %, meaning the same total energy is delivered to a smaller volume, leading to an increase in deposited energy by 3 %. Similar effects will occur in the PET and prompt gamma ray images. Large values of the gamma index are not very frequent, and extend to a value of 1.9. Most large gamma values occur close to local heterogeneities as well as near the end of the field in the beam direction. Also, a band where the gamma index drops to zero is seen at approximately two thirds of the proton range, indicated by the red box. This is caused by the fact that along the proton path production starts with a larger value, but the total range is decreased, leading to an earlier decrease to zero. When this happens, there must be a region where the production is roughly equal to the production in the planned case, leading to a gamma index close to zero.

When the isocenter is shifted by 3 mm, a large effect occurs over the entire irradiated volume, but it is highest at the lateral edge of the field, indicated by the red boxes. A region that measures counts where there were none in the planned case, or vice versa, leads to high values of the gamma index, up to 3.5, which is significantly higher than the maximum value of the gamma index for the 3 % density increase.

The total fraction of voxels that exceeds the gamma index threshold of 1 is shown in tables 7.3 and 7.4 for each patient, scanning protocol, imaging modality, and treatment modification. Table 7.3 uses gamma index parameters that are equal to the magnitude of changes we wish to detect, i.e. distance to agreement Δd_M = 3 mm and dose difference ΔD_M = 3 %. These values of the parameters lead to small fractions of voxels that fail the gamma index criteria. No more than roughly 0.5 % of voxels show a gamma index larger than 1. The first head and neck patient shows an advantage for prompt gamma ray imaging. It consistently shows more voxels that fail the gamma criterion. The differences are largest for the density increase modification, showing up to 10 times more failed voxels for prompt gamma ray imaging compared to PET. Detection of the 3 mm misalignment shows comparable results for PGI and PET. The second head and neck irradiation and the sarcoma irradiation show an advantage for

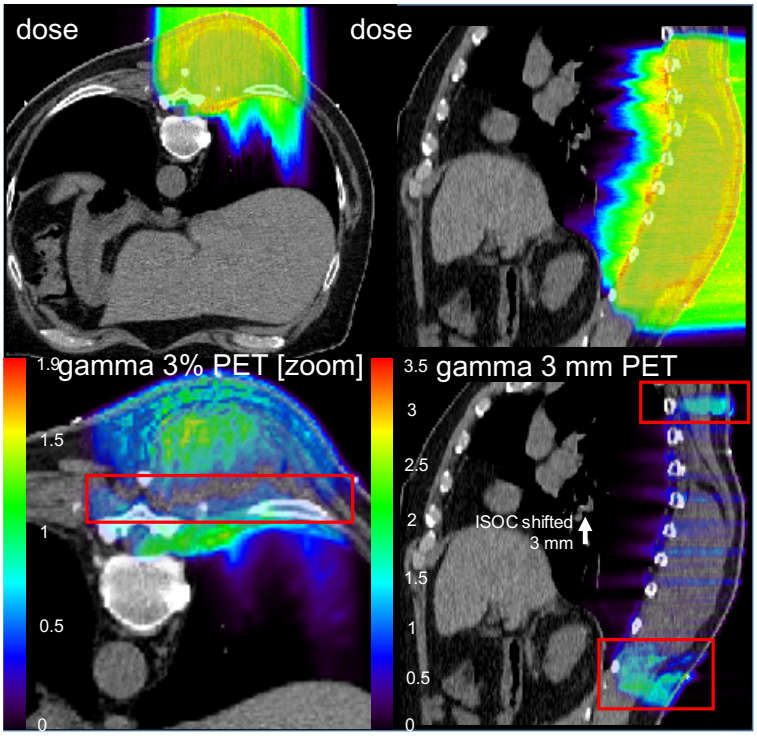

Figure 7.8: 3D gamma index analysis for the sarcoma patient. The top row shows the simulated dose distributions of the first field in the transverse and the sagittal plane. The gamma analysis for the PET scan after the first field with distance to agreement Δd_M = 2 mm and dose difference ΔD_M = 2% are displayed in the bottom row. The color scale is set to the total range of values in the 3D image. The bottom left image shows the transverse plane for the 3 % density modification. The bottom right image shows the sagittal plane for the 3 mm alignment modification. The direction of the applied isocenter shift is indicated with an arrow. Red boxes show regions of interest: for the 3 % density modification a region where the gamma index drops to zero and for the 3 mm alignment modification two regions with large gamma index.

PET. Six out of eight combinations of protocols and modifications favor PET for these patients. When combining the results from all three patients, six cases favor PET and six cases favor prompt gamma ray imaging. However, these results do not allow us to draw strong and definitive conclusions since very few voxels are detected as failing the gamma criterion.

Table 7.4 shows results for a more strict parameter setting of distance to agreement Δd_M = 2 mm and dose difference ΔD_M = 2 %. When compar-

Table 7.3: Gamma index over the threshold of 1 using distance to agreement Δd_M = 3 mm and ΔD_M = 3 %. Displayed in bold is the imaging modality that shows the most detected deviations.

patient	scan	modification	PET $\gamma > 1$ [%]	PG $\gamma > 1$ [%]
h&n 1	field 1	3 mm	0.495	**0.503**
		3 %	0.00778	**0.0775**
	final	3 mm	0.511	**0.517**
		3 %	0.0173	**0.0398**
h&n 2	field 1	3 mm	**0.29**	0.178
		3 %	0.00261	**0.0243**
	final	3 mm	**0.355**	0.245
		3 %	**0.0720**	0.00959
sarcoma	field 1	3 mm	**0.512**	0.250
		3 %	**0.118**	0.0742
	final	3 mm	0.177	**0.220**
		3 %	**0.0492**	0.0440

Table 7.4: Gamma index over the threshold of 1 using distance to agreement Δd_M = 2 mm and dose difference ΔD_M = 2 %. Displayed in bold is the imaging modality that shows the most detected deviations.

patient	scan	modification	PET $\gamma > 1$ [%]	PG $\gamma > 1$ [%]
h&n 1	field 1	3 mm	**2.14**	1.95
		3 %	**0.924**	0.858
	final	3 mm	**2.27**	2.04
		3 %	**0.994**	0.709
h&n 2	field 1	3 mm	**3.85**	1.71
		3 %	**0.346**	0.245
	final	3 mm	**4.75**	2.24
		3 %	**0.274**	0.0703
sarcoma	field 1	3 mm	**3.81**	1.97
		3 %	**0.695**	0.375
	final	3 mm	**2.58**	2.12
		3 %	**0.540**	0.226

ing imaging modalities, these results clearly show an advantage for PET. All patients, all protocols, and all modifications show a higher number of voxels that are detected as failing the gamma criterion for PET compared to prompt

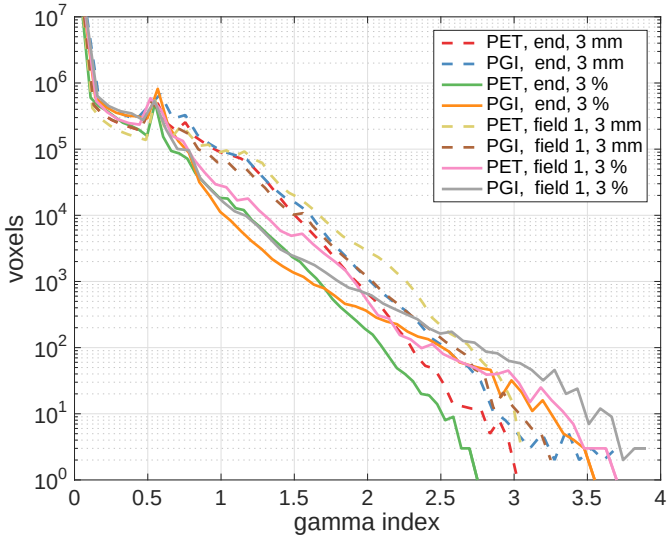

Figure 7.9: Gamma distribution histogram for the first head and neck patient using distance to agreement Δd_M = 2 mm and dose difference ΔD_M = 2 %. Solid lines indicate a 3 % density increase, dashed lines indicate a 3 mm mispositioning modification.

gamma ray imaging in a similar imaging scenario. The number of voxels with a gamma index larger than 1 is 8 % to 390 % higher when using PET compared to PGI.

Comparing the scanning protocols for the 3 mm mispositioning situation, a scan after the final field is almost always to be preferred compared to a scan after the first field, except for PET imaging of the sarcoma patient. The 3 % density increase shows the opposite behavior; a scan after the first field is almost always to be preferred compared to a scan after the final field, except for PET imaging of the first head and neck patient.

Figure 7.9, 7.10 and 7.11 show the histogram of gamma values, providing more detailed insight in the distribution of gamma values compared to just the fraction of $\gamma > 1$. A large proportion of voxels show a gamma value close to zero. For similar reasons as in section 7.2.5, these voxels occur near the edge of the ROI, where the value of the PET or PGI distribution is identically zero. In all histograms, a peak is seen around γ = 0.5. This small peak is most likely caused by the voxel-to-voxel variability of 1 % (see table 7.2). Overall, a faster drop-off of gamma values is seen for the 3 % density increase for all scanning protocols and imaging modalities. More values with high gamma as well as higher values of the gamma index are detected for the 3 mm misposi-

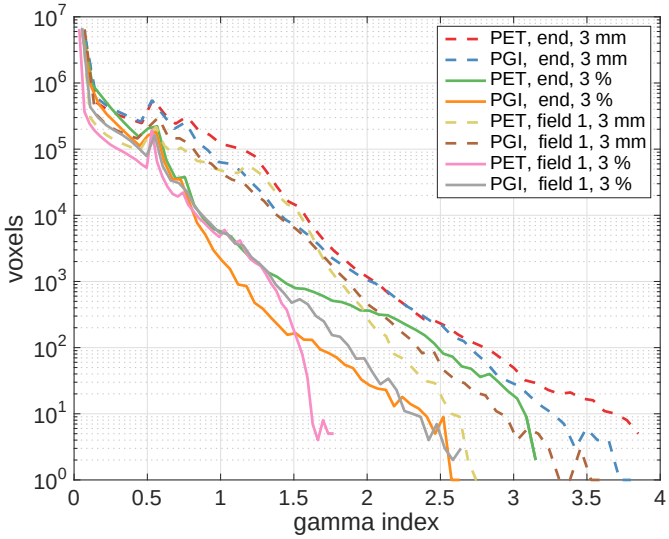

Figure 7.10: Gamma distribution histogram for the second head and neck patient using distance to agreement Δd_M = 2 mm and dose difference ΔD_M = 2 %. Solid lines indicate a 3 % density increase, dashed lines indicate a 3 mm mispositioning modification.

tioning situation. However, these high values (γ = 3 to 4) are detected in very few voxels (1 to 100 voxels).

7.4 Conclusion

We have investigated, using Monte Carlo simulations, the ability of PET and prompt gamma ray imaging to detect a compromised dose delivery using two scanning protocols: a scan after the first field and a scan after the final field. The dose deliveries were modified by a 3 % density increase as well as a 3 mm mispositioning of the isocenter. Using a 3D gamma index analysis, the sensitivity of each imaging modality and scanning protocol to the applied modification was investigated. In PET imaging, more voxels (up to a factor 4) failing the gamma criterion of 2 mm and 2 % were found than in prompt gamma ray imaging. However, this conclusion is only valid for the methods of comparison studied in this thesis. In time, technological advances specifically in the field of prompt gamma ray imaging might necessitate a re-evaluation of the performance of the prompt gamma ray imaging techniques compared to PET. When detecting a 3 mm misalignment, a scan after the final field is almost always to be preferred compared to a scan after the first field due to more voxels being irradiated with

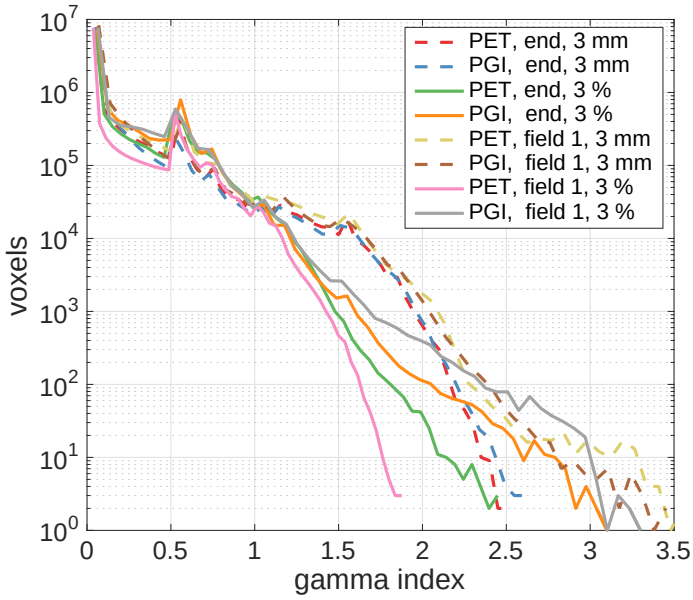

Figure 7.11: Gamma distribution histogram for the sarcoma patient using distance to agreement Δd_M = 2 mm and dose difference ΔD_M = 2 %. Solid lines indicate a 3 % density increase, dashed lines indicate a 3 mm mispositioning modification.

a higher dose. This leads to a higher overall signal to be measured. However, when detecting a 3 % density increase, a scan after the first field is in most cases to be preferred. In this case, large gamma values occur close to sharp heterogeneities in density, as well as close to the distal edge. When measuring after the final field, these features are less pronounced and more difficult to detect using the gamma index analysis since they have been irradiated again with overlapping fields of a later irradiation. In general, these simulations exemplify the complex interactions between irradiation properties, imaging modalities, scanning protocols and the applied deviations from the treatment plan. A generic optimal scanning protocol and imaging modality cannot be determined, since it depends on the type of change that needs to be detected.

Chapter 8

Summary and Outlook

8.1 Imaging of short-lived positron emitters

To verify the dose delivery of proton therapy, secondary signals need to be measured since the protons stop at the end of their range inside the patient. The most-often used techniques currently are positron emission tomography (PET) and prompt gamma ray imaging. PET is the oldest method used to verify the dose delivery from proton therapy, but its disadvantage is the delayed feedback due to the half-life of the radioactive decay. To image the most copiously produced nuclides, ^{15}O or ^{11}C, measurement times need to be of the order of their half-lives, 2 to 20 min, making instantaneous feedback impossible. Imaging of nuclides with a short half-life can overcome this obstacle. Dendooven et al. (2015) identified the short-lived nuclides that are produced in sufficient quantity to be useful for dose delivery verification of proton therapy. In this thesis, imaging of the most-promising nuclides from that study is investigated. In chapter 3, ^{12}N is used to obtain fast feedback on the dose delivery. The results of a proof-of-principle experiment of beam-on PET imaging of short-lived ^{12}N nuclei are presented. A method was developed to subtract the long-lived background signal from the ^{12}N image by introducing a beam-off period into the cyclotron beam time structure. This allows the isolation of the ^{12}N contribution. A range shift of 5 mm was measured as 6 ± 3 mm using the 1D ^{12}N profile. This measurement was performed using 2.5×10^{10} protons delivered over a 120 s period, resulting in 4.0×10^{3} detected ^{12}N counts compared to a total number of 4.0×10^{4} counts from long-lived nuclides during beam-off. A simulation shows that a large dual panel scanner that images a single spot at

the beginning of the dose delivery, can measure a 5 mm range shift with millimeter accuracy: 5.5 ± 1.1 mm for 1.64×10^8 protons and 5.2 ± 0.5 mm for 8.2×10^8 protons.

Not all events are transmitted by the data acquisition system during beam-on measurements, due to the high counting rate when the beam is on. However, the beam-on data that is transmitted is of good quality. Once the prompt events that coincide with the proton bunches are removed from the data via an anti-coincidence filter, high-quality PET energy and time distributions result. This shows that it is possible to take good PET data during beam-on by removing prompt counts using the anti-coincidence filter. However, the efficacy of this method depends on the distribution of counts relative to the RF of the accelerator, as a larger proportion of counts is removed when the bunch repetition rate is increased. When a detector is used that can handle a higher count rate than the PDPC Module TEK system and that covers a larger solid angle, an image with sufficient counts can be taken during or right after the first few spots of a clinical irradiation are delivered. As most detected counts during that time are produced by the short-lived nuclides, correcting for the longer-lived background will be less important to obtain high fidelity images that correspond to the dose delivery.

Since ^{12}N is produced on carbon nuclei, it will produce a signal in most tissue types, but the production scales with the carbon concentration of the tissue. Bone-like tissues, unlike most soft tissues, also contain calcium and phosphorus nuclei. On these nuclei, other short-lived nuclides are produced than in soft tissue, such as ^{29}P and ^{38m}K. In chapter 4, imaging of these short-lived nuclides was performed and a target shift of 10 mm was measured as 8.8 ± 1.2 mm to 9.0 ± 1.2 mm. Although the measurement time needed to image these nuclides is in the order of 1 to 4 s, meaning real-time imaging is impossible, they can be used to image the bone structures in the beam path and serve as anatomical markers.

To optimize the information that can be obtained by the dose delivery verification PET scan, several scanning and imaging protocols can be envisioned. As the effects of overall range deviations or mispositioning are more prominent for larger proton ranges and most of the dose is usually delivered by the layers with the highest proton energy, the focus should be to detect the dose delivery of the most distal energy layer. A method that has been proposed to aid the *in vivo* range verification is the delivery of a set of high energy pilot beams from the regular treatment plan (Zhong, Lu, Chen, & Shao, 2017). These pilot beams are delivered first, before the rest of the treatment plan is executed. They can be selected to cover specific areas of concern, where the proton range is most likely to be influenced by for example (i) complex density heterogeneities, (ii) where the end of the proton range is close to an organ at risk or (iii) where the influence of inter/intra-fractional motion is expected to cause a dose delivery deviation. Using these pilot beams, fast imaging of

the proton range can yield clean images unperturbed by contributions of other fields or overlapping beams. A go/no-go decision moment can be introduced in the dose delivery based on how well the image of the pilot beams matches the pre-calculated expectation of the image. This decision moment can be automated based on predefined thresholds on the measured range deviations of the pilot beams, or it can be left up to human judgement. If the range deviation contains a systematic component, the proton energy might be dynamically scaled to more closely align with the planned range.

Another option to incorporate a fast PET scan in the treatment is by extending the spot-to-spot switching time of the first few spots from the distal energy layer. An extension of the switching time to at least 22 ms will yield a decay of >75% of the ^{12}N nuclei that were produced during that spot irradiation, in the approximation that the delivery of the spot is much faster than 11 ms so that the decay of the ^{12}N nuclei during beam-on can be considered negligible. After the first couple of spots are delivered and decay of the longer-lived nuclides comprises a larger fraction of the total count rate during the beam-off measurements, the spot switching time can be reduced to its regular value to continue the rest of the irradiation without a specific modification to the time structure. This protocol treats the first few spots delivered in this way similar to the pilot beams described above.

Imaging protocols can also be optimized for the type of accelerator that is used. For continuous-wave operating accelerators (cyclotrons), measurements during beam delivery will require a detector system that can operate with a high counting rate, and will require accurate energy selection to eliminate high energy prompt gamma counts. For the synchrocyclotron accelerators from e.g. IBA and Mevion, the proton beam microstructure consists of high intensity proton pulses of 10 microsecond duration and periods of 1 to 2 ms during which no beam is delivered, meaning a lower duty cycle. IBA developed a superconducting synchrocyclotron (S2C2) with a repetition rate of 1 kHz and a pulse length of 10 microseconds (Henrotin et al., 2016). In that case, a detection system that can shut off during the proton pulses, but that can directly measure when the beam turns off might be an attractive option, as only a small number of counts will be lost during the beam-on time (Lestand et al., 2017).

8.2 Comparison of PET and prompt gamma imaging using simulation studies

A series of simulation studies was performed to investigate the high-level choices that arise when considering a dose delivery verification system. What type of signal should be measured, positron emitting nuclides or prompt gamma rays? Is there a difference with respect to the type of patient that is treated? What imaging protocol yields the best results when comparing PET and

prompt gamma ray imaging? To answer these questions, four typical proton therapy cases were simulated in detail. The first simulation study, in chapter 6, contains the irradiation of one field of a head-and-neck case. The sensitivity of positron emitting nuclides and prompt gamma rays to reflect changes in the delivered dose distribution was studied by introducing artificial inserts into the patient anatomy at the level of the treatment planning CT. Such inserts are themselves unrealistic anatomical changes, but they induce changes in the proton transport that are representative of those encountered in clinical practice when a range deviation occurs due to, e.g. the filling of a cavity. The effect of anatomical changes along the proton path on the production of PET nuclides and prompt gamma rays is shown to be complex as it depends on the combination of the irradiation parameters, the density and elemental composition of the irradiated tissue and the energy dependence of the nuclear reaction cross sections. It follows that optimization of *in vivo* dose delivery verification requires detailed investigations of a variety of clinical cases; irradiation of simple phantoms does not capture the full complexity of the problem.

For the second simulation study, chapter 7, three additional patient cases were investigated: two more head and neck cases, and a sarcoma case. The entire treatment containing all fields was simulated and different scanning protocols were implemented, a scan of 120 s directly after the first field and a scan of 120 s after the final field, both for PET. For prompt gamma ray imaging, the closest comparable protocol was used, i.e. a scan of the first field only and a scan during the entire irradiation. The dose deliveries were modified by a 3 % density increase as well as a 3 mm mispositioning of the isocenter. The sensitivities of these protocols and imaging modalities to detect the dose delivery modifications was compared using a 3D gamma index analysis. PET imaging shows more voxels (up to a factor 4) than prompt gamma ray imaging that deviate from the reference distribution based on the gamma criteria of 2 mm and 2 %. This means the PET imaging signal is more sensitive to the applied changes than the prompt gamma ray signal for these patients and imaging protocols. When detecting a misalignment, a scan after the final field is almost always to be preferred compared to a scan after the first field due to more voxels being irradiated with a higher dose, leading to a stronger signal. However, when detecting a density increase, a scan after the first field is in most cases to be preferred, as large gamma values occur close to sharp heterogeneities in density, as well as close to the distal edge. When measuring after the final field, these features are less pronounced and more difficult to detect as they have been irradiated by overlapping fields.

Based on these simulation studies of the production of prompt gamma ray and positron emitting nuclides, no imaging modality and protocol can be recommended that will produce the best information on the deviations with respect to the treatment plan for all situations. This means that the properties of the imaging equipment and the resulting images will play a pivotal role

in selecting an imaging system. Operational aspects will contribute to the overall desirability of a system, such as whether the imaging requires an extension of the time that the patient remains in the room, as this could mean a lower patient throughput. In that sense, real-time imaging such as prompt gamma ray imaging or ^{12}N PET imaging shows a significant operational advantage over regular in-situ PET imaging of the longer-lived nuclides. Cost and complexity of the imaging system and the interplay between the irradiation system and the dose delivery verification system also play a significant role.

8.3 Overview of the current state of PET and Prompt Gamma detection systems

The prompt gamma ray spectroscopy imaging technique has been developed into a full-scale clinical prototype and will soon start a clinical study of patients with brain tumors (Hueso-González et al., 2018). This prototype has been tested up to 2 nA beam current, i.e. under clinical-like conditions. A statistical precision of 1.1 mm at the 95% confidence level was achieved on the absolute proton range by aggregating measurements over a cylinder with a radius of 10 mm. Similar aggregation can also be performed for fast PET scanning or other prompt gamma ray imaging techniques to improve the signal-to-noise ratio.

The latests results from the prompt gamma ray timing experiments (Werner et al., 2019) show that the device has been tested at short irradiation times of 70 ms and clinical beam currents of 2 nA. However, the method is sensitive to the unstable relation between the phase of the accelerator RF and the delivery of the proton bunches. This effect is orders of magnitude larger than the change in signal that would correspond to a proton range deviation, so a proton bunch monitor is being developed to accurately correct for this large effect. In addition to this, the uncertainty related to the counting statistics leads to range uncertainties of 16 to 28 mm. To be able to reach millimeter precision on the range detection, spot aggregation needs to be implemented as described above as well as increasing the counting rate of the detector system, increasing the number of detectors or pixelating the detectors and thereby increasing the number of individual detector units. Further experiments using complex phantom irradiation are planned.

Prompt gamma ray imaging using a knife-edge slit camera has been used in a clinical setting for a double scattering proton therapy irradiation Priegnitz et al. (2016); Richter et al. (2016). The sensitivity of the imaging device for several beam delivery techniques was investigated by Nenoff et al. (2017), showing that applied range shifts were measured with 1 to 3 mm accuracy for IMPT and single field uniform dose (SFUD) beam delivery. Also noted by Nenoff et al. is the fact that the number of protons per spot limits

the accuracy of the shift detection, which could be solved by the clustering or aggregating of neighboring spots, leading to a compromise between lateral resolution and range detection accuracy.

Recent results from the INSIDE project in-beam PET scanner show the irradiation of PMMA targets with carbon beams (Pennazio et al., 2018). In-spill (beam-on) data is discarded due to the increase in noise it produces, and only inter-spill (beam-off) data is used to reconstruct the PET image for range verification, but using the beam-on data is being investigated. As shown in chapter 3, it is possible to obtain good quality PET data when the beam is on if the scanner can handle the high counting rate. In order to obtain enough data from the inter-spill measurements, measurement times need to be extended up to 20 s after the field is delivered. By using the shorter lived nuclei such as ^{12}N, this time might be significantly reduced. Fiorina et al. (2018) show results from the first patient monitored with the INSIDE in-beam PET scanner in December 2016. A clinical trial of the INSIDE PET system has started in 2018 at CNAO, monitoring about 20 patients who are treated with proton and carbon ions.

8.4 Routine clinical use of *in vivo* range verification

Although research has already showed the potential benefits of *in vivo* range verification techniques, it is not yet in widespread routine clinical use. Whether PET or prompt gamma ray detection systems will ever be implemented in a routine way depends inversely on the confidence one has in the treatment planning. More reliable treatment planning decreases the need for dose delivery verification. Developments to increase the quality of the treatment plan are for example DECT for more accurate tissue identification, proton radiography for direct stopping power determination and in-room imaging such as real-time MR, in-room CT or cone-beam CT. Newly developed real-time MR-guided X-ray beam systems have shown to increase treatment performance by in-situ anatomical and physiological imaging (Lagendijk et al., 2008; Raaymakers et al., 2017). The same technology applied to proton therapy is shown to be feasible by (Moteabbed, Schuemann, & Paganetti, 2014; Raaymakers, Raaijmakers, & Lagendijk, 2008; Schellhammer et al., 2018) and might yield similar or even greater benefits, as the impact of deviations from the planned dose delivery is greater for proton therapy.

The first step towards routine clinical use of *in vivo* range verification is the comparison of day-to-day results. This does not require a prediction of the measurement and thus is easier and more accurate. It will deliver a relative range deviation with respect to previous days. Predicting a measurement to obtain absolute range verification is more difficult and introduces its own uncertainties related to e.g. production cross sections.

The need for accurate range verification is increased by certain developments in protontherapy, such as hypofractionation or the use of high instantaneous beam intensities. For all cases of hypofractionation, a larger fraction of the total dose is delivered at once. An extreme case of hypofractionation is flash therapy, the delivery of an entire irradiation with an ultra-high dose rate up to 200 Gy/s on a sub-second timescale. This therapy modality can potentially result in an enhanced and wider therapeutic window, as it was shown to reduce normal tissue toxicity while remaining effective at killing tumour cells in C57BL/6J mice using dose rates of 40 Gy/s compared to the conventional dose rates of 0.03 Gy/s (Favaudon et al., 2014). Experiments are being conducted in clinical treatment rooms, delivering flash therapy to phantoms using existing accelerators and gantries (Girdhani et al., 2019; IBA, 2019). For a regular fractionated irradiation, 25 to 40 fraction of around 2 Gy each are delivered to the patient. When a dose delivery deviation is detected, the remainder of the fractions can be modified to mitigate the error that occurred. With just a few fractions or even one fraction, this is no longer possible. Delivering the entire irradiation fast and at once highlights the importance of accurate dose delivery verification, as day-to-day variations in patient positioning and other random variations do no longer average out over the course of the treatment. Using techniques such as pilot beams, deviations from the treatment plan can be identified early and modifications can be made to accurately deliver the remainder of the total dose. An additional benefit of hypofractionation is that it will increase the signal of *in vivo* verification systems. So the need for accurate verification is higher but the information that can be obtained will also be more accurate. This more accurate information could help the implementation of *in vivo* verification systems.

The PET and prompt gamma systems described in the previous section all have different properties and different circumstances will lead to success of some of them. With more accelerators adopting a beam delivery structure that produces short, intense pulses with low duty cycle, measuring while the beam is on poses a greater challenge due to the more intense instantaneous radiation and the counting rate limits of the imaging devices. This has a larger effect on prompt gamma ray imaging than on PET, as PET can use the non-prompt PET signal to measure while the beam is off in more favorable conditions. Several of the prompt gamma ray detection methods will not work well with synchrocyclotrons, as the instantaneous counting rate becomes too high. To get those systems to work, individual detector units need to be decrease in size, e.g. by pixelating the detectors, or the system needs to be placed further away to reduce its detection efficiency. More detectors are then needed to retain the same information quality, thereby increasing the total system cost and increasing the difficulty to integrate the system in the treatment room. Using PET imaging of short-lived nuclei such as ^{12}N, sub-second feedback is possible by measuring when the beam is off, nearly unaffected by the high counting rate

during beam-on. Aggregating counts of neighboring spots to increase counting statistics will improve the image quality for this short-lived PET method as well as for the prompt gamma ray imaging devices described above. Based on radiation hardness experiments from Diblen et al. (2017), SiPM-based detector systems will suffer from performance degradation due to increased dark count rate after a few weeks of operational use, so a PMT-based system is to be preferred for reliable performance. A large surface area PET detector system with the ability to turn off detection during beam delivery should be able to operate in clinical conditions and provide fast feedback on the dose delivery via ^{12}N imaging. Further research using such a device is currently being conducted at KVI-CART.

Another advantage of PET is the fact that the basic technology is not developed solely for *in vivo* range verification. PET scanners are continuously improved independent from their application in the field of proton therapy. They are developed for the larger market of nuclear medicine, but also in the field of high-energy physics an effort is ongoing in order to increase the radiation hardness of SiPMs, which will make them better suited for use in a proton therapy facility. The radiotherapy community can profit from these PET scanner advancements in other fields. It is not clear that this will be a deciding factor in determining which detector system will be implemented by proton-therapy facilities, but large part of their success will be determined by the ease and cost of implementation, research and use.

List of publications

Buitenhuis H J T, Diblen F, Brzezinski K W, Brandenburg S and Dendooven P 2017 *Physics in Medicine and Biology* Beam-on imaging of short-lived positron emitters during proton therapy 62(12), 4654-4672 https://doi.org/10.1088/1361-6560/aa6b8c

Dendooven P, Buitenhuis H J T, Diblen F, Heeres P N, Biegun A K, Fiedler F, Van Goethem M-J, Van der Graaf E R and Brandenburg S 2015 *Physics in Medicine and Biology* Short-lived positron emitters in beam-on PET imaging during proton therapy 60(23), 8923-8947 https://doi.org/10.1088/0031-9155/60/23/8923

Dendooven P, Buitenhuis H J T, Diblen F, Heeres P N, Biegun A K, Fiedler F, Van Goethem M-J, Van der Graaf E R and Brandenburg S 2019 *Physics in Medicine and Biology* Corrigendum: Short-lived positron emitters in beam-on PET imaging during proton therapy (2015 Phys. Med. Biol. 60 8923), 64(12) 129501 https://doi.org/10.1088/1361-6560/ab23d7

Diblen F, Buitenhuis T, Solf T, Rodrigues P, Van der Graaf E, Van Goethem M-J, Brandenburg S and Dendooven P 2017 *IEEE Transactions on Nuclear Science* Radiation hardness of dSiPM sensors in a proton therapy radiation environment 64(7), 1891-1896 https://doi.org/10.1109/TNS.2017.2705522

Us D, Brzezinski K, Buitenhuis T, Dendooven P and Ruotsalainen U 2018 *IEEE Transactions on Radiation and Plasma Medical Sciences* Evaluation of Median Root Prior for Robust In-Beam PET Reconstruction 5(2) 490-498 https://doi.org/10.1109/TRPMS.2018.2854231

Nederlandse samenvatting

Kanker is een van de belangrijkste doodsoorzaken in Nederland. In 2017 droegen alle vormen van kanker bij aan 47,000 van de 150,000 geregistreerde doodsoorzaken (Centraal Bureau voor de Statistiek, 2017). Er zijn verschillende manieren om kanker te behandelen. De meest voorkomende behandelmethoden zijn radiotherapie, chirurgie, chemotherapie, doelgerichte therapie, hormoontherapie en immunotherapie. Geregeld worden verschillende methoden gecombineerd om de effectiviteit van de behandeling te vergroten. Patiënten kunnen bijvoorbeeld na de operatie radiotherapie krijgen om alle achtergebleven sporen van kankercellen te verwijderen.

Radiotherapie gebruikt ioniserende straling om tumorcellen te doden door hun DNA te beschadigen. Deze straling kan intern (brachytherapie) of extern toegediend worden. Voor brachytherapie worden radioactieve bronnen geïmplanteerd in en rond de tumor. Deze bronnen geven hun dosis daardoor direct af op de juiste locatie. Voor deze methode moet de tumor zich echter op een relatief gemakkelijk toegankelijke locatie bevinden. Bij sommige patiënten wordt een radioactieve substantie geinjecteerd die zich ophoopt in de tumor en zo lokaal de meeste dosis afgeeft. Vaker wordt de straling toegediend met behulp van een bron buiten het lichaam. In het verleden werden radioactieve bronnen zoals ^{60}Co gebruikt om MeV-gammastralen te leveren. Tegenwoordig wordt in de meeste radiotherapiefaciliteiten een lineaire versneller gebruikt om MeV-elektronenstralen te produceren. Deze elektronen worden gestopt in een wolfraamabsorbeerder om MeV-röntgenstralen te genereren, die diep in het lichaam doordringen.

Andere deeltjes kunnen ook worden gebruikt, zoals protonen of zelfs zwaardere nucliden. Het versnellen van deze deeltjes tot klinisch bruikbare energieën vereist grote deeltjesversnellers. Al in 1946 schreef Robert R. Wilson over hoe protonen met een energie in de orde van 100 MeV zeer interes-

sant zijn voor radiotherapie (Wilson, 1946). Momenteel bestaan er 92 centra voor hadrontherapie over de hele wereld (PTCOG, 2019). Patiënten worden dagelijks behandeld met protonen, en in mindere mate met koolstofkernen. Tot 2017 zijn ongeveer 170.000 patiënten wereldwijd behandeld met protonen en koolstofkernen (PTCOG, 2019). In Nederland zijn recent verschillende centra voor protonentherapie gebouwd. Het Universitair Medisch Centrum Groningen heeft in januari 2018 een eerste patiënt behandeld in hun nieuwe protonentherapiefaciliteit (UMCG, 2018). HollandPTC begon met behandelingen in augustus 2018 en ZON-PTC in Maastricht begon met behandelingen in februari 2019.

Protonenherapie wordt gekenmerkt door mogelijkheden voor het toedienen van verbeterde gelokaliseerde dosis in vergelijking met fotonentherapie. Deze eigenschap kan worden benut om bijkomende schade aan gezonde weefsels rondom de tumor te verminderen, of om de dosis in de tumor te verhogen. Het eindige protonenbereik en de hoge dosis in de Bragg-piek veroorzaken echter een verhoogde gevoeligheid voor afwijkingen van de geplande behandeling in vergelijking met fotonen. Daarom is een *in vivo*-methode voor het verifiëren van de dosisafgifte van cruciaal belang om het klinische voordeel van de fysisch superieure dosisverdelingen volledig te benutten.

Omdat de protonen in het lichaam van de patiënt worden gestopt, vereist *in vivo* verificatie van de dosisafgifte beeldvorming van secundaire straling geïnduceerd door protoninteracties in het menselijk lichaam. Hoogenergetische fotonen worden meestal voor dit doel gebruikt, omdat ze gunstige productiedoorsneden hebben en ze uit het lichaam van de patiënt kunnen ontsnappen. Er zijn twee soorten hoogenergetische fotonen beschikbaar die volgen uit kernreacties geïnduceerd door de protonen: positron-annihilatie-fotonen (511 keV) na het verval van kernen die positronen uitzenden en prompte gammastralen die worden uitgezonden op een tijdschaal van sub-nanoseconden in het verval van geëxciteerde kernen.

Dit proefschrift is onderverdeeld in twee delen. Het eerste deel gaat over hoe snelle informatie over de dosisafgifte kan worden verkregen met behulp van positronemissietomografie (PET). Omdat een typische PET-scan minstens een paar minuten duurt om voldoende tellingen te verkrijgen voor verificatie vanwege de halfwaardetijden van 2 tot 20 minuten is onmiddellijke feedback niet mogelijk. Dit heeft geleid tot de ontwikkeling van beeldvormingstechnieken gebaseerd op prompte gammastraling, die in principe real-time feedback over de dosisafgifte kunnen geven. Wanneer echter een PET scan tijdens de bestraling wordt genomen, zal ook het verval van nucliden met een kortere levensduur zoals ^{12}N met een halfwaardetijd van 11 ms bijdragen aan het beeld. In het eerste deel van dit proefschrift wordt beeldvorming van deze kortlevende nucliden bestudeerd om het gebruik van PET voor real-time dosisafgifte-verificatie mogelijk te maken.

In het tweede deel worden de kwalitatieve verschillen tussen PET

en prompte gammastraling onderzocht. Er is een gedetailleerd Monte Carlo simulatie framework ontwikkeld om de verschillen in PET en prompte gamma verdelingen te bestuderen met behulp van echte patiëntinformatie.

Beeldvorming van kortlevende positron emitters

Om de dosisafgifte van protonentherapie te verifiëren, moeten secundaire signalen worden gemeten, aangezien de protonen stoppen aan het einde van hun bereik in de patiënt. De meest gebruikte technieken zijn momenteel positronemissietomografie (PET) en prompte gammastraling. PET is de oudste methode die wordt gebruikt om de dosisafgifte van protonentherapie te verifiëren, maar het nadeel is de vertraagde feedback vanwege de halfwaardetijd van het radioactieve verval. Om de meest overvloedig geproduceerde nucliden af te beelden, ^{15}O of ^{11}C, moeten meettijden van de PET scan in de orde van hun halfwaardetijd zijn, 2 tot 20 minuten, waardoor real-time feedback onmogelijk is. Beeldvorming van nucliden met een korte halfwaardetijd kan dit obstakel overkomen. Dendooven et al. (2015) identificeerde de kortlevende nucliden die in voldoende hoeveelheid worden geproduceerd om bruikbaar te zijn voor verificatie van dosisafgifte van protonentherapie. In dit proefschrift wordt de beeldvorming van de meest veelbelovende nucliden uit die studie onderzocht. In hoofdstuk 3 wordt ^{12}N gebruikt om snelle feedback over de dosisafgifte te verkrijgen. De resultaten van een proof-of-principle experiment van beam-on PET imaging van kortlevende ^{12}N-kernen worden gepresenteerd. Een methode werd ontwikkeld om het langlevende achtergrondsignaal af te trekken van het ^{12}N-beeld door een beam-off periode in de cyclotron-bundeltijdstructuur in te voeren. Hiermee kan de ^{12}N-bijdrage aan het beeld worden geïsoleerd. Een verandering van 5 mm in het bereik van de protonen werd gemeten als 6 ± 3 mm met behulp van het 1D ^{12}N-profiel. Deze meting werd uitgevoerd met 2.5×10^{10} protonen afgeleverd over een 120 s periode, resulterend in 4.0×10^{3} gedetecteerde ^{12}N tellingen vergeleken met een totaal aantal 4.0×10^{4} tellingen van langlevende nucliden tijdens de beam-off periode. Een simulatie laat zien dat een grote scanner met twee panelen die een enkele spot afbeeldt vanaf het begin van de dosisafgifte een verschuiving van 5 mm met millimeternauwkeurigheid kan meten: 5.5 ± 1.1 mm voor 1.64×10^{8} protonen en 5.2 ± 0.5 mm voor 8.2×10^{8} protonen.

Niet alle tellingen worden door het data-acquisitiesysteem tijdens beam-on-metingen verzonden, vanwege de hoge telsnelheid wanneer de bundel is ingeschakeld. De tellingen die doorkomen zijn echter van goede kwaliteit. Zodra de prompte tellingen die samenvallen met de proton bunches uit de data worden verwijderd via een anti-coincidentiefilter, resulteert dit in hoogwaardige PET energie- en tijdspectra. Dit laat zien dat het mogelijk is om goede PET-data te verkrijgen tijdens het beam-on door prompte tellingen te ver-

wijderen met behulp van het anti-coincidentiefilter. De effectiviteit van deze methode hangt echter af van de verdeling van tellingen ten opzichte van de RF van de versneller, omdat een groter deel van tellingen wordt verwijderd wanneer de herhalingsfrequentie van de proton bunches wordt verhoogd. Wanneer een detector wordt gebruikt die een hogere telsnelheid aankan dan het PDPC Module TEK-systeem en die een grotere ruimtehoek bestrijkt, kan een beeld met voldoende tellingen worden verkregen tijdens of direct nadat de eerste paar spots van een bestraling zijn afgeleverd. Aangezien de meeste gedetecteerde tellingen gedurende die tijd worden geproduceerd door de kortlevende nucliden, zal het corrigeren voor de langer levende achtergrond minder belangrijk zijn om goede beelden te verkrijgen die overeenkomen met de dosisafgifte.

Omdat ^{12}N wordt geproduceerd op koolstofkernen zal het een signaal produceren in de meeste weefseltypen, maar de productie schaalt met de koolstofconcentratie van het weefsel. Botachtige weefsels, in tegenstelling tot de meeste weke delen, bevatten ook calcium- en fosforkernen. Op deze kernen worden andere kortlevende nucliden geproduceerd dan in weke delen, zoals ^{29}P en ^{38m}K. In hoofdstuk 4 werd beeldvorming van deze kortlevende nucliden uitgevoerd en werd een verschuiving van 10 mm gemeten als 8,8 ± 1,2 mm tot 9,0 ± 1,2 mm. Hoewel de meettijd die nodig is om deze nucliden af te beelden in de orde van 1 tot 4 seconden is, wat betekent dat real-time beeldvorming onmogelijk is, kunnen ze worden gebruikt als anatomische markers en om de botstructuren in het bundelpad af te beelden.

Vergelijking van PET en prompte gamma-beeldvorming met behulp van simulatiestudies

Een reeks simulatiestudies werd uitgevoerd om de keuzes te onderzoeken die zich voordoen bij het overwegen van een verificatiesysteem voor dosisafgifte. Welk type signaal moet worden gemeten, PET of prompte gammastralen? Is er een verschil met het type patiënt dat wordt behandeld? Welk beeldvormingsprotocol geeft de beste resultaten bij het vergelijken van PET en prompte gammastraling? Om deze vragen te beantwoorden, werden vier typische protonentherapie casussen in detail gesimuleerd. De eerste simulatie studie, in hoofdstuk 6, bevat de bestraling van één veld van een hoofd-hals patiënt. De gevoeligheid van PET en prompte gammastraling om veranderingen in de afgegeven dosisverdeling te detecteren werd bestudeerd door kunstmatige inserts in de anatomie van de patiënt te introduceren op het niveau van de planning CT. Dergelijke inserts zijn zelf onrealistische anatomische veranderingen, maar ze induceren veranderingen in het protontransport die representatief zijn voor de veranderingen die worden aangetroffen in de klinische praktijk wanneer een range-afwijking optreedt als gevolg van, b.v. het vullen van een anatomische holte. Het effect van anatomische veranderingen in het protonenpad op de

productie van PET-nucliden en prompte gammastraling is complex omdat het afhankelijk is van de combinatie van de bestralingsparameters, de dichtheid en elementaire samenstelling van het bestraalde weefsel en de energieafhankelijkheid van de nucleaire productiedoorsneden. Hieruit volgt dat optimalisatie van *in vivo* verificatie van dosisafgifte gedetailleerd onderzoek van een aantal klinische casussen vereist; bestralingen op eenvoudige fantomen geven niet genoeg inzicht in de volledige complexiteit van het probleem.

Voor het tweede simulatieonderzoek, hoofdstuk 7, werden drie extra patiëntcasussen onderzocht: twee additionele hoofd-hals patiënten en een sarcoom patiënt. De gehele behandeling met alle velden werd gesimuleerd en verschillende scanprotocollen werden geïmplementeerd: een scan van 120 s direct na het eerste veld en een scan van 120 s na het laatste veld, beide voor PET. Voor prompte gammastraling werd het meest vergelijkbare protocol gebruikt, d.w.z. alleen een scan van het eerste veld en een scan tijdens de gehele bestraling. De dosisafgiften werden gewijzigd door een 3 % dichtheidstoename evenals een 3 mm verplaatsing van het isocentrum. De gevoeligheden van deze protocollen en beeldvormingsmodaliteiten om de dosisafgifteveranderingen te detecteren werden vergeleken met behulp van een 3D gamma-indexanalyse. PET-beeldvorming toont meer voxels (tot een factor 4) dan prompte gammastraling die afwijken van de referentieverdeling op basis van de gamma-criteria van 2 mm en 2 %. Dit betekent dat het PET-signaal gevoeliger is voor de toegepaste veranderingen dan het prompte gammastralingssignaal voor deze patiënten en beeldvormingsprotocollen. Bij het detecteren van een verkeerde uitlijning van het isocentrum verdient een scan na het laatste veld bijna altijd de voorkeur in vergelijking met een scan na het eerste veld, omdat meer voxels worden bestraald met een hogere dosis, wat leidt tot een sterker signaal. Wanneer echter een toename van de dichtheid wordt gedetecteerd, verdient een scan na het eerste veld in de meeste gevallen de voorkeur, omdat grote gammawaarden voorkomen in de buurt van scherpe heterogeniteiten in dichtheid, evenals in de buurt van de distale rand. Bij het meten na het laatste veld zijn deze kenmerken minder uitgesproken en moeilijker te detecteren omdat ze zijn bestraald door overlappende velden.

Op basis van deze simulatiestudies van de productie van prompte gammastraling en positron-emitterende nucliden, kunnen geen beeldvormingsmodaliteit en protocol worden aanbevolen dat voor alle situaties de beste informatie oplevert over de afwijkingen met betrekking tot het behandelplan. Dit betekent dat de eigenschappen van de beeldvormingsapparatuur en de resulterende beelden een belangrijke rol zullen spelen bij het selecteren van een beeldvormingssysteem. Operationele aspecten zullen bijdragen aan de algehele wenselijkheid van een systeem, zoals of de beeldvorming een verlenging van de tijd vereist dat de patiënt in de kamer blijft, omdat dit een langere doorvoertijd van de patiënt kan betekenen. In die zin biedt realtime beeldvorming van prompte gammastraling of ^{12}N PET een aanzienlijk operationeel voordeel ten

opzichte van reguliere in situ PET beeldvorming van de langer levende nucliden. Kosten en complexiteit van het beeldvormingssysteem en de wisselwerking tussen het bestralingssysteem en het verificatiesysteem voor dosisafgifte spelen ook een belangrijke rol.

Dankwoord

Wetenschap is vaak teamwork, en ook dit proefschrift zou niet tot stand zijn gekomen zonder de bijdrage van velen. Ik wil graag iedereen van harte bedanken.

Beste Peter, beste Sytze, bedankt voor de mogelijkheid om mijn promotieonderzoek in de Medische Fysica groep van het KVI-CART te kunnen doen. De afgelopen jaren hebben we veel overlegd en gediscussieerd. Bedankt voor alle begeleiding, de waardevolle suggesties, jullie benaderbaarheid, geduld en vertrouwen in mij.

Dear members of the assessment committee, thank you for your commitment to reading my thesis. You gave several suggestions for improvements to the manuscript, which I have gladly embraced.

Uiteraard wil ik ook alle collega's uit de Medische Fysica groep bedanken. Ik heb enorm veel van jullie kunnen leren. Dank voor alle hulp, voor het delen van jullie theoretische en praktische kennis, maar bovenal voor de gezelligheid op het lab.

Beste klinisch fysici van de afdeling UMCG radiotherapie, bedankt voor jullie support in het ontwikkelen van een realistisch simulatieframework. Jullie hebben de calibratie data, scans en behandelplannen aangeleverd die ten grondslag liggen aan de meeste van mijn simulaties.

Beste medewerkers van het AGOR versnellerbedrijf en de mechanische werkplaats, bedankt voor alle praktische hulp bij het voorbereiden van de opstellingen en het uitvoeren van de vele nachtelijke experimenten.

Dear IBA group and Skandionkliniken in Uppsala, thank you for allowing us to perform some PET measurements in your experimental room using the clinical accelerator and beam line. Even though unforeseen circumstances did not allow us to perform usable measurements, the experience was very valuable.

Dear Oncology Solutions department of Philips Research, many thanks for supervising my MSc internship in this field and the fruitful collaborations and experiments afterwards.

Vrienden en familie, bedankt voor jullie support tijdens het schrijven van dit proefschrift. Zonder jullie betrokkenheid en de broodnodige afleiding waren de afgelopen jaren een stuk minder aangenaam geweest.

Tot slot, Xandra, je hebt me altijd gesteund, zeker in de moeilijke afrondende fase. Ik had het niet kunnen doen zonder jou.

Bibliography

Agostinelli, S., Allison, J., Amako, K., Apostolakis, J., Araujo, H., Arce, P., … Zschiesche, D. (2003). Geant4—a simulation toolkit. *Nuclear Instruments and Methods in Physics Research Section A: Accelerators, Spectrometers, Detectors and Associated Equipment*, *506*(3), 250-303. https://doi.org/10.1016/S0168-9002(03)01368-8
(p. 65).

Ammar, C., Frey, K., Bauer, J., Melzig, C., Chiblak, S., Hildebrandt, M., … Parodi, K. (2014). Comparing the biological washout of β^+ -activity induced in mice brain after ^{12}C-ion and proton irradiation. *Physics in Medicine and Biology*, *59*(23), 7229. Retrieved from `http://stacks.iop.org/0031-9155/59/i=23/a=7229`
(pp. 75, 76, 76, 76, 76, 78).

Assmann, W., Kellnberger, S., Reinhardt, S., Lehrack, S., Edlich, A., Thirolf, P. G., … Parodi, K. (2015). Ionoacoustic characterization of the proton Bragg peak with submillimeter accuracy. *Medical Physics*, *42*(2), 567-574. https://doi.org/10.1118/1.4905047
(pp. 9, 21).

Bazalova, M., Carrier, J.-F., Beaulieu, L., & Verhaegen, F. (2008). Dual-energy CT-based material extraction for tissue segmentation in Monte Carlo dose calculations. *Physics in Medicine and Biology*, *53*(9), 2439. Retrieved from `http://stacks.iop.org/0031-9155/53/i=9/a=015`
(p. 8).

Berger, M., Coursey, J., Zucker, M., & Chang, J. (2005). *ESTAR, PSTAR, and ASTAR: Computer programs for calculating stopping-power and range tables for electrons, protons, and helium ions.* Retrieved from `http://physics.nist.gov/Star`
(p. 29).

Bisogni, M. G., Attili, A., Battistoni, G., Belcari, N., Camarlinghi, N., Cerello, P., … Wheadon, R. (2017, 01). INSIDE in-beam positron emission tomography system for particle range monitoring in hadrontherapy. *Journal of medical imaging (Bellingham, Wash.)*, *4*(1), 011005; 011005-011005. https://doi.org/10.1117/1.JMI.4.1.011005
(p. 14).

Boda-Heggemann, J., Knopf, A.-C., Simeonova-Chergou, A., Wertz, H., Stieler, F., Jahnke, A., … Lohr, F. (2016, 2018/12/03). Deep inspiration breath hold-based radiation therapy: A clinical review. *International Journal of Radiation Oncology, Biology, Physics*, *94*(3), 478-492. https://doi.org/10.1016/j.ijrobp.2015.11.049
(p. 7).

Böhlen, T. T., Cerutti, F., Dosanjh, M., Ferrari, A., Gudowska, I., Mairani, A., & Quesada, J. M. (2010). Benchmarking nuclear models of FLUKA and GEANT4 for carbon ion therapy. *Physics in Medicine and Biology*, *55*(19), 5833. Retrieved from http://stacks.iop.org/0031-9155/55/i=19/a=014
(p. 70).

Buitenhuis, H. J. T., Diblen, F., Brzezinski, K. W., Brandenburg, S., & Dendooven, P. (2017). Beam-on imaging of short-lived positron emitters during proton therapy. *Physics in Medicine and Biology*, *62*(12), 4654. Retrieved from http://stacks.iop.org/0031-9155/62/i=12/a=4654
(p. 81).

Cambraia Lopes, P., Bauer, J., Salomon, A., Rinaldi, I., Tabacchini, V., Tessonnier, T., … Schaart, D. R. (2016). First in situ TOF-PET study using digital photon counters for proton range verification. *Physics in Medicine and Biology*, *61*(16), 6203. Retrieved from http://stacks.iop.org/0031-9155/61/i=16/a=6203
(pp. 31, 31, 81).

Centraal Bureau voor de Statistiek. (2017). *Statline; overledenen; doodsoorzaak, kwartaal en jaar overlijden.*
(pp. 1, 123).

Compaq, Hewlett-Packard, Intel, Lucent, Microsoft, NEC, & Philips. (2000, April). Universal serial bus specification revision 2.0 [Computer software manual]. Retrieved from http://www.usb.org/developers/docs/usb20_docs/
(p. 31).

Cormack, A. M. (1963, 2018/11/23). Representation of a function by its line integrals, with some radiological applications. *Journal of Applied Physics*, *34*(9), 2722-2727. https://doi.org/10.1063/1.1729798
(p. 9).

Crespo, P., Barthel, T., Frais-Kolbl, H., Griesmayer, E., Heidel, K., Parodi, K., … Enghardt, W. (2005, Aug). Suppression of random coincidences

during in-beam PET measurements at ion beam radiotherapy facilities. *IEEE Transactions on Nuclear Science*, *52*(4), 980-987.
(p. 81).

Crespo, P., Shakirin, G., & Enghardt, W. (2006). On the detector arrangement for in-beam PET for hadron therapy monitoring. *Physics in Medicine and Biology*, *51*(9), 2143. Retrieved from http://stacks.iop.org/0031-9155/51/i=9/a=002
(p. 14).

Dendooven, P., Buitenhuis, H. J. T., Diblen, F., Heeres, P. N., Biegun, A. K., Fiedler, F., … Brandenburg, S. (2015). Short-lived positron emitters in beam-on PET imaging during proton therapy. *Physics in Medicine and Biology*, *60*(23), 8923. Retrieved from http://stacks.iop.org/0031-9155/60/i=23/a=8923
(pp. 15, 16, 27, 28, 35, 36, 37, 47, 51, 113, 125).

Dendooven, P., Buitenhuis, H. J. T., Diblen, F., Heeres, P. N., Biegun, A. K., Fiedler, F., … Brandenburg, S. (2019). Corrigendum: Short-lived positron emitters in beam-on PET imaging during proton therapy (2015 Phys. Med. Biol. 60 8923). *Physics in Medicine and Biology*, *64*(12), 129501. https://doi.org/10.1088/1361-6560/ab23d7
(pp. 16, 36, 51, 53, 56).

Diblen, F., Buitenhuis, T., Solf, T., Rodrigues, P., van der Graaf, E., van Goethem, M., … Dendooven, P. (2017). Radiation hardness of dSiPM sensors in a proton therapy radiation environment. *IEEE Transactions on Nuclear Science*, *64*(7), 1891-1896.
(pp. 14, 15, 120).

Enghardt, W., Crespo, P., Fiedler, F., Hinz, R., Parodi, K., Pawelke, J., & Pönisch, F. (2004). Charged hadron tumour therapy monitoring by means of PET. *Nuclear Instruments and Methods in Physics Research Section A: Accelerators, Spectrometers, Detectors and Associated Equipment*, *525*(1), 284-288. (Proceedings of the International Conference on Imaging Techniques in Subatomic Physics, Astrophysics, Medicine, Biology and Industry) https://doi.org/10.1016/j.nima.2004.03.128
(pp. 15, 81).

Enghardt, W., Debus, J., Haberer, T., Hasch, B. G., Hinz, R., Jäkel, O., … Pawelke, J. (1999, Jun 01). The application of PET to quality assurance of heavy-ion tumor therapy. *Strahlentherapie und Onkologie*, *175*(2), 33-36. https://doi.org/10.1007/BF03038884
(p. 14).

Everett, D. B., Fleming, J. S., Todd, R. W., & Nightingale, J. M. (1977). Gamma-radiation imaging system based on the compton effect. *Proceedings of the Institution of Electrical Engineers*, *124*(11), 995.
(p. 18).

Falbo, L., Burato, G., Primadei, G., & Paoluzzi, M. (2011). CNAO RF

system: Hardware description. *WEPS006*.
(p. 22).

Favaudon, V., Caplier, L., Monceau, V., Pouzoulet, F., Sayarath, M., Fouillade, C., … Vozenin, M.-C. (2014, 07). Ultrahigh dose-rate flash irradiation increases the differential response between normal and tumor tissue in mice. *Science Translational Medicine*, *6*(245), 245ra93. https://doi.org/10.1126/scitranslmed.3008973
(p. 119).

Ferrero, V., Fiorina, E., Morrocchi, M., Pennazio, F., Baroni, G., Battistoni, G., … Bisogni, M. G. (2018). Online proton therapy monitoring: clinical test of a silicon-photodetector-based in-beam PET. *Scientific Reports*, *8*(1), 4100. https://doi.org/10.1038/s41598-018-22325-6
(p. 14).

Fiedler, F., Kunath, D., Priegnitz, M., & Enghardt, W. (2012). Ion beam therapy: Fundamentals, technology, clinical applications. In U. Linz (Ed.), (pp. 527–543). Berlin, Heidelberg: Springer. https://doi.org/10.1007/978-3-642-21414-1_31
(p. 9).

Fiorina, E., Ferrero, V., Pennazio, F., Baroni, G., Battistoni, G., Belcari, N., … Bisogni, M. G. (2018, 2018/06/26). Monte Carlo simulation tool for online treatment monitoring in hadrontherapy with in-beam PET: A patient study. *Physica Medica: European Journal of Medical Physics*. https://doi.org/10.1016/j.ejmp.2018.05.002
(p. 118).

Frach, T., Prescher, G., & Degenhardt, C. (2010). The digital silicon photomultiplier—system architecture and performance evaluation. *IEEE NSS-MIC Conf. Record*, 1722.
(p. 30).

Girdhani, S., Abel, E., Katsis, A., Rodriquez, A., Senapati, S., KuVillanueva, A., … Parry, R. (2019). Flash: A novel paradigm changing tumor irradiation platform that enhances therapeutic ratio by reducing normal tissue toxicity and activating immune pathways. In *Aacr annual meeting*.
(p. 119).

Golnik, C., Hueso-González, F., Müller, A., Dendooven, P., Enghardt, W., Fiedler, F., … Pausch, G. (2014). Range assessment in particle therapy based on prompt γ-ray timing measurements. *Physics in Medicine and Biology*, *59*(18), 5399. Retrieved from `http://stacks.iop.org/0031-9155/59/i=18/a=5399`
(pp. 20, 46).

Grevillot, L., Frisson, T., Zahra, N., Bertrand, D., Stichelbaut, F., Freud, N., & Sarrut, D. (2010). Optimization of GEANT4 settings for proton pencil beam scanning simulations using GATE. *Nuclear Instruments and Methods in Physics Research Section B:*

Beam Interactions with Materials and Atoms, *268*(20), 3295-3305. https://doi.org/10.1016/j.nimb.2010.07.011
(p. 74).

Grogg, K., Alpert, N. M., Zhu, X., Min, C. H., Testa, M., Winey, B., … El Fakhri, G. (2015, 10). Mapping ^{15}O production rate for proton therapy verification. *International Journal of Radiation Oncology, Biology, Physics*, *92*(2), 453-459. https://doi.org/10.1016/j.ijrobp.2015.01.023
(pp. 75, 78).

Haemisch, Y., Frach, T., Degenhardt, C., & Thon, A. (2012). Fully digital arrays of silicon photomultipliers (dSiPM) – a scalable alternative to vacuum photomultiplier tubes (PMT). *Physics Procedia*, *37*, 1564-1560. Retrieved from https://doi.org/10.1016/j.phpro.2012.03.749
(p. 30, 30, 30).

Hayakawa, Y., Tada, J., Arai, N., Hosono, K., Sato, M., Wagai, T., … Tsujii, H. (1995). Acoustic pulse generated in a patient during treatment by pulsed proton radiation beam. *Radiation Oncology Investigations*, *3*(1), 42-45. https://doi.org/10.1002/roi.2970030107
(p. 9).

Helmbrecht, S., Enghardt, W., Fiedler, F., Iltzsche, M., Pausch, G., Tintori, C., & Kormoll, T. (2016). In-beam PET at clinical proton beams with pile-up rejection. *Zeitschrift für Medizinische Physik*, *27*(3), 202-217. https://doi.org/10.1016/j.zemedi.2016.07.003
(p. 44).

Helmbrecht, S., Enghardt, W., Parodi, K., Didinger, B., Debus, J., Kunath, D., … Fiedler, F. (2013, Sep). Analysis of metabolic washout of positron emitters produced during carbon ion head and neck radiotherapy. *Med Phys*, *40*(9), 091918.
(pp. 74, 75, 75, 78).

Henrotin, S., Abs, M., Forton, E., Jongen, Y., Kleeven, W., de Walle, J. V., & Verbruggen, P. (2016). *Commissioning and testing of the first IBA S2C2* (No. TUP07). Cyclotron Technology.
(p. 115).

Hickling, S., Xiang, L., Jones, K. C., Parodi, K., Assmann, W., Avery, S., … El Naqa, I. (2018). Ionizing radiation-induced acoustics for radiotherapy and diagnostic radiology applications. *Medical Physics*, *45*(7), e707-e721. https://doi.org/10.1002/mp.12929
(p. 21).

Hirano, Y., Kinouchi, S., Ikoma, Y., Yoshida, E., Wakizaka, H., Ito, H., & Yamaya, T. (2013). Compartmental analysis of washout effect in rat brain: in-beam OpenPET measurement using a ^{11}C beam. *Physics in Medicine and Biology*, *58*(23), 8281. Retrieved from http://stacks.iop.org/0031-9155/58/i=23/a=8281
(p. 75).

Hsi, W. C., Indelicato, D. J., Vargas, C., Duvvuri, S., Li, Z., & Palta, J. (2009, 2018/12/04). In vivo verification of proton beam path by using post-treatment PET/CT imaging. *Medical Physics*, *36*(9Part1), 4136-4146. https://doi.org/10.1118/1.3193677
(p. 51).

Hueso-González, F., Enghardt, W., Fiedler, F., Golnik, C., Janssens, G., Petzoldt, J., … Pausch, G. (2015). First test of the prompt gamma ray timing method with heterogeneous targets at a clinical proton therapy facility. *Physics in Medicine and Biology*, *60*(16), 6247. Retrieved from http://stacks.iop.org/0031-9155/60/i=16/a=6247
(p. 20).

Hueso-González, F., Rabe, M., Ruggieri, T. A., Bortfeld, T., & Verburg, J. M. (2018). A full-scale clinical prototype for proton range verification using prompt gamma-ray spectroscopy. *Physics in Medicine and Biology*, *63*(18), 185019. Retrieved from http://stacks.iop.org/0031-9155/63/i=18/a=185019
(pp. 19, 102, 117).

Hünemohr, N., Krauss, B., Tremmel, C., Ackermann, B., Jäkel, O., & Greilich, S. (2014). Experimental verification of ion stopping power prediction from dual energy CT data in tissue surrogates. *Physics in Medicine and Biology*, *59*(1), 83. Retrieved from http://stacks.iop.org/0031-9155/59/i=1/a=83
(p. 8).

IBA. (2019, March). *Flash irradiation delivered in a clinical treatment room.* Retrieved from [07-07-2019]https://iba-worldwide.com/sites/protontherapy/files/media_document/20190308_flash_groningen_final.pdf
(p. 119).

Jan, S., Santin, G., Strul, D., Staelens, S., Assié, K., Autret, D., … Morel, C. (2004). GATE: a simulation toolkit for PET and SPECT. *Physics in Medicine and Biology*, *49*(19), 4543. Retrieved from http://stacks.iop.org/0031-9155/49/i=19/a=007
(pp. 36, 65).

Johnson, R. P. (2018). Review of medical radiography and tomography with proton beams. *Reports on Progress in Physics*, *81*(1), 016701. Retrieved from http://stacks.iop.org/0034-4885/81/i=1/a=016701
(p. 9).

Jones, K. C., Nie, W., Chu, J. C. H., Turian, J. V., Kassaee, A., Sehgal, C. M., & Avery, S. (2018). Acoustic-based proton range verification in heterogeneous tissue: simulation studies. *Physics in Medicine and Biology*, *63*(2), 025018. Retrieved from http://stacks.iop.org/0031-9155/63/i=2/a=025018
(p. 21).

Jones, K. C., Seghal, C. M., & Avery, S. (2016). How proton pulse characteristics influence protoacoustic determination of proton-beam range: simulation studies. *Physics in Medicine and Biology*, *61*(6), 2213. Retrieved from http://stacks.iop.org/0031-9155/61/i=6/a=2213
(p. 21).

Jones, K. C., Vander Stappen, F., Bawiec, C. R., Janssens, G., Lewin, P. A., Prieels, D., … Avery, S. (2016, 2018/12/03). Experimental observation of acoustic emissions generated by a pulsed proton beam from a hospital-based clinical cyclotron. *Medical Physics*, *42*(12), 7090-7097. https://doi.org/10.1118/1.4935865
(pp. 9, 21).

Knopf, A.-C., & Lomax, A. (2013). In vivo proton range verification: a review. *Physics in Medicine and Biology*, *58*(15), R131. Retrieved from http://stacks.iop.org/0031-9155/58/i=15/a=R131
(p. 9).

Kozlovsky, B., Murphy, R. J., & Ramaty, R. (2002). Nuclear deexcitation gamma-ray lines from accelerated particle interactions. *The Astrophysical Journal Supplement Series*, *141*(2), 523. Retrieved from http://stacks.iop.org/0067-0049/141/i=2/a=523
(pp. 17, 71).

Kraan, A. C. (2015). Range verification methods in particle therapy: Underlying physics and Monte Carlo modeling. *Frontiers in Oncology*, *5*, 150. https://doi.org/10.3389/fonc.2015.00150
(p. 9).

Krane, K. S. (1988). *Introductory nuclear physics*. Wiley.
(p. 37).

Krimmer, J., Dauvergne, D., Létang, J., & Testa, É. (2018). Prompt-gamma monitoring in hadrontherapy: A review. *Nuclear Instruments and Methods in Physics Research Section A: Accelerators, Spectrometers, Detectors and Associated Equipment*, *878*, 58-73. (Radiation Imaging Techniques and Applications) https://doi.org/https://doi.org/10.1016/j.nima.2017.07.063
(pp. 9, 16).

Kurz, C., Bauer, J., Conti, M., Guérin, L., Eriksson, L., & Parodi, K. (2015). Investigating the limits of PET/CT imaging at very low true count rates and high random fractions in ion-beam therapy monitoring. *Medical Physics*, *42*(7), 3979-3991. https://doi.org/10.1118/1.4921995
(p. 14).

Lagendijk, J. J. W., Raaymakers, B. W., Raaijmakers, A. J. E., Overweg, J., Brown, K. J., Kerkhof, E. M., … van der Heide, U. A. (2008, 2019/05/26). MRI/linac integration. *Radiotherapy and Oncology*, *86*(1), 25-29. https://doi.org/10.1016/j.radonc.2007.10.034
(p. 118).

Lee, E., Werner, M. E., Karp, J. S., & Surti, S. (2013). Design optimization of a Time-Of-Flight, breast PET scanner. *IEEE Transactions on Nuclear Science*, *60*(3), 1645-1652.
(p. 15).

Lehrack, S., Assmann, W., Bertrand, D., Henrotin, S., Herault, J., Heymans, V., … Parodi, K. (2017). Submillimeter ionoacoustic range determination for protons in water at a clinical synchrocyclotron. *Physics in Medicine and Biology*, *62*(17), L20. Retrieved from http://stacks.iop.org/0031-9155/62/i=17/a=L20
(pp. 9, 22).

Lestand, L., Montarou, G., Force, P., Joly, B., Lambert, D., Magne, M., … Chadelas, R. (2017). In beam pet acquisition on 75 mev. u^{-1} carbon beam using sampling-based read-out electronics. In *IEEE transactions on radiation and plasma medical sciences* (Vol. 1, p. 87-95).
(p. 115).

Levin, W. P., Kooy, H., Loeffler, J. S., & DeLaney, T. F. (2005, 09 27). Proton beam therapy. *British Journal Of Cancer*, *93*, 849 EP -. Retrieved from https://doi.org/10.1038/sj.bjc.6602754
(p. 6).

Lopes, P. C., Crespo, P., Simões, H., Marques, R. F., Parodi, K., & Schaart, D. R. (2018). Simulation of proton range monitoring in an anthropomorphic phantom using multi-slat collimators and time-of-flight detection of prompt-gamma quanta. *Physica Medica*, *54*, 1-14. https://doi.org/https://doi.org/10.1016/j.ejmp.2018.09.001
(p. 17).

Low, D. A., Harms, W. B., Mutic, S., & Purdy, J. A. (1998). A technique for the quantitative evaluation of dose distributions. *Medical Physics*, *25*(5), 656-661.
(p. 103).

Min, C.-H., Kim, C. H., Youn, M.-Y., & Kim, J.-W. (2006). Prompt gamma measurements for locating the dose falloff region in the proton therapy. *Applied Physics Letters*, *89*(18), 183517. https://doi.org/10.1063/1.2378561
(p. 17).

Min, C. H., Zhu, X., Winey, B. A., Grogg, K., Testa, M., El Fakhri, G., … Shih, H. A. (2013, 2018/12/03). Clinical application of in-room positron emission tomography for in vivo treatment monitoring in proton radiation therapy. *International Journal of Radiation Oncology, Biology, Physics*, *86*(1), 183-189. https://doi.org/10.1016/j.ijrobp.2012.12.010
(p. 13).

Mizuno, H., Tomitani, T., Kanazawa, M., Kitagawa, A., Pawelke, J., Iseki, Y., … Ishii, K. (2003). Washout measurement of radioisotope implanted by radioactive beams in the rabbit. *Physics in Medicine and Biol-*

ogy, *48*(15), 2269. Retrieved from http://stacks.iop.org/0031-9155/48/i=15/a=302
(pp. 74, 75, 75, 75).

Möhler, C., Russ, T., Wohlfahrt, P., Elter, A., Runz, A., Richter, C., & Greilich, S. (2018). Experimental verification of stopping-power prediction from single- and dual-energy computed tomography in biological tissues. *Physics in Medicine and Biology*, *63*(2), 025001. Retrieved from http://stacks.iop.org/0031-9155/63/i=2/a=025001
(p. 8).

Moteabbed, M., España, S., & Paganetti, H. (2011). Monte Carlo patient study on the comparison of prompt gamma and PET imaging for range verification in proton therapy. *Physics in Medicine and Biology*, *56*(4), 1063. Retrieved from http://stacks.iop.org/0031-9155/56/i=4/a=012
(pp. 80, 80, 90).

Moteabbed, M., Schuemann, J., & Paganetti, H. (2014, 2019/05/30). Dosimetric feasibility of real-time MRI-guided proton therapy. *Medical Physics*, *41*(11), 111713. https://doi.org/10.1118/1.4897570
(p. 118).

Nenoff, L., Priegnitz, M., Janssens, G., Petzoldt, J., Wohlfahrt, P., Trezza, A., … Richter, C. (2017). Sensitivity of a prompt-gamma slit-camera to detect range shifts for proton treatment verification. *Radiotherapy and Oncology*, *125*(3), 534-540. https://doi.org/https://doi.org/10.1016/j.radonc.2017.10.013
(p. 117, 117).

Nie, W., Jones, K. C., Petro, S., Kassaee, A., Sehgal, C. M., & Avery, S. (2018). Proton range verification in homogeneous materials through acoustic measurements. *Physics in Medicine and Biology*, *63*(2), 025036. Retrieved from http://stacks.iop.org/0031-9155/63/i=2/a=025036
(p. 9).

Nishio, T., Miyatake, A., Ogino, T., Nakagawa, K., Saijo, N., & Esumi, H. (2010, 2017/10/12). The development and clinical use of a beam online PET system mounted on a rotating gantry port in proton therapy. *International Journal of Radiation Oncology, Biology, Physics*, *76*(1), 277-286. https://doi.org/10.1016/j.ijrobp.2009.05.065
(p. 14).

NNDC. (2015). *National nuclear data center.*
(p. 57).

Otuka, N., Dupont, E., Semkova, V., Pritychenko, B., Blokhin, A., Aikawa, M., … Zhuang, Y. (2014). Towards a more complete and accurate experimental nuclear reaction data library (EXFOR): International collaboration between nuclear reaction data centres (NRDC). *Nuclear Data Sheets*, *120*(Supplement C), 272-276.

https://doi.org/10.1016/j.nds.2014.07.065
(pp. 11, 71).

Paganetti, H. (2012). Range uncertainties in proton therapy and the role of Monte Carlo simulations. *Physics in Medicine and Biology*, *57*(11), R99-R117. https://doi.org/10.1088/0031-9155/57/11/R99
(pp. 8, 8, 66).

Parodi, K. (2011). Proton therapy physics. In H. Paganetti (Ed.), (Vol. 20115763, pp. 489–524). Boca Raton: CRC Press.
(p. 9).

Parodi, K. (2015). Vision 20/20: Positron emission tomography in radiation therapy planning, delivery, and monitoring. *Medical Physics*, *42*(12), 7153-7168. https://doi.org/10.1118/1.4935869
(p. 9).

Parodi, K., Ferrari, A., Sommerer, F., & Paganetti, H. (2007). Clinical CT-based calculations of dose and positron emitter distributions in proton therapy using the FLUKA Monte Carlo code. *Physics in Medicine and Biology*, *52*(12), 3369. Retrieved from http://stacks.iop.org/0031-9155/52/i=12/a=004
(p. 70).

Parodi, K., Paganetti, H., Shih, H. A., Michaud, S., Loeffler, J. S., Delaney, T. F., … Bortfeld, T. (2007, 07). Patient study of in vivo verification of beam delivery and range, using positron emission tomography and computed tomography imaging after proton therapy. *International journal of radiation oncology, biology, physics*, *68*(3), 920-934. https://doi.org/10.1016/j.ijrobp.2007.01.063
(p. 66).

Parodi, K., & Polf, J. C. (2018, 11). In vivo range verification in particle therapy. *Medical Physics*, *45*(11), e1036-e1050. https://doi.org/10.1002/mp.12960
(p. 9).

Parra, L., & Barrett, H. H. (1998, April). List-mode likelihood: EM algorithm and image quality estimation demonstrated on 2-D PET. *IEEE Transactions on Medical Imaging*, *17*(2), 228-235.
(p. 11).

Patch, S. K., Covo, M. K., Jackson, A., Qadadha, Y. M., Campbell, K. S., Albright, R. A., … Phair, L. (2016). Thermoacoustic range verification using a clinical ultrasound array provides perfectly co-registered overlay of the bragg peak onto an ultrasound image. *Physics in Medicine and Biology*, *61*(15), 5621. Retrieved from http://stacks.iop.org/0031-9155/61/i=15/a=5621
(pp. 9, 21).

Peng, B. H., & Levin, C. S. (2010, 09). Recent development in PET instrumentation. *Current pharmaceutical biotechnology*, *11*(6), 555-571. Re-

trieved from https://www.ncbi.nlm.nih.gov/pubmed/20497121
(p. 14).

Pennazio, F., Battistoni, G., Bisogni, M. G., Camarlinghi, N., Ferrari, A., Ferrero, V., … Cerello, P. (2018). Carbon ions beam therapy monitoring with the INSIDE in-beam PET. *Physics in Medicine and Biology*, *63*(14), 145018. Retrieved from http://stacks.iop.org/0031-9155/63/i=14/a=145018
(p. 118).

Perali, I., Celani, A., Bombelli, L., Fiorini, C., Camera, F., Clementel, E., … Stappen, F. V. (2014). Prompt gamma imaging of proton pencil beams at clinical dose rate. *Physics in Medicine and Biology*, *59*(19), 5849. Retrieved from http://stacks.iop.org/0031-9155/59/i=19/a=5849
(pp. 17, 47, 48).

Perl, J., Shin, J., Schümann, J., Faddegon, B., & Paganetti, H. (2012, 2018/11/30). TOPAS: An innovative proton Monte Carlo platform for research and clinical applications. *Medical Physics*, *39*(11), 6818-6837. https://doi.org/10.1118/1.4758060
(pp. 65, 74).

Petzoldt, J., Roemer, K. E., Enghardt, W., Fiedler, F., Golnik, C., Hueso-González, F., … Pausch, G. (2016). Characterization of the microbunch time structure of proton pencil beams at a clinical treatment facility. *Physics in Medicine and Biology*, *61*(6), 2432. Retrieved from http://stacks.iop.org/0031-9155/61/i=6/a=2432
(pp. 20, 46).

Pinto, M., Dauvergne, D., Freud, N., Krimmer, J., Letang, J. M., Ray, C., … Testa, E. (2014). Design optimisation of a TOF-based collimated camera prototype for online hadrontherapy monitoring. *Physics in Medicine and Biology*, *59*(24), 7653. Retrieved from http://stacks.iop.org/0031-9155/59/i=24/a=7653
(p. 17).

Priegnitz, M., Barczyk, S., Nenoff, L., Golnik, C., Keitz, I., Werner, T., … Richter, C. (2016). Towards clinical application: prompt gamma imaging of passively scattered proton fields with a knife-edge slit camera. *Physics in Medicine and Biology*, *61*(22), 7881. Retrieved from http://stacks.iop.org/0031-9155/61/i=22/a=7881
(pp. 17, 117).

PTCOG. (2019). Retrieved from https://www.ptcog.ch
(pp. 2, 2, 124, 124).

Raaymakers, B. W., Jürgenliemk-Schulz, I. M., Bol, G. H., Glitzner, M., Kotte, A. N. T. J., van Asselen, B., … Lagendijk, J. J. W. (2017). First patients treated with a 1.5 T MRI-linac: clinical proof of concept of a high-precision, high-field MRI guided radiotherapy treatment. , *62*(23), L41-L50. https://doi.org/10.1088/1361-6560/aa9517

(p. 118).

Raaymakers, B. W., Raaijmakers, A. J. E., & Lagendijk, J. J. W. (2008). Feasibility of MRI guided proton therapy: magnetic field dose effects. , *53*(20), 5615-5622. https://doi.org/10.1088/0031-9155/53/20/003
(p. 118).

Rassouli, N., Etesami, M., Dhanantwari, A., & Rajiah, P. (2017, 10). Detector-based spectral CT with a novel dual-layer technology: principles and applications. *Insights into imaging*, *8*(6), 589-598. https://doi.org/10.1007/s13244-017-0571-4
(p. 8).

Richter, C., Pausch, G., Barczyk, S., Priegnitz, M., Keitz, I., Thiele, J., … Baumann, M. (2016). First clinical application of a prompt gamma based *in vivo* proton range verification system. *Radiotherapy and Oncology*, *118*(2), 232-237. https://doi.org/10.1016/j.radonc.2016.01.004
(pp. 17, 102, 117).

Rimmer, E., & Fisher, P. (1968). Resonances in the (p, n) reaction on ^{12}C. *Nuclear Physics A*, *108*(3), 561-566. https://doi.org/10.1016/0375-9474(68)90324-2
(p. 37).

Schellhammer, S. M., Hoffmann, A. L., Gantz, S., Smeets, J., van der Kraaij, E., Quets, S., … Pawelke, J. (2018). Integrating a low-field open mr scanner with a static proton research beam line: proof of concept. , *63*(23), 23LT01. https://doi.org/10.1088/1361-6560/aaece8
(p. 118).

Schneider, U., Besserer, J., Pemler, P., Dellert, M., Moosburger, M., Pedroni, E., & Kaser-Hotz, B. (2004, 2018/11/23). First proton radiography of an animal patient. *Medical Physics*, *31*(5), 1046-1051. https://doi.org/10.1118/1.1690713
(p. 9).

Schneider, W., Bortfeld, T., & Schlegel, W. (2000). Correlation between CT numbers and tissue parameters needed for Monte Carlo simulations of clinical dose distributions. *Physics in Medicine and Biology*, *45*(2), 459. Retrieved from http://stacks.iop.org/0031-9155/45/i=2/a=314
(pp. 66, 66, 66, 67, 68, 69, 70).

Shibuya, K., Yoshida, E., Nishikido, F., Suzuki, T., Tsuda, T., Inadama, N., … Murayama, H. (2007). Annihilation photon acollinearity in PET: volunteer and phantom FDG studies. *Physics in Medicine and Biology*, *52*(17), 5249. Retrieved from http://stacks.iop.org/0031-9155/52/i=17/a=010
(p. 14).

Smeets, J., Roellinghoff, F., Prieels, D., Stichelbaut, F., Benilov, A., Busca, P., … Dubus, A. (2012). Prompt gamma imaging with a slit camera for real-time range control in proton therapy. *Physics in Medicine and Biology*,

57(11), 3371. Retrieved from http://stacks.iop.org/0031-9155/57/i=11/a=3371
(pp. 17, 102, 102).

Somlai-Schweiger, I., Schneider, F., & Ziegler, S. (2015). Performance analysis of digital silicon photomultipliers for PET. *Journal of Instrumentation*, *10*(05), P05005. Retrieved from http://stacks.iop.org/1748-0221/10/i=05/a=P05005
(p. 31).

Sportelli, G., Belcari, N., Camarlinghi, N., Cirrone, G. A. P., Cuttone, G., Ferretti, S., … Rosso, V. (2014). First full-beam PET acquisitions in proton therapy with a modular dual-head dedicated system. *Physics in Medicine and Biology*, *59*(1), 43. Retrieved from http://stacks.iop.org/0031-9155/59/i=1/a=43
(p. 81).

Stichelbaut, & Jongen. (2003, October). *39th meeting of the Particle Therapy Co-Operative Group, San Francisco, CA.* (PTCOG 2003)
(p. 16).

Studenski, M. T., & Xiao, Y. (2010). Proton therapy dosimetry using positron emission tomography. *World J. Radiol.*, *2*, 135.
(p. 9).

Sulak, L., Armstrong, T., Baranger, H., Bregman, M., Levi, M., Mael, D., … Learned, J. (1979). Experimental studies of the acoustic signature of proton beams traversing fluid media. *Nuclear Instruments and Methods*, *161*(2), 203-217. https://doi.org/https://doi.org/10.1016/0029-554X(79)90386-0
(p. 21).

Taasti, V. T., Michalak, G. J., Hansen, D. C., Deisher, A. J., Kruse, J. J., Krauss, B., … McCollough, C. H. (2018). Validation of proton stopping power ratio estimation based on dual energy CT using fresh tissue samples. *Physics in Medicine and Biology*, *63*(1), 015012. Retrieved from http://stacks.iop.org/0031-9155/63/i=1/a=015012
(p. 8).

Tada, J., Hayakawa, Y., Hosono, K., & Inada, T. (1991). Time resolved properties of acoustic pulses generated in water and in soft tissue by pulsed proton beam irradiation—a possibility of doses distribution monitoring in proton radiation therapy. *Medical Physics*, *18*(6), 1100-1104. https://doi.org/10.1118/1.596618
(p. 21).

Ten Haken, R. K., Nussbaum, G. H., Emami, B., & Hughes, W. L. (1981). Photon activation—^{15}O decay studies of tumor blood flow. *Medical Physics*, *8*(3), 324-336. https://doi.org/10.1118/1.594835
(pp. 75, 76).

Testa, E., Bajard, M., Chevallier, M., Dauvergne, D., Le Foulher, F., Freud,

N., … Testa, M. (2008). Monitoring the Bragg peak location of 73MeV/u carbon ions by means of prompt γ-ray measurements. *Applied Physics Letters*, *93*(9), 093506. https://doi.org/10.1063/1.2975841
(p. 17).

Tomitani, T., Pawelke, J., Kanazawa, M., Yoshikawa, K., Yoshida, K., Sato, M., … Takizawa, S. (2003). Washout studies of ^{11}C in rabbit thigh muscle implanted by secondary beams of HIMAC. *Physics in Medicine and Biology*, *48*(7), 875. Retrieved from http://stacks.iop.org/0031-9155/48/i=7/a=305
(p. 75).

Toramatsu, C., Yoshida, E., Wakizaka, H., Mohammadi, A., Ikoma, Y., Tashima, H., … Yamaya, T. (2018). Washout effect in rabbit brain: in-beam PET measurements using ^{10}C, ^{11}C and ^{15}O ion beams. *Biomedical Physics & Engineering Express*, *4*(3), 035001. Retrieved from http://stacks.iop.org/2057-1976/4/i=3/a=035001
(p. 75, 75).

UMCG, P. R. (2018, January). *UMCG behandelt eerste patiënten met protonentherapie.* https://www.umcg.nl/NL/UMCG/Nieuws/Persberichten/Paginas/UMCG-behandelt-eerste-patienten-met-protonentherapie.aspx.
(pp. 2, 124).

Urie, M., Goitein, M., Holley, W. R., & Chen, G. T. Y. (1986). Degradation of the Bragg peak due to inhomogeneities. *Physics in Medicine and Biology*, *31*(1), 1. Retrieved from http://stacks.iop.org/0031-9155/31/i=1/a=001
(p. 79).

Van Abbema, J. K. (2017). Accurate relative stopping power prediction from dual energy ct for proton therapy: Methodology and experimental validation. (p. 8).

Van Abbema, J. K., Van der Schaaf, A., Kristanto, W., Groen, J. M., & Greuter, M. J. W. (2012, 2018/11/23). Feasibility and accuracy of tissue characterization with dual source computed tomography. *Physica Medica: European Journal of Medical Physics*, *28*(1), 25-32. https://doi.org/10.1016/j.ejmp.2011.01.004
(p. 8).

van Abbema, J. K., van Goethem, M.-J., Greuter, M. J. W., van der Schaaf, A., Brandenburg, S., & van der Graaf, E. R. (2015, apr). Relative electron density determination using a physics based parameterization of photon interactions in medical DECT. *Physics in Medicine and Biology*, *60*(9), 3825-3846.
(p. 8).

Vandenberghe, S., Mikhaylova, E., D'Hoe, E., Mollet, P., & Karp, J. S. (2016).

Recent developments in time-of-flight PET. *EJNMMI Physics*, *3*(1), 3. https://doi.org/10.1186/s40658-016-0138-3
(p. 15).

Verburg, J. M., & Bortfeld, T. (2016). TU-FG-BRB-06: A prompt gamma-ray spectroscopy system for clinical studies of in vivo proton range verification. *Medical Physics*, *43*(6Part35), 3757-3757. https://doi.org/10.1118/1.4957546
(p. 17).

Verburg, J. M., & Seco, J. (2014). Proton range verification through prompt gamma-ray spectroscopy. *Physics in Medicine and Biology*, *59*(23), 7089-7106. Retrieved from http://dx.doi.org/10.1088/0031-9155/59/23/7089
(pp. 18, 71, 71, 91, 102).

Wang, D. (2015). *A critical appraisal of the clinical utility of proton therapy in oncology* (Vol. 8).
(p. 7).

Werner, T., Berthold, J., Hueso-González, F., Koegler, T., Petzoldt, J., Roemer, K., … Pausch, G. (2019). Processing of prompt gamma-ray timing data for proton range measurements at a clinical beam delivery. , *64*(10), 105023. https://doi.org/10.1088/1361-6560/ab176d
(p. 117).

Wilson, R. R. (1946, 2018/11/29). Radiological use of fast protons. *Radiology*, *47*(5), 487-491. https://doi.org/10.1148/47.5.487
(pp. 2, 5, 124).

Xie, Y., Yin, L., Dolney, D., Avery, S., O'Grady, F., McDonough, J., … Solberg, T. D. (2017). Prompt gamma imaging for in vivo range verification of pencil beam scanning proton therapy. , *99*(1), 210-218.
(p. 18).

Yamaya, T. (2017). OpenPET: a novel open-type PET system for 3D dose verification in particle therapy. *Journal of Physics: Conference Series*, *777*(1), 012023. Retrieved from http://stacks.iop.org/1742-6596/777/i=1/a=012023
(p. 14).

Zhong, Y., Lu, W., Chen, M., & Shao, Y. (2017). PET image based intrabeam range verification and delivery optimization for charged particle radiation therapy. *International Journal of Radiation Oncology, Biology, Physics*, *99*(2, Supplement), S92. https://doi.org/https://doi.org/10.1016/j.ijrobp.2017.06.221
(p. 114).

Zhu, X., & El Fakhri, G. (2013). Proton therapy verification with PET imaging. *Theranostics*, *3*(10), 731-40.
(pp. 9, 12, 13).

Ziegler, J. F., Ziegler, M. D., & Biersack, J. P. (2010, jun). SRIM - The

stopping and range of ions in matter (2010). *Nuclear Instruments and Methods in Physics Research B*, *268*, 1818-1823.
(p. 52).